REVEALING ION TRANSFER KINETICS AND CHARGE DYNAMICS AT OPERATING BATTERY MATERIALS THROUGH SCANNING ELECTROCHEMICAL MICROSCOPY

BY

ZACHARY TYSON GOSSAGE

DISSERTATION

Submitted in partial fulfillment of the requirements
for the degree of Doctor of Philosophy in Chemistry
in the Graduate College of the
University of Illinois at Urbana–Champaign, 2020

Urbana, Illinois

Doctoral Committee:

Associate Professor Joaquín Rodríguez-López, Chair
Professor Jeffrey S. Moore
Assistant Professor Renske M. van der Veen
Professor Paul J. A. Kenis

ABSTRACT

Interfacial charge transfer plays a critical role in battery technologies, where it governs the rate of reliable ion or electron movement to and from a battery electrode during charge/discharge. As such, issues with performance are often linked to trouble at the interface across many technologies. Developing higher-performance batteries with improved rates and cycling requires better comprehension of the electrode behavior and evolution during operation. Analytical chemistry is a pivotal field for developing the necessary tools and methods. Specifically, surface-sensitive tools that can access localized or single particle information will help breakdown complexities across the heterogeneous and particulate composition of electrodes applied in real batteries. Among emerging surface tools, scanning electrochemical microscopy (SECM) provides broad opportunity for understanding interphase formation and evolution, measuring single particles, and mapping electrode function. This work presents the development of multiple electroanalytical methods based on SECM to evaluate localized interfacial electrochemistry at various energy storage systems.

Within size-exclusion redox flow batteries (RFBs), large, dispersible redox active polymers (RAPs) and colloids (RACs) accept millions of electrons while simultaneously exchanging an equal number of ions with the electrolyte. This charge transfer process occurs at the interface of a current collector involving material adsorption and a reliance on electron transfer kinetics for efficient charge/discharge. Avoiding complications with bulk measurements, I show that single particles can be adhered to a substrate and imaged using feedback at a 300 nm SECM probe. After making contact by slowly approaching the probe, RACs were reliably cycled using cyclic voltammetry and potentiostatic charge/discharge measurements. The results were further verified using Raman spectroscopy and COMSOL modeling. This work shows the power of SECM for understanding charge transfer at an individual particle and helps coordinate back to cycling

behavior in bulk. As a perspective, I describe efforts and progress toward single RAC measurements using Raman-SECM.

Within intercalation batteries, such as Li^+, we find highly complex interphase structures at the electrode-electrolyte interface. These structures stabilize the electrodes and guide ion movement to and from the electrolyte thus playing an essential role in device performance. In spite of its significance, ion transfer at the interphase remains poorly understood with little guidance on manipulating its structure for improved performance. Building on previous work in the Rodríguez-López group with Hg probes, I developed localized, *in situ* methods for measuring ion flux at operating battery electrodes. Using a Hg disc-well (HgDW), I show the potentials at which graphite edge plane and graphene electrodes consume Li^+ to form and stabilize their SEI. Further, the probe revealed transitions between SEI formation and (de)intercalation. I modeled the HgDW response with COMSOL to extract ion intercalation kinetics at each applied potential, thus providing quantification of the localized Li^+ transfer rate. In a follow up study, I introduced a pulsed methodology to expand our technique for mapping ionic flux across a functioning electrode and coordinate the response to electron transfer at the same locations. The techniques for understanding charge transfer at Li^+ batteries were further used to solve longstanding challenges in more traditional systems, such as Pb-acid batteries. Looking toward future applications, I present efforts to develop a robust HgDW probe based on a 300 nm Pt electrode for evaluating nanoscale battery materials and discuss applications of SECM toward understanding interphase formation in cathode materials. My projects have expanded on others' efforts to push Hg probes and SECM forward as a powerful analytical platform for evaluating interface chemistry in battery systems. This work seeds opportunity for wide access to key information for improving current and next generation technologies.

ACKNOWLEDGMENTS

I thank Prof. Joaquín Rodríguez-López for pulling me into the world of electrochemistry and opening his laboratory to what became an extremely fulfilling and life-changing experience. Jokes about the cosmos aside, his lab truly called to me via an Arecibo message on his Lab webpage when I had just finished my master's degree. The message was designed by Carl Sagan and others to reach out to the *strangers* of the universe; I did not expect it to develop a more personal and terrestrial meaning. His continued support and guidance pushed me to think outside the box and work hard to improve myself. I've grown significantly as a scientist and person; and I am extremely grateful for such an opportunity.

I thank my committee members Prof. van der Veen, Prof. Moore and Prof. Kenis for their guidance and support throughout the program. I have really enjoyed receiving feedback from talented individuals of very different backgrounds. Further, I express gratitude to my professors for teaching some excellent coursework. My brain exploded with knowledge while attending the Electrochemistry and X ray courses.

I am very thankful to past and present members of Rodríguez-López lab. My training in electrochemistry started with Dr. Burton Simpson, Dr. Zachary Barton, and Dr. Mark Burgess, but all the members have had a positive impact on my life. Dr. Jingshu Hui and Dr. Kenneth Hernández-Burgos were helpful with advice and research discussions a countless number of times. I thank Kendrich Hatfield, Abhiroop Mishra, and Heriberto Flores-Zuleta for their hard work and enjoyed conducting research with them. Aside, I thank Prof. Huimin Zhao, his lab, Dr. Fang Guo, Dr. Ashok Kumar and the Construction Engineering Research Laboratory for support and their collaborative efforts. I thank the American Chemical Society, National Science Foundation, and the Electrochemical Society for financial support.

I also want to thank my first research advisor from my undergraduate studies, Prof. Andrea Porras-Alfaro. She provided opportunity, encouragement and excellent advice when I needed help the most. She pushed me to seek a lab at UIUC, and the result was far better than expected.

Lastly, I want to thank all my family and friends for the memories and experiences. Specifically, I want to thank my wife, Sayaka, whom dealt with my madness on a daily basis. I am very grateful for my mom, dad and siblings, whom provided endless encouragement and support in my pursuit of happiness. I am forever indebted and inspired by my good friends Dr. Lynnaun Johnson, James Parmer, and Weebo.

TABLE OF CONTENTS

CHAPTER 1: Accessing and Understanding Ion and Electron Transfer at Electrode Interfaces in Energy Storage 1
CHAPTER 2: Soft Surfaces for Fast Characterization and Positioning of Scanning Electrochemical Microscopy Nanoelectrode Tips 16
CHAPTER 3: Electron Transfer and Cycling at Single Redox Active Particles for Size-Exclusion Redox Flow Batteries 34
CHAPTER 4: Probing the Reversibility and Kinetics of Li^+ during SEI Formation and (De)intercalation on Edge Plane Graphite using Ion-sensitive Scanning Electrochemical Microscopy 64
CHAPTER 5: Coordinated Mapping of Li^+ Flux and Electron Transfer Reactivity during Solid-Electrolyte Interphase Formation at a Graphene Electrode 86
CHAPTER 6: Reconstruction of Lead Acid Battery Negative Electrodes affected by Hard Sulfation using Controlled Chelation Chemistry 109
CHAPTER 7: Ongoing and Future Work 132

Appendix A: COMSOL Models for Chapter 3 145
Appendix B: COMSOL Models for Chapter 4 148
Appendix C: COMSOL Models for Chapter 5 153

CHAPTER 1

Accessing and Understanding Ion and Electron Transfer at Electrode Interfaces in Energy Storage

1.1 Abstract

Batteries continue to flourish as portable energy storage devices but realizing their full potential for modern applications (*e.g.* powering the grid, electric vehicles) requires better comprehension of the electrode behavior and evolution during operation. An important challenge for determining how battery materials function and fail is accessing information at the electrochemical interfaces where comingled ionic and electronic movement is occurring. Advanced analytical approaches including *in situ*/*in operando*, combinatorial and localized measurements are starting to access this key information, though many questions remain. My thesis work has focused on understanding and treating interface issues across different battery technologies. Most of my efforts utilized the scanning electrochemical microscope (SECM) to acquire quantitative *in situ* information at the interfaces of operating battery electrodes and single particle battery materials.

1.2 Electrode-Electrolyte Interfaces in Energy Storage

1.2.1 Introduction

Interfacial charge transfer plays a key role in reliable energy storage across various technologies including redox flow batteries (RFBs),[1-3] Li+ batteries (LIBs),[4-7] super capacitors[8] and next generation devices (*e.g.* Li-air, Na^+, K^+).[9-11] To meet demands for electric vehicles and the grid, there is a need to better identify surface and bulk properties that can improve the rate

This chapter is in part adapted and reprinted from a published review article in *Analytical Chemistry** with permission from the American Chemical Society, copyright 2018.
*Hui, J.; Gossage, Z. T.; Sarbapalli, D.; Hernández-Burgos, K.; and Rodríguez-López, J. "Advanced Electrochemical Analysis for Energy Storage Interfaces." *Anal. Chem.*, **2019**, 91 (1), 60-83. DOI: 10.1021/acs.analchem.8b05115

performance and stability of these technologies.[9, 10, 12] Issues at the interface are leading causes for poor performance and failure across technologies.[9, 12-14] Within RFBs, electrons transfer occurs between current collectors and solubilized catholyte and anolyte materials; here, material adsorption to the current collector and sluggish electron transfer kinetics are common issues.[2, 3, 15-17] In intercalation type batteries, like LIBs, the interfaces contain highly complex, multiphase (or interphase) structures that guide ions into/out of the material.[9, 18] These interphase structures occur at both cathodes and anodes thereby heavily impacting battery performance.[9, 12, 19] In this introductory chapter, I will provide some background on the key roles of interfacial ion and electron transfer in energy storage, stabilization of interphase structures, and charge transfer dynamics at battery materials. Thereafter, I will discuss my methodologies using SECM and highlight key aspects for each chapter regarding my research efforts.

1.2.2 Ion transfer at Battery Electrode Surfaces

The basis for battery operation involves extensive ion flux at the electrode–electrolyte interfaces during charge/discharge.[20] LIBs rely on a “rocking-chair” mechanism, where ions migrate through the electrolyte and move into and out of the anode and cathode.[21, 22] Researchers have dedicated much effort to understanding the mechanisms for incorporating Li^+ (or other ions) with the electrode materials,[4, 23-25] but ion transfer at the electrode-electrolyte interfaces precedes this step and includes further complexities due to dynamic, multi-component and heterogeneous interphase layers.[9, 26, 27] Our knowledge of the interphase structure and improving its properties are not well understood compared to bulk properties and analysis.[9, 28] Regardless, material performance could be improved by realizing faster ion transfer rates across the entire electrode. Recent development of new *in situ* and *in operando* analytical methods are pushing to shed light on fundamental and practical aspects of the interphase structures.[9, 28]

During interphase formation, electrons at the electrode surface meet the electrolyte ions and solvent molecules to develop the interphase structure.[29, 30] Electrodes form stable SEI during

initial cycles or may even be reactive enough to start forming SEI at open circuit.[31, 32] Ions are consumed in several surface reactions including redox reactions with surface groups and the formation of surface fluorides (*e.g.* LiF) and carbonates (*e.g.* Li_2CO_3, Li_2CO_4).[9, 29, 30, 33-35] The Li^+-SEI consists of a nanoscale film with a compact inorganic inner layer, consisting mainly of LiF, Li_2O and Li_2CO_3, and a thicker organic outer layer of more carbonates, semicarbonates, and polymers.[9, 36] An effective SEI electronically passivates the electrode, minimizing further reactions with the electrolyte while still enabling ion flux from the bulk solvent to the electrode for up to thousands of cycles.[37] However, *in situ* methods have indicated heterogeneous behavior across the SEI with micro and nano-scale fluctuations during operation or at rest.[26, 27, 38] As such, localized methods that coordinate surface reactivity, or electron transfer, with ion flux could provide deeper insight into the interphase formation process and local performance during operation.[39] Analytical methods for understanding and tracking ionic flux at battery materials are becoming highly sought after and will provide guidance for designing next generation energy storage materials.[40-42]

1.2.3 Charge Transfer to Solubilized Battery Materials

Beyond the solid electrodes used in LIBs, RFBs also rely on efficient interfacial ion and electron transfer to solubilized electrode materials.[1, 2, 43] To date, the electrode materials, known as the catholyte and anolyte, are based on small molecules,[1, 44] redox active polymers (RAPs),[2, 15] and redox active colloids (RACs).[16] For the emerging size-exclusion RFB concept, large multielectron RAPs and RACs are promising candidates because of their modular synthetic routes for structure and redox functonality.[15, 16, 45, 46] In contrast to small molecules that undergo facile outer sphere electron transfer reactions at an electrode, electron transfer to large RAPs and RACs involves adsorption to form a more complex polymer/electrode interface dictated by the polymer and electrolyte environment.[2, 3]

Currently, most RAPs have been built on an insulative backbone that involves long-distance intraparticle charge transfer through hopping between adjacent redox groups across the backbone.[15, 47-49] Reliable access to a full RAP's capacity requires efficient electron mobility as well as ion and solvent transport to/from the molecules interior.[2, 16, 50] To design optimal RAPs, structure, surface charge and the impact of the electrolyte environment need to be greatly considered.[2, 3] On the other hand, RACs present the advantage of a more robust structure due to their cross-linking, though little is known on its impact for charge access and storage.[16] Understanding charge transfer, including electrons and ions, between the current collector and RAPs or RACs, and charge movement within the molecules could lead to improved material designs for pushing forward size-exclusion RFBs.

1.2.4 Interface Issues in Lead Acid Batteries

While lead-acid batteries (LABs) remain the lowest-cost and most-used secondary battery worldwide,[37, 51] they create substantial waste (2.46 million tons in 2014) due to their relatively short cycle lifetimes.[52, 53] One major cause of failure is hard sulfation where large $PbSO_4$ crystals accumulate at the electrode-electrolyte interface of the negative electrode and impede access to the battery's original capacity.[14, 37, 54] Hard sulfation occurs when LABs are operated under partial state of charge, cycled at high rates, deeply discharged, or stored in the discharged state. Lead (II) sulfate ($PbSO_4$) formation occurs on both electrodes as part of the energy storage mechanism, but hard sulfation progresses due to inefficient conversion each cycle. Researchers have tried to minimize hard sulfation through preparation of electrodes that contain additives,[55, 56] pulsing or unique charging protocols to reverse sulfate growth,[57, 58] and electrolyte additives.[59, 60] However, most of these methods apply to new or partially used batteries with limited effectiveness for extreme states of sulfation.[58] While recycling is the most common endpoint for failed LABs, few have considered *in situ* recycling routes to refurbish the electrode surfaces instead of disassembly.

1.3 Dissertation Outline

1.3.1 Research Motivation

Battery chemistry, especially at the electrode-electrolyte interface, is highly complex and system dependent.[9] Emerging techniques are revealing components and precursors involved in interphase formation processes,[9, 61, 62] interphase reactivity, and tracking of the energy storage process.[63, 64] These techniques provide powerful insight but frequently are limited in spatiotemporal resolution. Modern LIBs and technologies beyond are typically based on composite electrodes with a heterogeneous surface structure of active material and binders.[26, 65, 66] Therefore, it becomes apparent that localized methods are better suited for such analysis; specifically, scanning probe methods including AFM,[38, 67] STM,[68] SECM,[69] SICM,[70, 71] SECCM,[42, 72, 73] and Hg-based SECM,[23, 41, 74] which are surface sensitive, have high spatiotemporal resolution, and can isolate single entities.[28]

Among the various scanning probe methods, SECM is particularly suited for energy storage studies because of its wide breadth for electroanalysis.[28, 69, 75] These techniques quantify localized information about substrate heterogeneity, electron transfer kinetics, redox species generation and uptake, morphological changes, and ionic fluxes (Figure 1.2), which help us better understand surface properties and interfacial reactions of energy storage materials.[28, 75] In SECM studies, an ultramicroelectrode (UME) is positioned close to a substrate surface immersed in solution to characterize the electrochemical processes and structural differences (Figure 1.2a). The measured current at the UME usually depends on the rate of active component fluxes (electrons or ions), tip−substrate distances, and substrate reactivity. The tip can be approached to the substrate in the z-direction or scanned along x- and y-directions at constant z-location to obtain areal mapping of specific electrochemical information at the substrate surface and the topographical changes. Further, emerging single particle methods based on nanoscale SECM probes[76] are highly promising to approach composite electrodes used in real batteries.[26, 27] Aside,

localized ion measurements are greatly lacking for battery studies, though they play an essential role in energy storage.[9, 77] My graduate research focused on analysis of interfacial processes and issues across a range of energy storage systems through SECM and other electroanalytical methods.

1.3.2 SECM with nanoelectrodes

At first, I prepared and used pyrolyzed carbon nanoelectrodes with SECM. I showed that nanoelectrodes as small as 30 nm (diameter) could rapidly approach to soft surfaces including immersed Ar bubbles and polymer films of PDMS without breakage. By approaching to a PDMS layer, it is possible to make a rough, but rapid positioning of nanoelectrodes. However, feedback theory was not reliable to either soft surface. I overcame this issue by deploying half-coated PDMS substrates that could be prepared through simple spin-coating. These substrates allowed the nanoelectrodes to be quickly positioned, then slowly repositioned above a hard, conductive, or insulator surface for further characterization, as illustrated in Figure 1.1a. This initial work provided extensive time for overcoming the difficulties of handling and using nanoelectrodes for SECM. The developments are discussed in Chapter 2.[78]

1.3.3 Electroanalysis of Energy Storage at Single Redox Active Polymers

Next, I moved to a larger but more durable 300 nm SECM probe for single particle measurements. An initial study on RACs showed adsorption to the current collector and macroelectrodes used for analysis.[16] By exploring RACs as single entities,[79] we could deconvolute complications in those bulk measurements to directly measure charge transfer at the material. Initially, we encountered issues with SECM imaging due to RAC movement across the surface. To prevent their movement, I explored electrostatic interactions involving RACs containing Cl^- counterions[80] instead of their highly dispersible PF_6^- counterpart.[16] In a follow up work, I determined heating as an effective method for immobilizing dispersible RACs by

increasing their surface contact to the substrate.[81] With adhered RACs, I showed SECM was suitable for imaging and making contact for single particle measurements. These measurements can be used for determination of fundamental parameters, *e.g.* charge diffusion rates, kinetics, internal redox concentrations, and for electroanalysis of the material upon cycling. Raman spectroscopy on few RACs further verified the single RAC measurements (Figure 1.1b). The results are presented in Chapter 3.[80, 81]

1.3.4 Li^+ Flux during SEI formation and (De)Intercalation at Graphite

After these initial works on single particles, I pivoted toward promising techniques based on Hg probes for ion measurements with SECM.[40, 41, 82] I expanded the applications of the HgDW SECM probe for evaluating ionic flux measurements during SEI formation at an active graphitic anode (Fig. 1.1c). I showed that HgDW electrodes captured irreversible and reversible components of the SEI formation process. The probe clearly revealed stabilization of the SEI film and subsequent (de)intercalation process. Further, our localized measurements agreed with the bulk anode response. To interpret the intercalation data further and extract Li^+ kinetics, I developed a COMSOL model based on previous work.[82] Through the model, I found high rates for ion transfer at the graphite edge plane; the most reactive site for electron transfer and ion intercalation.[83-85] The results are presented in Chapter 4.[86]

1.3.5 Li^+ Flux Mapping Across an MLG Electrode

Next, I expanded the application of HgDWs for acquiring both redox and ionic information at an evolving MLG interface. I focused on developing a mapping methodology that tracks ionic flux across the surface. By implementing a pulsing sequence at the substrate, I showed ion-sensitive SECM could detect Li^+ fluxes during either SEI formation or intercalation processes with temporal and spatial resolution comparable to the HgDW size (Figure 1.1d). During SEI formation, the probe revealed a broad signal for Li^+ consumption that initiated at a high positive potential on

MLG where LiF formation is known to occur.[33] Through ionic imaging, I observed location-dependent uptake of Li^+ across MLG-SiO_2 surfaces with good coordination to electron transfer passivation. Comparing our results with COMSOL modeling, I show that diffusional broadening during Li^+ flux mapping was consistent with traditional SECM feedback measurements. By coordinating potential pulse methods at the substrate with displacements of the SECM probes we gained swift access to identification of locations where high ionic flux was happening during reversible and irreversible reactions. The results are presented in Chapter 5.[87]

1.3.6 Refurbishing LAB Negative Electrodes after Hard Sulfation

In a side project, I focused on developing a remediation procedure to treat LABs after failure and extreme states of sulfation (Figure 1.1e). I started the project by looking at small chelator molecules, e.g. EDTA, NTA, IDA, and their ability to dissolve and remove $PbSO_4$ crystals from the damaged electrode surfaces. Systematically, I showed that soaking in EDTA at high pH was the most facile route due to its high stability constant for forming complexes with Pb^{2+}.[88] To reengineer the Pb^{2+} removed from the surface for further cycling, I explored electrodeposition procedures from the Pb-EDTA complexes. Again, Hg microelectrodes were effective tools to determine the impact of chelator binding and pH on Pb electrodeposition. Next, I deposited micron-thick films from Pb-EDTA onto gold substrates to look at the film morphology and test their electrochemistry as a negative electrode material. The films were able to rapidly cycle between Pb and $PbSO_4$ in 4.2 M H_2SO_4 for over 50 cycles. Further, I showed Pb-EDTA could be reduced at an actual LAB negative electrode. The results are presented in Chapter 6.

1.3.7 Further Applications and Future Work

Finally, I discuss a couple future applications and the progress made to date. On one front, I suggest the miniaturization of Hg probes to nanoscale dimensions for application to ion-sensitive SECM at single nanoparticles.[89, 90] Though nanoscale Hg probes have been rarely

demonstrated,[40] many challenges remain in their application to SECM studies. I discuss my progress developing a 300 nm HgDW (Figure 1.1f, left) and provide alternative avenues for achieving smaller ion-sensitive probes. Next, I present preliminary measurements using SECM to understand cathode interphase formation and degradation (Figure 1.1f, middle). Then, I provide results and discussion on single particle Raman-SECM measurements (Figure 1.1f, right). I discuss limitations in the current instrumentation and suggest that improving signal-to-noise in the Raman measurement could provide unprecedented spectroelectrochemical studies on battery materials. The results and discussion are presented in Chapter 7.

1.4 Figures

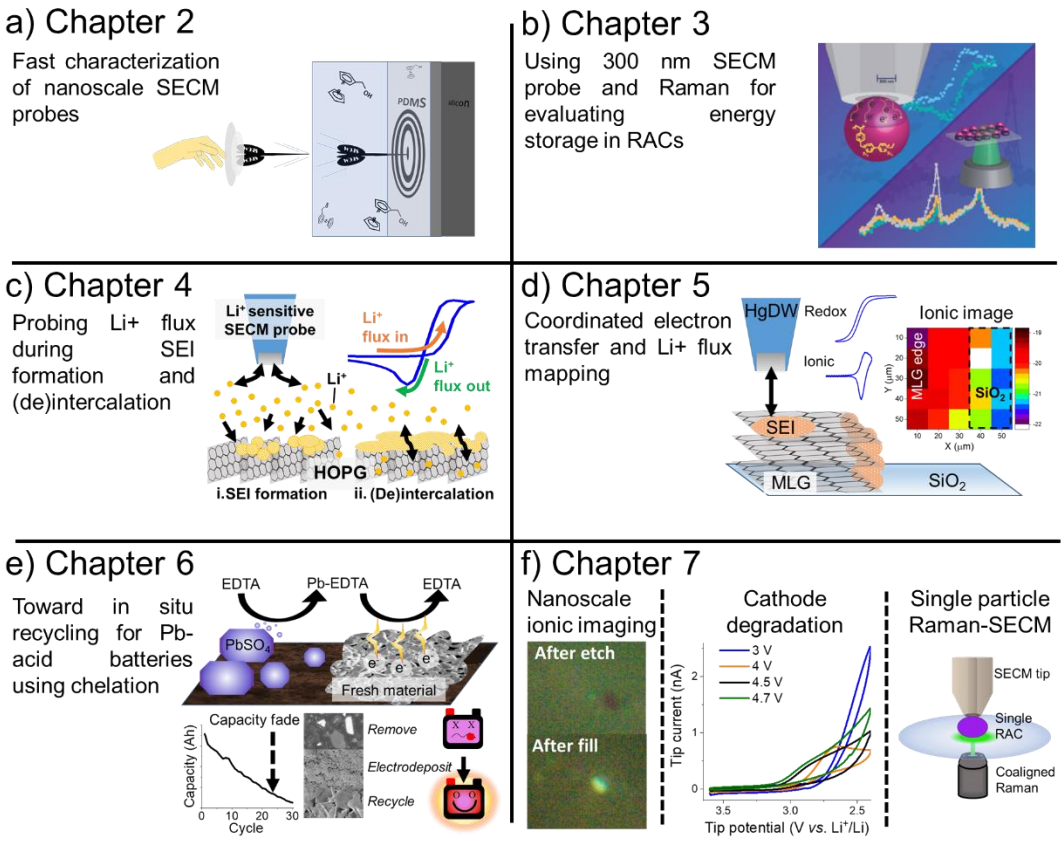

Figure 1.1. a) Chapter 2 presents improved characterization and application of nanoscale probes for SECM studies. Reproduced with permission from Gossage, *et al*.[78] b) Chapter 3 demonstrates use of a 300 nm SECM probe to make contact to single redox active particles for evaluating charge transfer and storage. Reproduced with permission from Gossage, *et al*.[81] c) Chapter 4 shows the use of Hg-based SECM probes for ion flux measurements at the surface of an operating graphite electrode. Reproduced with permission from Gossage, *et al*.[86] d) Chapter 5 shows that Hg-based SECM probes can map ionic flux at extended battery electrodes by using a pulsing protocol. Reproduced with permission from Gossage, *et al*.[87] e) Chapter 6 shows a two-step, *in situ* procedure for treating LAB failure through sulfate removal then Pb electrodeposition. f) Chapter 7 shows ongoing and future work using SECM and Hg probes to evaluate interphase processes at functioning battery electrodes.

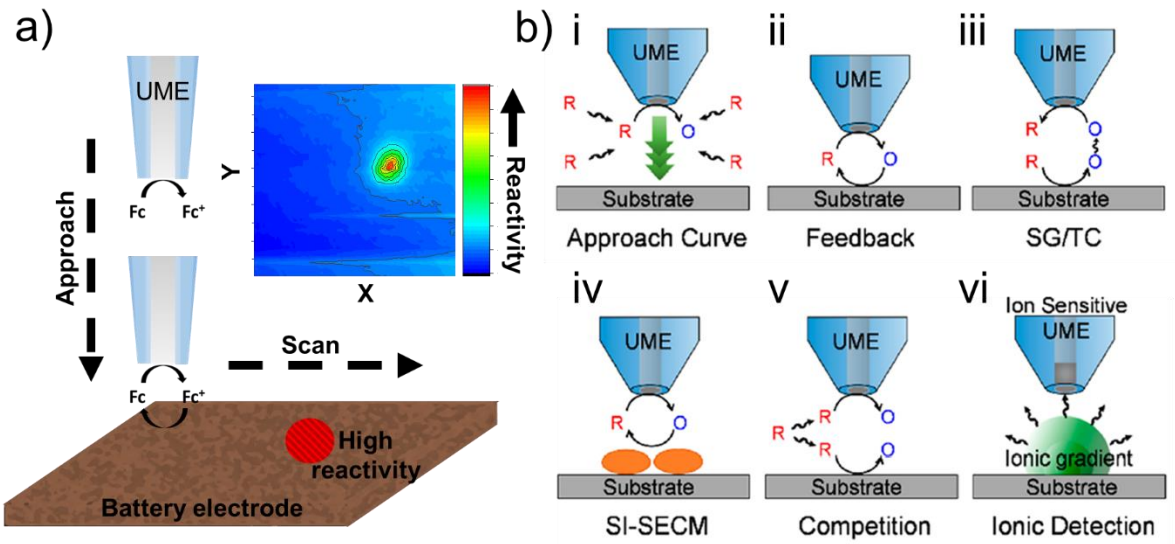

Figure 1.2. Schematics of SECM setup and its different operation modes. a) Illustration of approaching and SECM imaging at a battery electrode surface using a redox mediator couple, ferrocene/ferrocenium (Fc/Fc^+), and feedback mode. b) Modes of SECM: i) approach to an electrode surface and ii) constant-height imaging using feedback, iii) collection of soluble reaction products, iv) titrating surface species using a redox mediator, and competition between the substrate and SECM probe for v) redox mediators or vi) ions. Graphics in (b) are reproduced with permission from the American Chemical Society.[28]

1.5 References

(1) W. Li, J. Liu and C. Yan, *Electrochim. Acta*, **2012**, 79, 102-108.

(2) M. Burgess, J. S. Moore and J. Rodríguez-López, *Acc. Chem. Res.*, **2016**, 49, 2649-2657.

(3) M. Burgess, K. Hernández-Burgos, J. K. Schuh, J. Davila, E. C. Montoto, R. H. Ewoldt and J. Rodríguez-López, *J. Am. Chem. Soc.*, **2018**, 140, 2093-2104.

(4) M. D. Levi and D. Aurbach, *J. Electroanal. Chem*., **1997**, 421, 79-88.

(5) S. S. Zhang, *J. Power Sources*, **2006**, 162, 1379-1394.

(6) O. C. Harris and M. H. Tang, *J. Phys. Chem. C*, **2018**, 122, 20632-20641.

(7) H. Yildirim, A. Kinaci, M. K. Y. Chan and J. P. Greeley, *ACS Appl. Mater. Interfaces*, **2015**, 7, 18985-18996.

(8) A. Sumboja, U. M. Tefashe, G. Wittstock and P. S. Lee, *Adv. Mater. Interfaces*, **2015**, 2, 1400154.

(9) A. M. Tripathi, W.-N. Su and B. J. Hwang, *Chem. Soc. Rev*., **2018**, 47, 736-851.

(10) G. Crabtree, G. Rubloff and E. Takeuchi, Basic research needs for next generation electrical energy storage, *Report of the Office of Basic Energy Sciences Workshop on Energy Storage*, U.S. Department of Energy Office of Science, Washington, D.C., **2017**.

(11) A. Nijamudheen, D. Sarbapalli, J. Hui, J. Rodríguez-López and J. L. Mendoza-Cortes, *ACS Appl. Mater. Interfaces*, **2020**.

(12) M. R. Palacín, *Chem. Soc. Rev*., **2018**, 47, 4924-4933.

(13) J. Hui, N. B. Schorr, S. Pakhira, Z. Qu, J. L. Mendoza-Cortes and J. Rodríguez-López, *J. Am. Chem. Soc*., **2018**, 140, 13599-13603.

(14) H. A. Catherino, F. F. Feres and F. Trinidad, *J. Power Sources*, **2004**, 129, 113-120.

(15) G. Nagarjuna, J. Hui, K. J. Cheng, T. Lichtenstein, M. Shen, J. S. Moore and J. Rodríguez-López, *J. Am. Chem. Soc.*, **2014**, 136, 16309-16316.

(16) E. C. Montoto, *et al*., *J. Am. Chem. Soc.*, **2016**, 138, 13230-13237.

(17) T. S. Watkins, D. Sarbapalli, M. J. Counihan, A. S. Danis, J. Zhang, L. Zhang, K. R. Zavadil and J. Rodríguez-López, *J. Mater. Chem. A*, **2020** – Advance Article. DOI: 10.1039/D0TA00836B

(18) V. A. Agubra and J. W. Fergus, *J. Power Sources*, **2014**, 268, 153-162.

(19) W. Li, A. Dolocan, P. Oh, H. Celio, S. Park, J. Cho and A. Manthiram, *Nat. Commun*., **2017**, 8, 14589.

(20) K. W. Beard, *Linden's Handbook of Batteries*, Fifth Edition, McGraw-Hill Education, New York, N.Y., **2019**.

(21) D. Guyomard and J.-M. Tarascon, *Adv. Mater*., **1994**, 6, 408-412.

(22) J. M. Tarascon and M. Armand, in *Materials for Sustainable Energy*, Co-Published with Macmillan Publishers Ltd, UK, **2010**, pp. 171-179.

(23) J. Hui, M. Burgess, J. Zhang and J. Rodríguez-López, *ACS Nano*, **2016**, 10, 4248-4257.

(24) M. D. Levi, E. A. Levi and D. Aurbach, *J. Electroanal. Chem*., **1997**, 421, 89-97.

(25) R. B. Smith, E. Khoo and M. Z. Bazant, *J. Phys. Chem. C*, **2017**, 121, 12505-12523.

(26) H. Bülter, F. Peters, J. Schwenzel and G. Wittstock, *Angew. Chem. Int. Ed*., **2014**, 53, 10531-10535.

(27) H. Bülter, P. Schwager, D. Fenske and G. Wittstock, *Electrochim. Acta*, **2016**, 199, 366-379.

(28) J. Hui, Z. T. Gossage, D. Sarbapalli, K. Hernández-Burgos and J. Rodríguez-López, *Anal. Chem*., **2019**, 91, 60-83.

(29) K. Xu, *J. Electrochem. Soc*, **2009**, 156, A751.

(30) D. Aurbach, B. Markovsky, I. Weissman, E. Levi and Y. Ein-Eli, *Electrochim. Acta*, **1999**, 45, 67-86.

(31) V. A. Oltean, B. Philippe, S. Renault, R. Félix Duarte, H. Rensmo and D. Brandell, *Chem. Mater*., **2016**, 28, 8742-8751.

(32) D. Takamatsu, Y. Koyama, Y. Orikasa, S. Mori, T. Nakatsutsumi, T. Hirano, H. Tanida, H. Arai, Y. Uchimoto and Z. Ogumi, *Angew. Chem. Int. Ed*., **2012**, 51, 11597-11601.

(33) T. Kawaguchi, K. Shimada, T. Ichitsubo, S. Yagi and E. Matsubara, *J. Power Sources*, **2014**, 271, 431-436.

(34) N. Ogihara, Y. Igarashi, A. Kamakura, K. Naoi, Y. Kusachi and K. Utsugi, *Electrochim. Acta*, **2006**, 52, 1713-1720.

(35) M. Dollé, S. Grugeon, B. Beaudoin, L. Dupont and J. M. Tarascon, *J. Power Sources*, **2001**, 97-98, 104-106.

(36) E. Peled and S. Menkin, *J. Electrochem. Soc.*, **2017**, 164, A1703-A1719.

(37) Z. P. Cano, D. Banham, S. Ye, A. Hintennach, J. Lu, M. Fowler and Z. Chen, *Nat. Energy*, **2018**, 3, 279-289.

(38) A. v. Cresce, S. M. Russell, D. R. Baker, K. J. Gaskell and K. Xu, *Nano Lett*., **2014**, 14, 1405-1412.

(39) K. Hernández-Burgos, Z. J. Barton and J. Rodríguez-López, *Chem. Mater*., **2017**, 29, 8918-8931.

(40) Z. J. Barton and J. Rodríguez-López, *Anal. Chem*., **2014**, 86, 10660-10667.

(41) Z. J. Barton, J. Hui, N. B. Schorr and J. Rodríguez-López, *Electrochim. Acta*, **2017**, 241, 98-105.

(42) Y. Takahashi, A. Kumatani, H. Munakata, H. Inomata, K. Ito, K. Ino, H. Shiku, P. R. Unwin, Y. E. Korchev and K. Kanamura, *Nat. Commun*., **2014**, 5, 1-7.

(43) M. J. Baran, M. N. Braten, E. C. Montoto, Z. T. Gossage, L. Ma, E. Chénard, J. S. Moore, J. Rodríguez-López and B. A. Helms, *Chem. Mater*., **2018**, 30, 3861-3866.

(44) A. Parasuraman, T. M. Lim, C. Menictas and M. Skyllas-Kazacos, *Electrochim. Acta*, **2013**, 101, 27-40.

(45) E. C. Montoto, Y. Cao, K. Hernández-Burgos, C. S. Sevov, M. N. Braten, B. A. Helms, J. S. Moore and J. Rodríguez-López, *Macromolecules*, **2018**, 51, 3539-3546.

(46) M. Burgess, E. Chénard, K. Hernández-Burgos, G. Nagarjuna, R. S. Assary, J. Hui, J. S. Moore and J. Rodríguez-López, *Chem. Mater*., **2016**, 28, 7362-7374.

(47) E. F. Dalton and R. W. Murray, *J. Phys. Chem*., **1991**., 95(16), 6383-6389.

(48) C. Amatore, Y. Bouret, E. Maisonhaute, J. I. Goldsmith and H. D. Abruña, *Chem. Eur. J*., **2001**, 7, 2206-2226.

(49) D. A. Buttry and F. C. Anson, *J. Electroanal. Chem.*, **1981**, 130, 333-338.

(50) K. W. Pollak, J. W. Leon, J. M. J. Fréchet, M. Maskus and H. D. Abruña, *Chem. Mater*., **1998**, 10, 30-38.

(51) O. Schmidt, A. Hawkes, A. Gambhir and I. Staffell, *Nat. Energy*, **2017**, 2, 17110.

(52) W. Zhang, J. Yang, X. Wu, Y. Hu, W. Yu, J. Wang, J. Dong, M. Li, S. Liang and J. Hu, *Renew. Sustain. Energy Rev*., **2016**, 61, 108-122.

(53) Z. Sun, H. Cao, X. Zhang, X. Lin, W. Zheng, G. Cao, Y. Sun and Y. Zhang, *Waste Management*, **2017**, 64, 190-201.

(54) D. Pavlov, *Lead-acid batteries: science and technology*, Elsevier, **2011**.

(55) Q. Long, G. Ma, Q. Xu, C. Ma, J. Nan, A. Li and H. Chen, *J. Power Sources*, **2017**, 343, 188-196.

(56) A. Banerjee, B. Ziv, Y. Shilina, E. Levi, S. Luski and D. Aurbach, *ACS Appl. Mater. Interfaces*, **2017**, 9, 3634-3643.

(57) B. Zhang, J. Zhong, W. Li, Z. Dai and Z. Cheng, *J. Power Sources*, **2010**, 195, 4338-4343.

(58) C. Spanos, S. A. Berlinger, A. Jayan and A. C. West, *J. Electrochem. Soc*, **2016**, 163, A1612-A1618.

(59) N. Vangapally, S. A. Gaffoor and S. K. Martha, *Electrochim. Acta*, **2017**, 258, 1493-1501.

(60) G. Petkova, P. Nikolov and D. Pavlov, *J. Power Sources*, **2006**, 158, 841-845.

(61) J. Z. Olson, P. K. Johansson, D. G. Castner and C. W. Schlenker, *Chem. Mater*., **2018**, 30, 1239-1248.

(62) F. Shi, P. N. Ross, G. A. Somorjai and K. Komvopoulos, *J. Phys. Chem. C*, **2017**, 121, 14476-14483.

(63) J. Lim, Y. Li, D. H. Alsem, H. So, S. C. Lee, P. Bai, D. A. Cogswell, X. Liu, N. Jin and Y.-s. Yu, *Science*, **2016**, 353, 566-571.

(64) J. L. L. Lopez and P. J. Grandinetti, *J. Mater. Chem. A*, **2018**, 6, 231-243.

(65) E. M. Erickson, C. Ghanty and D. Aurbach, *J. Phys. Chem*., **2014**, 5, 3313-3324.

(66) P. G. Bruce, S. A. Freunberger, L. J. Hardwick and J.-M. Tarascon, *Nat. Mater*., **2012**, 11, 19-29.

(67) S. Wang, Q. Liu, C. Zhao, F. Lv, X. Qin, H. Du, F. Kang and B. Li, *Energy Environ. Mater*., **2018**, 1, 28-40.

(68) L. Seidl, S. Martens, J. Ma, U. Stimming and O. Schneider, *Nanoscale*, **2016**, 8, 14004-14014.

(69) E. Ventosa and W. Schuhmann, *Phys. Chem. Chem. Phys*., **2015**, 17, 28441-28450.

(70) A. L. Lipson, R. S. Ginder and M. C. Hersam, *Adv. Mater*., **2011**, 23, 5613-5617.

(71) K. McKelvey, S. L. Kinnear, D. Perry, D. Momotenko and P. R. Unwin, *J. Am. Chem. Soc*., **2014**, 136, 13735-13744.

(72) B. Tao, L. C. Yule, E. Daviddi, C. L. Bentley and P. R. Unwin, *Angew. Chem*., **2019**, 131, 4654-4659.

(73) M. E. Snowden, M. Dayeh, N. A. Payne, S. Gervais, J. Mauzeroll and S. B. Schougaard, *J. Power Sources*, **2016**, 325, 682-689.

(74) M. A. Alpuche-Aviles, J. E. Baur and D. O. Wipf, *Anal. Chem*., **2008**, 80, 3612-3621.

(75) A. J. Bard and M. V. Mirkin, *Scanning electrochemical microscopy*, CRC Press, **2012**.

(76) T. Sun, Y. Yu, B. J. Zacher and M. V. Mirkin, *Angew. Chem. Int. Ed*., **2014**, 53, 14120-14123.

(77) D. X. Liu, J. Wang, K. Pan, J. Qiu, M. Canova, L. R. Cao and A. C. Co, *Angew. Chem. Int. Ed*., **2014**, 53, 9498-9502.

(78) Z. T. Gossage, B. H. Simpson, N. B. Schorr and J. Rodríguez-López, *Anal. Chem*., **2016**, 88, 9897-9901.

(79) L. A. Baker, *J. Am. Chem. Soc*., **2018**, 140, 15549-15559.

(80) Z. T. Gossage, N. B. Schorr, K. Hernández-Burgos, J. Hui, B. H. Simpson, E. C. Montoto and J. Rodríguez-López, *Langmuir*, **2017**, 33, 9455-9463.

(81) Z. T. Gossage, K. Hernández-Burgos, J. S. Moore and J. Rodríguez-López, *ChemElectroChem*, **2018**, 5, 3006-3013.

(82) Z. J. Barton and J. Rodríguez-López, *Anal. Chem*., **2017**, 89, 2716-2723.

(83) M. Winter, *J. Electrochem. Soc*., **1998**, 145, 428.

(84) R. J. Rice and R. L. McCreery, *Anal. Chem*., **1989**, 61, 1637-1641.

(85) Y. Yamada, K. Miyazaki and T. Abe, *Langmuir*, **2010**, 26, 14990-14994.

(86) Z. T. Gossage, J. Hui, Y. Zeng, H. Flores-Zuleta and J. Rodríguez-López, *Chem. Sci.*, **2019**, 10, 10749-10754.

(87) Z. T. Gossage, J. Hui, D. Sarbapalli and J. Rodríguez-López, *Analyst*, **2020**, 145, 2631-2638.

(88) R. W. Schmid and C. N. Reilley, *J. Am. Chem. Soc.*, **1956**, 78, 5513-5518.

(89) L. Hu, J. W. Freeland and J. Cabana, *ACS Appl. Energy Mater*., **2019**, 2, 2149-2160.

(90) M. Ge, J. Rong, X. Fang and C. Zhou, *Nano Lett*., **2012**, 12, 2318-2323.

CHAPTER 2

Soft Surfaces for Fast Characterization and Positioning of Scanning Electrochemical Microscopy Nanoelectrode Tips

2.1 Abstract

The testing of nanoelectrode tips for scanning electrochemical microscopy (SECM) is a slow and cumbersome task that often results in untimely electrode breakage due to crashing against a substrate. Here, we evaluated approach curves of nano- and microelectrodes to soft surfaces using SECM for a rapid and more convenient characterization and positioning protocol. Soft surfaces consisted of either a submerged argon bubble or a thin polydimethylsiloxane (PDMS) layer. While approach curves to Ar bubbles in the presence of a surfactant were promising for the characterization of microelectrode tips, their performance with nanoelectrodes was deficient. In contrast, approach curves to PDMS films allowed the rapid positioning of nanoelectrodes as small as 30 nm radius at speeds up to 5 μm/s without the risk of breakage. The nanoelectrodes were able to approach the polymer films multiple times without affecting their electrochemical performance. Furthermore, using a half-coated substrate with PDMS, nanoelectrodes could be retracted and positioned very close to the bare, hard substrate for characterization with traditional approach curves. We estimate time savings on tip characterization/positioning on the order of 10- to 100-fold. This simple procedure is easily implemented without the requirement of additional devices supplementing existing commercial SECM instruments.

This chapter is adapted and reprinted from a technical note in *Analytical Chemistry** with permission from the American Chemical Society, copyright 2016. Z.T.G. conducted the experiments, made the figures and wrote the publication. B.H.S. and N.B.S. helped with experiments and writing.

*Gossage, Z.T.; Simpson, B.H.; Schorr, N.B.; Rodríguez-López, J. "Soft Surfaces for Fast Characterization and Positioning of Scanning Electrochemical Microscopy Nanoelectrode Tips." *Anal. Chem*., **2016**, *88*, 9897-9901. DOI: 10.1021/acs.analchem.6b02213

2.2 Introduction

Scanning electrochemical microscopy (SECM) enables imaging and quantification of local electrochemical activity. SECM is used for the in situ analysis of diverse systems such as photo and electrocatalysts, surface-confined redox systems, and bioelectrochemical interfaces.[1–4] A key component for this technique is the "SECM tip," a probe electrode that can vary in size and material to fit the requirements of a particular study. Ultramicroelectrodes (UMEs) are very commonly used for SECM owing to their commercial availability and relative ease of construction. However, in order to probe smaller environments, such as single nano entities, for obtaining higher lateral resolution, increasing mass transfer, or working in highly resistive solutions, nanoelectrodes are more suitable.[5,6] Procedures such as pyrolysis and wire pulling have been very successful for preparing nanoelectrodes in a variety of sizes and geometries.[7,8] Geometry and size affect the electrochemical response of the probes, so these parameters need to be known for quantitative analysis. For this reason, it is important to characterize every probe before deploying it in SECM techniques.

When moving to nanosized SECM probes, characterization becomes quite difficult and typically involves microscopy, cyclic voltammetry (CV), and SECM approach curve analysis. Because of the diffraction limit of visible light, optical microscopy is not appropriate for this purpose. Electron microscopy is more suitable, but its use is complicated by electron beam damage to the tip, limitations in chamber height, and the need for conductive coatings to prevent overcharging of the surrounding glass. CV is useful to assess probe performance but is not enough as a stand-alone characterization technique. SECM approach curves (Figure 2.1), on the other hand, are useful to obtain the electrode's radius, a, and RG. RG is defined as the ratio of the glass radius, rg, to the electrode radius, i.e., RG = rg/a. Approach curves are obtained by plotting the normalized current i_T, as the ratio between the measured tip current, i, normalized to the current in the bulk solution, i.e., at "infinite" distance away from the electrode, i_∞.[9,10] Ultimately,

approach curve analysis prior to experimentation is the most reliable method to assess the quality of an SECM tip.

Unfortunately, approach curve analysis requires tip−substrate distances proportional to the tip radius. This means nanoscale tips need to be approached very close to the substrate prior to knowing their performance. This makes tip breakage a likely event and caution is often exercised by performing approach curves at very slow speeds, often on the order of few radii per second.[7,11] An SECM technique that could quickly and safely determine the approximate size and quality of a nanoelectrode would be very useful. Furthermore, in order for nanoelectrodes to become a routine tool, they need to have reliable, simple, and fast methods for characterization, regardless of the technology available in the laboratory. In this technical note, we evaluate the plausibility of employing soft surfaces for fast characterization and positioning of nanoelectrodes. An ideal soft surface would prevent the breakage of the SECM tip. Here, we utilized argon bubbles and soft polymer layers as substrates for characterization. We further show that following an initial approach to a soft surface, electrodes could be retracted and repositioned over hard surfaces of interest.

2.3 Materials and Methods

2.3.1 Chemicals and Materials

Hexaammineruthenium(III) chloride (ruhex) (≥99%; STREM), ferrocenemethanol (≥97%; Sigma-Aldrich), and potassium ferricyanide (≥99%; Sigma-Aldrich) were used as redox mediators for electrochemical measurements. Sodium chloride (≥99%; EMD Chem) or potassium nitrate (≥ 99%; Sigma-Aldrich) were used as electrolytes. Buffers were prepared with potassium phosphate salts (≥98; Sigma-Aldrich) or boric acid (≥99.5%; Fisher). Solutions for bubble experiments also contained sodium dodecyl sulfate (SDS) (≥99%; Fisher). Copper acetate (99.5%; Fisher) was

used in the nanoelectrode fabrication process. Polydimethylsiloxane (PDMS, Slygard 184; Dow Corning) was used for substrate fabrication.

2.3.2 Electrode Fabrication

Pt (12.5 μm radius) and carbon fiber (4 μm radius) UMEs were prepared through reported procedures using borosilicate pipettes (o.d., 1.0 mm; i.d., 0.58 mm; Sutter).[12,3] Wollaston electrodes (Goodfellow, purity 99.9%, 300 nm radius) were prepared as described elsewhere.[13] An optical microscope (Zeiss) was used to measure the UME size, geometry, and smoothness. Pyrolyzed carbon nanoelectrodes were prepared in a similar manner to previously described methods.[6,14,15] Briefly, quartz pipettes (o.d., 1.0 mm; i.d., 0.70 mm; Sutter) were pulled to various radii with a P-2000 puller and backfilled with 3 μL of copper acetate (1 mg/mL). After removing the air bubbles by tapping, the pipettes were placed under vacuum at 40 °C overnight. They were then connected via tubing to an acetylene source, and the tip was sheathed with a quartz tube connected to an Ar source. While flowing both Ar and acetylene, a propane torch was used to heat the outside of the sheathing quartz tube. Heating consisted of 60 s of heating, followed by 15 s of cooling, repeated 3 times. The acetylene pressure was 3–5 psi. Pipets were checked under an optical microscope at 1000× with transmitted light then further characterized with scanning electron microscopy (SEM, JEOL 7000F).

2.3.3 SECM Experiments

Electrochemical measurements were performed with a commercial CHI920 SECM in Millipore-purified water. We used a Teflon SECM cell with a small cylindrical opening of 4 mm diameter. A glass slide, silicon wafer, or gold-coated silicon wafer acted as a substrate connected with a Viton O-ring and Teflon base. A large Pt wire was used as the counter electrode, and Ag/AgCl reference electrodes were used in conjunction with salt bridges for all measurements. Approaches were performed with the tip biased at a potential where a steady-state current was

achieved. The data were manually fitted to an established model for flat microdisc electrodes.[10] Data were compared with optical microscope measurements, cyclic voltammetry, and approach curves to glass. For nanoelectrodes, data were also compared with SEM images.

2.3.4 Approaches to an Argon Bubble

A 2.5 mM ruhex solution was prepared in a phosphate buffer (pH = 7) with 0.25 M NaCl as supporting electrolyte and with or without ~0.15 mM sodium dodecyl sulfate. A 3 mM solution of potassium ferricyanide was prepared likewise in borate buffer. A bubble of Ar was added to fill the 4 mm opening at the bottom of the SECM cell. A disposable syringe was used to remove excess air to eliminate excessive bulging. The tip was positioned over the bubble's center and approached at various speeds.

2.3.5 Approaches to PDMS

A thin film, typically 20 μm thick, of PDMS was deposited on a portion of insulating (silicon wafer) or conductive (gold-plated silica) substrates with a spin coater (model 100; CEE). This was accomplished by placing a piece of tape tightly over half of the substrate to protect it from being coated with PDMS. The substrate was placed with the uncovered portion mostly centered on the spin coater. The settings used were 1000 rpm, 100 for ramp speed, and a total time of 180 s. These samples were cured in a vacuum oven at 60 °C overnight. The tape was removed after curing, leaving a half-coated substrate.

PDMS height was predominantly determined with an SECM and UME by probing a few points on each half through feedback approach curves to 80% or 120% i_{ss} and comparing absolute coordinates with the z-axis motor. Film heights were also determined via profilometry. Leveling of the substrate was completed with the bare half using approach curves with a Pt microelectrode or a Wollaston SECM tip. All CVs and approach curves were conducted in a phosphate-buffered ferrocenemethanol and NaCl solution.

As shown in Figure 2.2, nanoelectrodes were first positioned above the PDMS layer using stepper motors. The electrode was positioned close to the surface by eye and approached at a relatively fast speed, typically at 5 μm/s. For a nanoelectrode with a 250 nm radius, this is equivalent to 20 times its radius per second. Upon reaching the PDMS surface, we observed negative feedback and stopped the electrode automatically with a set current threshold. The nanoelectrode was then retracted 500 μm and a CV was taken to check its integrity. Then it was repositioned over the PDMS-free side. By using the previously determined height difference (Figure 2.3) and absolute z-coordinate, the electrode was then positioned within 10−20 μm from the hard surface. It should be noted that even closer positioning can be attained with care. Feedback curves were then attained by approaching the bare insulating or conductive surface at a very slow speed using the piezo-motors (5−15 nm/s). Negative feedback curves were acquired with silicon substrates. Positive feedback curves were acquired with gold substrates biased to reducing potentials for regenerating the mediator, ferrocenemethanol. Approach curves to PDMS and corresponding hard surfaces were fitted and compared with CV data.

2.4 Results

2.4.1 Liquid-Gas Interface

Figure 2.4 shows SECM approach curves to a submerged Ar bubble using UMEs. In general, when using a small amount of SDS as a surface tension stabilizer, acceptable fittings to theory were obtained with either Pt or C UMEs.[10] However, approaches to a bubble in an SDS-free solution showed an unusual approach curve similar to those acquired by Gabrielli *et al*. for various sized (0.7−4 mm dia.) air bubbles using Pt UMEs.[16] In this last study, the authors concluded that the observed discrepancies to SECM theory were due to repulsive forces between the tip's glass surface and the bubble. These forces modify the surface tension of the bubble and deform it. In our study with SDS, negative-feedback approaches with UMEs were resolved to

current levels ~40% i_{ss}, approximately equivalent to L = 0.5 in Figure 1a. As the RG of the UME increased, the obtained fittings were poorer (Figure 2.5). This correlates well with the finds of Gabrielli, where the distortion length for unmodified bubbles increased with RG.[16]

Without SDS, hydrophilic effects may trap thin layers of liquid between two objects.[17,18] AFM experiments that measured the forces on a silica microbead (7−20 μm diameter) as it approached a bubble (4 mm diameter) claimed a water film thickness up to only 150 nm.[19] We note, however, that although the presence of surfactants has been shown to modify the strength of the forces at the interface during AFM experiments, these forces were very short ranged (from a few nanometers up to 1 μm).[17,19,20] We observed distortions initiating at relatively large distances (>10 μm) that are congruent with previous SECM results.[16]

In spite of the feasibility for characterizing UMEs, an SDS modified bubble did not work well for characterizing pyrolyzed carbon nanoelectrodes. A nanoelectrode approach to a bubble typically resulted in a distorted and approximately linear decay with respect to L as presented in Figure 2.6 using an electrode with *a* = 125 nm. Some electrodes could be approached as close as 85% i_{∞} before deviating significantly from theory. The reason for this is unclear, as no correlation was established between approach success and either electrochemical performance (CV) or observed geometry (SEM). As with the UMEs, atypical approach curves might be due to repulsion and deformation. Unlike the UME, the nanoelectrode response should be closer to the short-range of the known forces mentioned above as well as the thickness of the thin residual water layer. Additionally, small tips must be closer on an absolute scale to see feedback, so the influence of repulsive forces may be too great to observe negative feedback.

2.4.2 Soft Polymer Interface

Nanoelectrodes were made to approach repeatedly and quickly, at 5 μm/s, to PDMS substrates without damaging the electrode. In this case, the substrate had half of its area coated with PDMS, while the other half consisted of a hard Si surface. The retention of the electrochemical response of such nanoelectrodes is evidenced by the similar approach curves (Figure 2.7a) and consistent steady state voltammograms (Figure 2.7b) measured before and after approach. The electrode used for Figure 2.7 had an approximate radius of 30 nm based on the CV and rough fitting of the approach curve data. While we observed small changes in the CV and approach curve after the initial approach, the steady state response remained consistent and approach curves to PDMS were fairly similar. It is possible that the initial change observed is due to small amounts of polymer adsorbed on the tip.

In direct contrast to a soft surface, approaching to a hard Si substrate at a much slower speed of 400 nm/s resulted in a crash and tip breakage, evident in the approach curve in Figure 2.7a. Thus, the soft surface enabled rapid approach speeds and tip positioning times to be dramatically decreased. Further, repositioning very close above a hard surface is uncomplicated because PDMS does not typically swell in aqueous environments meaning the height difference will remain consistent over time.[21] We estimate improvements in time efficiency of 10−100-fold with respect to more conservative strategies. A related technique that makes use of fast approaches and PDMS for preventing tip breakage has been demonstrated with scanning ion conductance microscopy, but the probes and hardware are significantly different than those used by most commercial SECM instruments.[22]

The approach data for a slightly larger nanoelectrode, characterized with this technique is presented in Figure 2.8 and fit to a 60 nm radius (Figure 2.8a). In this case, the substrate also had half of its area coated with PDMS. Direct contrast between the PDMS and hard surface approach curves indicates that PDMS was not suitable to characterize nanoelectrode tips by itself,

though the cause is not exactly clear. However, after swiftly engaging the surface on the PDMS side, repositioning and approaching the hard surface, the obtained approach curves were of high quality indicating fairly ideal behavior for a disk geometry. Furthermore, no change in electrochemical response was observed for this nanoelectrode after approaching the PDMS (Figure 2.8b,c). Half-coated conductive substrates were also applicable with this setup for characterization with positive feedback.[12]

A few groups have recently discussed approach curves to passivating layers.[23,24] Cornut et al. showed that many films responded in a very similar way to that of a strictly inert surface.[23] However, a similar, albeit small, deviation from theory when approaching PDMS with a Pt microelectrode (5 μm radius) has already been demonstrated by Wang, et al.[25] Our UME data agree well with their analysis, but when moving to SECM tips of smaller dimensions the deviation becomes more significant. To the best of our knowledge, no groups have discussed a size-dependence for approach curves to soft films.

All of our nanoelectrodes showed significant differences between the hard, inert surface and PDMS. Plausible causes are the impact of film curvature, film roughness, film porosity, or electrode geometry. We discard the impact of electrode geometry, since approaches with a 300 nm radius Wollaston electrode, which otherwise conformed to theory on a solid surface, to a flat and leveled PDMS surface showed noticeable deviation from theory. Likewise, the roughness of spin-coated PDMS films has been reported to be in the range of 1 nm, thus this should not have an effect on nanoelectrodes of the dimensions used here.[26] Perhaps mediator penetration or porosity contributes to the deviation. We explored the dependency of the approach response with other commonly used, highly charged mediators, e.g., $[Ru(NH_3)_6]^{3+/2+}$ and $[Fe(CN)_6]^{3-/4-}$, and with oxygen, in water, and no noticeable improvements to fittings were observed in spite of the varying properties of these mediators such as charge and size. Our results suggest a cutoff in fit to theory at about 250 nm for the tip radius. Although the exact reason for the lack of fitting of approach

curves performed with nanoelectrodes to PDMS remains unclear, ultimately it is simple to use the featured approach to speed up traditional characterization of nanoelectrodes on PDMS while still using established models and hard surfaces.

2.5 Conclusions

We evaluated SECM approach curves with nanoelectrodes to soft surfaces for rapid characterization and positioning. Immersed bubbles in a surfactant solution yielded a suitable interface for safely engaging the tip but failed to provide manageable approach curves for accurate positioning or characterization. On the other hand, approach curves to polymer films of PDMS revealed a more convenient method for quickly positioning nanoelectrodes close to a hard substrate. Nanoelectrodes generally need to be moved at slow speeds (e.g., 5 nm/s) to prevent breaking the electrode, thus leading to very lengthy time frames for characterization. For example, moving 100 μm at this speed would take almost 6 h. In this technical note, we showed that by approaching to a PDMS layer, it is possible to make a rough positioning of electrodes as small as 30 nm in radius by means of a convenient and time saving approach rate of 5 μm/s. This reduces that time to only 20 s. At this high speed of ~166 radii/s, feedback theory is not reliable; however, approaches were reproducible and repeatable and allowed one to swiftly engage the nanoelectrodes to a hard, conductive, or insulator surface for further characterization. The electrodes mostly retained their mechanical and electrochemical stability, in stark contrast to destructive approaches observed for hard surfaces.

Aside from its use here as a characterization tool, this work may benefit SECM work that involves species such as nanoparticles, colloids, or cells that are deposited within or adhered to soft polymer matrixes. The technical advance presented here potentially solves issues with the cumbersome characterization and implementation of nanoelectrodes on SECM measurements. It additionally offers a robust approach that is easily implemented without the requirement of additional devices supplementing existing commercial SECM instruments.

2.6 Acknowledgments

Materials characterization was carried out in part in the Frederick Seitz Materials Research Laboratory Central Research Facilities, University of Illinois.

2.7 Figures

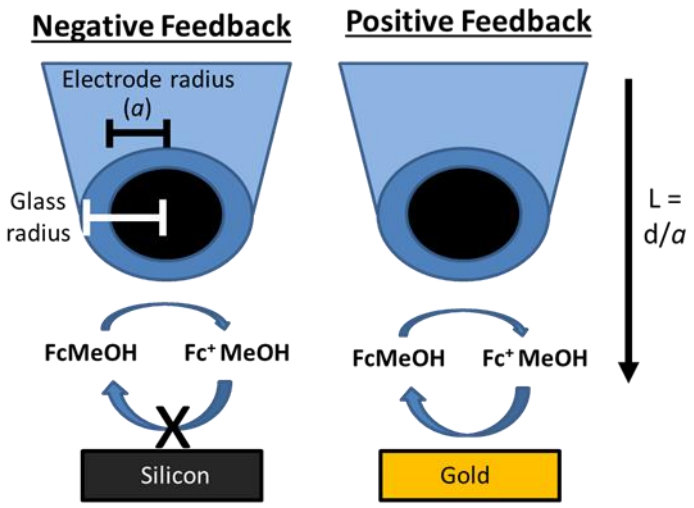

Figure 2.1. Interaction between the substrate and tip electrodes during an approach using a redox mediator (e.g. FcMeOH), leading to negative or positive feedback depending on the nature of the substrate and the distance (L) normalized to the electrode radius (*a*). Illustration of the SECM tip geometry includes the electrode radius (*a*) and insulator radius (rg) involved in the main fitting parameter (RG) that is evaluated with approach curves (RG = *rg*/*a*).

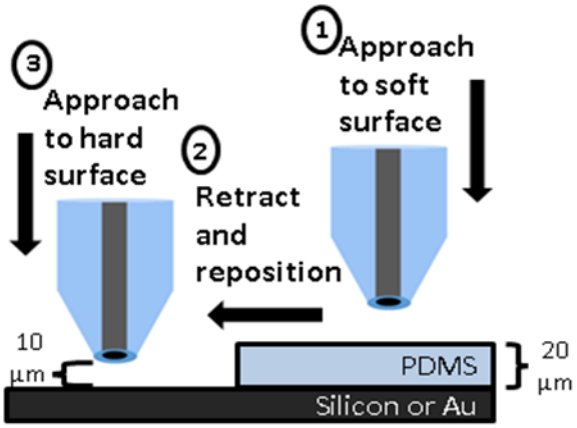

Figure 2.2. Technique and setup for using our characterization method. The PDMS film was typically between 20 and 50 µm.

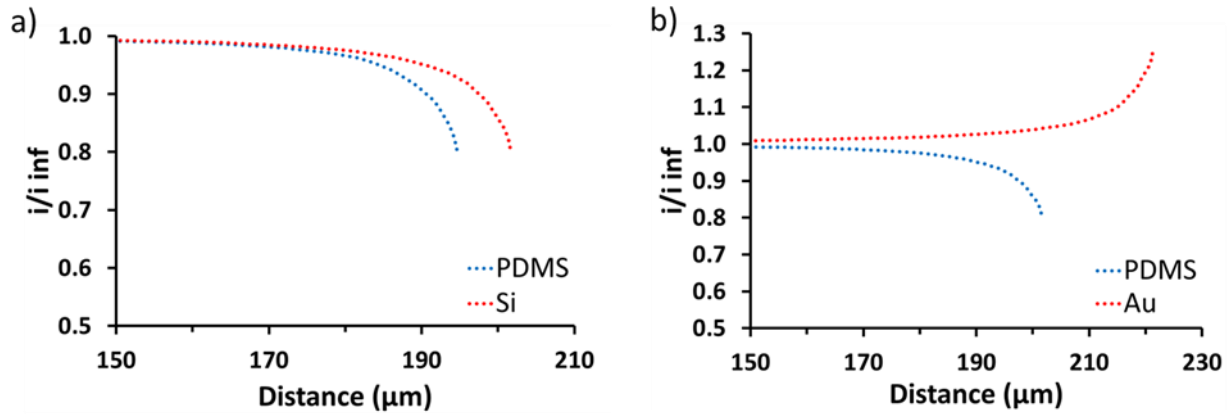

Figure 2.3. Approach curves acquired with a carbon fiber microelectrode to half PDMS-coated silicon (a) and gold (b) substrates. Feedback is attained at a shorter distance for the PDMS-coated side allowing an approximate measurement of film height. A mediator solution of 5 mM FcMeOH was used.

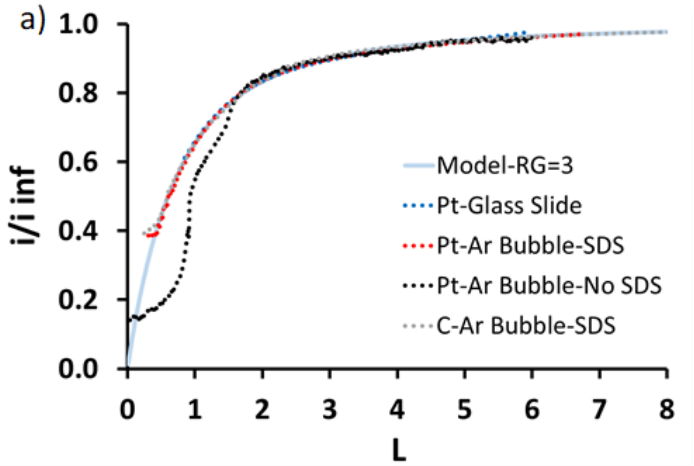

Figure 2.4. Typical negative feedback approach curves when approaching an SDS-modified Ar bubble with Pt (12.5 µm radius) and C (4 µm radius) UMEs (a) pyrolyzed C nanoelectrode (b) compared with a glass slide. An approach to an unmodified bubble is shown with a black line in (a). The inset in (b) shows a close-up SEM image of the nanoelectrode tip used for acquiring the two curves in (b). The dark region, the electrode surface, is a nice disk-shape of 250 nm diameter, surrounded by the lighter insulating glass of 330 nm diameter. For the Pt UME, the solution used was 2.5 mM ruhex, 0.25 M NaCl in a phosphate buffer (pH = 7). For the C fiber and nano electrodes, the solution contained 3 mM ferricyanide in borate buffer.

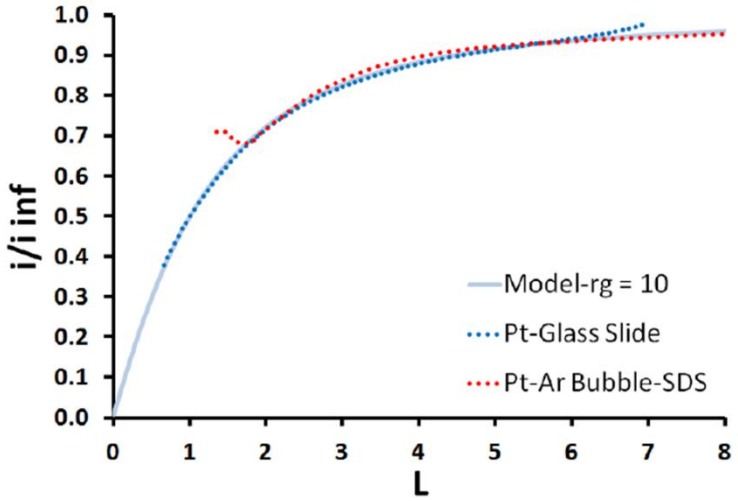

Figure 2.5. Pt microelectrode (RG = 10) approach to an Ar bubble with SDS (red) compared to an approach with the same electrode to a glass slide (blue) in a 1 mM FcMeOH solution. Solid line is the model used for fitting to an RG of 10 with a 12.5 μm radius.

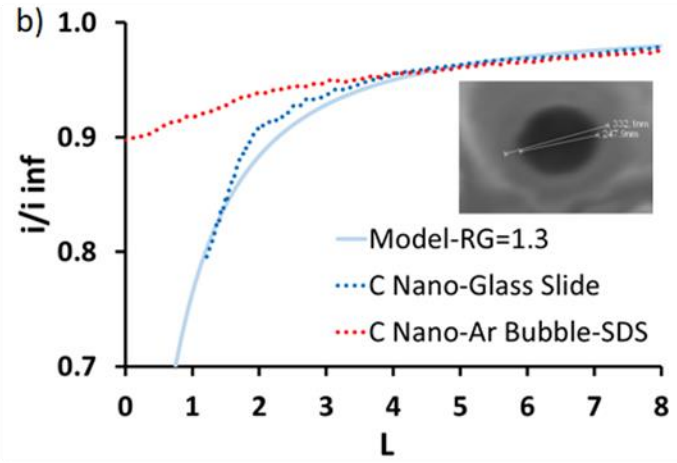

Figure 2.6. Negative feedback approach curves when approaching an SDS-modified Ar bubble with a pyrolyzed C nanoelectrode compared with a glass slide. The inset in shows a close-up SEM image of the nanoelectrode tip used for acquiring the two curves in (b). The dark region, the electrode surface, is a disk-shape of 250 nm diameter, surrounded by the lighter insulating glass of 330 nm diameter. The electrolyte contained 3 mM ferricyanide in borate buffer.

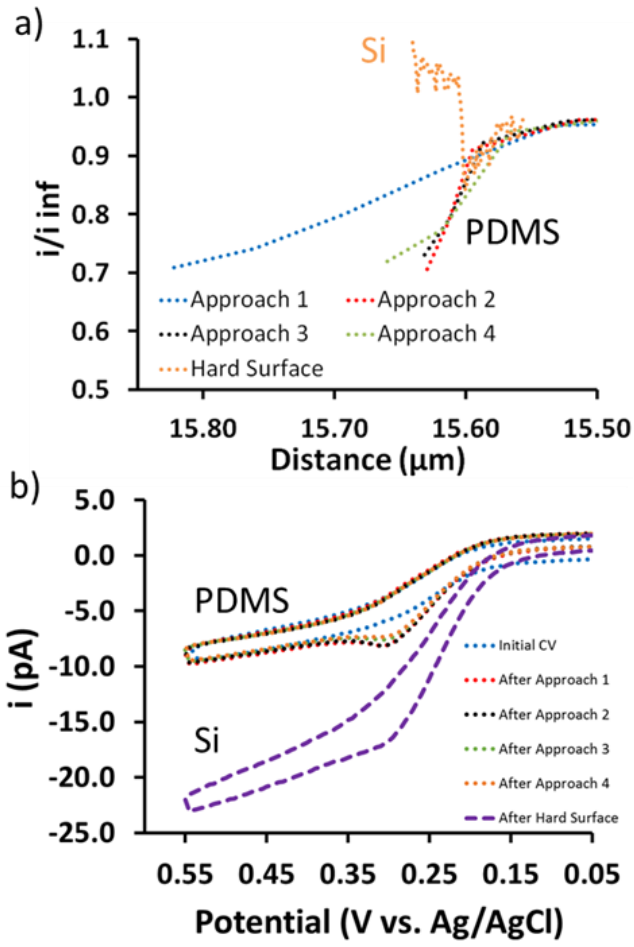

Figure 2.7. (a) Multiple approach curves with a carbon nanoelectrode (30 nm radius) at (5 µm/s) to PDMS followed by a slower approach (400 nm/s) and crash at a Si substrate. Comparison of CVs between the different approaches are overlain in part b. The mediator used was 1 mM FcMeOH.

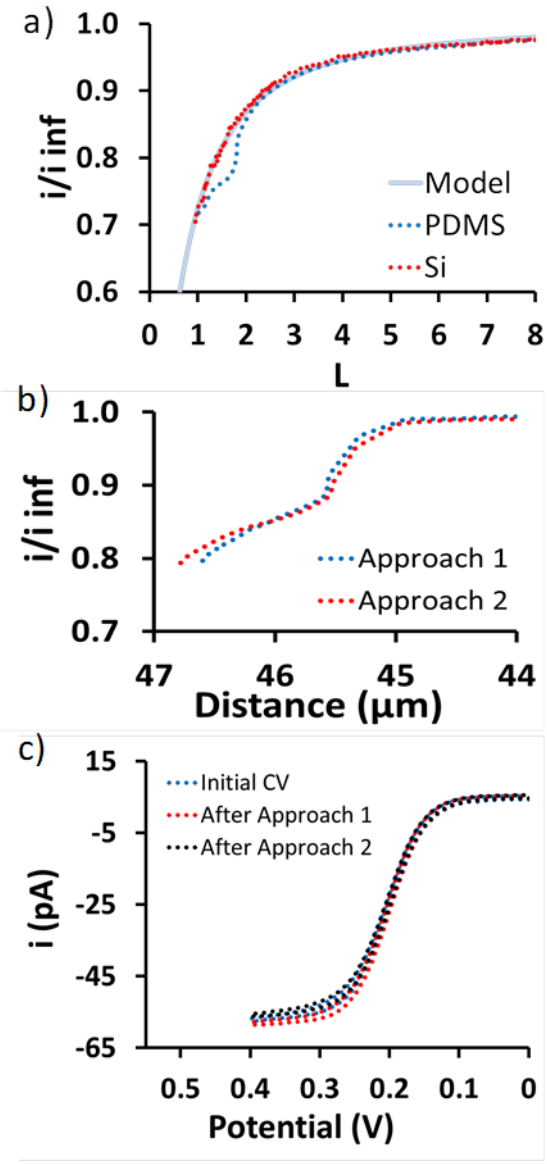

Figure 2.8. (a) Comparison between approaches to PDMS (5 µm/s) and the following approach to Si (5 nm/s). Two consecutive approaches to PDMS at the same speed are shown in part b. Intermittent CV data is overlain in part c. CV radius and approach data fitting are for a 60 nm radius; 3 mM FcMeOH was used as the redox mediator.

2.8 References

(1) Bertoncello, P. Y. *Energy Environ. Sci.* **2010**, 3, 1620.

(2) Rodríguez-López, J.; Alpuche-Avilés, M. A.; Bard, A. J. *J. Am. Chem. Soc.* **2008**, 130, 16985−16995.

(3) Bard, A. J.; Fan, F.; Pierce, D. T.; Unwin, P. R.; Wipf, D. O.; Zhou, F. *Science* **1991**, 254, 68−74.

(4) Amemiya, S.; Bard, A. J.; Fan, F.-R. F.; Mirkin, M. V.; Unwin, P. R. *Annu. Rev. Anal. Chem.* **2008**, 1, 95−131.

(5) Cox, J. T.; Zhang, B. Annu. Rev. *Anal. Chem*. **2012**, 5, 253−272.

(6) Actis, P.; Tokar, S.; Clausmeyer, J.; Babakinejad, B.; Mikhaleva, S.; Cornut, R.; Takahashi, Y.; López Córdoba, A.; Novak, P.; Shevchuck, A. I.; et al. *ACS Nano* **2014**, 8, 875−884.

(7) Shao, Y.; Mirkin, M. V.; Fish, G.; Kokotov, S.; Palanker, D.; Lewis, A. *Anal. Chem*. **1997**, 69, 1627−1634.

(8) Takahashi, Y.; Shevchuk, A. I.; Novak, P.; Babakinejad, B.; Macpherson, J.; Unwin, P. R.; Shiku, H.; Gorelik, J.; Klenerman, D.; Korchev, Y. E. *Proc. Natl. Acad. Sci.* **2012**, 109, 11540−11545.

(9) Mirkin, M. V.; Fan, F.-R. F.; Bard, A. J. *Science* **1992,** 257, 364−366.

(10) Cornut, R.; Lefrou, C. J. *Electroanal. Chem.* **2007**, 608, 59−66.

(11) Sun, P.; Zhang, Z.; Guo, J.; Shao, Y. *Anal. Chem*. **2001**, 73, 5346−5351.

(12) Kwak, J.; Bard, A. J. *Anal. Chem.* **1989**, 61, 1221−1227.

(13) Hui, J.; Burgess, M.; Zhang, J.; Rodríguez-López, J. *ACS Nano* **2016**, 10, 4248−4257.

(14) McNally, M.; Wong, D. K. *Anal. Chem*. **2001**, 73, 4793−4800.

(15) Saito, M.; Saga, A.; Matsuoka, H.; Wong, D. *Electrochem. Soc. Jpn*. **2000**, 68, 924−926.

(16) Gabrielli, C.; Huet, F.; Keddam, M.; Rousseau, P.; Vivier, V. *Electrochem. Solid-State Lett.* **2003**, 6, E23−E26.

(17) Preuss, M.; Butt, H.-J. *Langmuir* **1998**, 14, 3164−3174.

(18) Fisher, L. R.; Mitchell, E. E.; Hewitt, D.; Ralston, J.; Wolfe, J. *Colloids Surf.* **1991**, 52, 163 −174.

(19) Butt, H.-J. J. *Colloid Interface Sci*. **1994**, 166, 109−117.

(20) Ducker, W. A.; Xu, Z.; Israelachvili, J. N. *Langmuir* **1994**, 10, 3279−3289.

(21) Lee, J. N.; Park, C.; Whitesides, G. M. *Anal. Chem*. **2003**, 75, 6544−6554.

(22) Takahashi, Y.; Murakami, Y.; Nagamine, K.; Shiku, H.; Aoyagi, S.; Yasukawa, T.; Kanzaki, M.; Matsue, T. *Phys. Chem. Chem. Phys.* **2010**, 12, 10012−10017.

(23) Cornut, R.; Lefrou, C. *J. Electroanal. Chem*. **2008**, 623, 197−203.

(24) Kuss, C.; Payne, N. A.; Mauzeroll, J. *J. Electrochem. Soc*. **2016**, 163, H3066−H3071.

(25) Wang, K.; Xia, X.-H. *J. Chromatogr. A* **2006**, 1110, 222−226.

(26) Sokuler, M.; Auernhammer, G. n. K.; Roth, M.; Liu, C.; Bonacurrso, E.; Butt, H.-J. r. *Langmuir* **2010**, 26, 1544−1547.

CHAPTER 3

Electron Transfer and Cycling at Single Redox Active Particles for Size-Exclusion Redox Flow Batteries

3.1 Abstract

Redox active colloids (RACs) are dispersible, polymeric materials for size exclusion redox flow batteries that incorporate high concentrations of redox-active motifs enabling billions of electrons to be stored in each particle. In order to tap into their full potential for energy storage, it is essential to understand their internal charge mobility, capacity, and cyclability. Focusing on single particle measurements via bulk electrolysis and voltammetry provided an accelerated platform for evaluating intraparticle redox concentrations, the role of state of charge and conditioning on RAC performance. We used scanning electrochemical microscopy (SECM) with a 300 nm probe to image, isolate, and interrogate RACs between 0.83-1.2 μm diameter. Deep electrolysis of the particles evidenced capacity losses, but this conditioning simultaneously led to increased Coulombic efficiency. On the other hand, shallow cycling using voltammetry for over 150 cycles showed improved charge recovery and gradual changes in the particle's diffusional regimes. Raman spectroelectrochemistry on few RACs confirmed that degradation occurred upon deep cycling but that shallow cycling was not as detrimental, albeit with low capacity access. Our simulations further verified the internal concentration of RACs and suggested their porosity enabled solution redox active mediators to penetrate and titrate charge in their interior. The

Significant portions of this chapter are adapted and reprinted from two published articles within *Langmuir** and *ChemElectroChem*** with permission from the American Chemical Society, copyright 2017 and Wiley-VCH Verlag GmbH & Co. KgaA, copyright 2018. Z.T.G. conducted all experiments and simulations presented herein. K.H-B. provided experimental guidance and made the 3D figures.

*Gossage, Z.T.; Schorr, N.B.; Hernandez-Burgos, K.; Hui, J.; Simpson, B.H.; Montoto, E.C.; Rodríguez-López, J. "Interrogating Charge Storage on Redox Active Colloids via Combined Raman Spectroscopy and Scanning Electrochemical Microscopy." *Langmuir* **2017**, *33*(37), 9455-9463. DOI: 10.1021/acs.langmuir.7b01121

Gossage, Z.T.; Hernandez-Burgos, K.; Moore, J.S.; Rodríguez-López, J. "Impact of Charge Transport Dynamics and Conditioning on Cycling Efficiency within Single Redox Active Colloids." *ChemElectroChem* **2018*, 5*(20), 3006-3013. DOI: 10.1002/celc.201800736

methodologies presented herein provide a stepwise viewpoint of the progression of RAC function with cycling, linking bulk behavior with that of individual particles.

3.2 Introduction

There is an increasing demand for the development of grid-level electrical energy storage systems that readily adapt to different capacity and power needs.[1,2] Lithium-ion battery (LIB) technology is still the most mature and practical energy storage system with extensive commercial success and high volumetric energy densities.[3] However, current LIB technologies have cycle life limitations arising from the lithium intercalation mechanism[4] and there are concerns over the future demands for Li.[5] A promising alternative technology is the redox-flow battery (RFB), where soluble battery materials react at an electrode with prospects for extended cycle life of >10,000 cycles.[1,6] RFBs also have strong advantages including design flexibility, in which the energy and power output can be separately scaled to meet demands, and with an attractive cost with respect to lithium ion batteries.[2,7–9] These properties have driven a 'renaissance' in flow battery development.[10] Much of the recent effort has focused on new materials and system designs that enable a transition into organic solvents with higher energy densities.[2,8,11]

Redox active colloids (RACs), are emerging energy storage materials for size-exclusion redox flow batteries (SERFBs).[7,11–14] With billions of redox sites per particle, RACs attain high capacity per molecule and high structural tunability while exhibiting molecular-like electrochemical properties.[12] In SERFBs, RAC size is leveraged towards decreasing species crossover across nanoporous separators while alleviating the poor conductivity displayed by nonaqueous solvents.[15] RACs act as isolated reservoirs for charge, with a capacity determined by the particle size and the internal concentration of redox sites. However, the benefits and limitations of using a flowable particle for energy storage have not been fully elucidated. Because charge transport in RACs relies on pendant-to-pendant electron exchange, charge hopping dynamics dictate charge distribution within these particles. Therefore, it is essential to understand the factors

leading to swift capacity access.[11,16] Here we elucidate the properties of RACs for applications in SERFBs via single particle experiments.

RACs used in this study consist of an insulating and crosslinked polystyrene backbone decorated with viologen (V) pendants. Electron transfer at the electrode-particle interface and subsequent charge hopping enables particle electrolysis via the movement of charge between the oxidized (V^{2+}), and the reduced state (V^{+}).[12,17,18] Charge hopping on redox-active polymers has been investigated in solution,[19–21] as films on modified electrodes,[21,22] and with isolated molecules.[23] To be used in SERFBs, RACs are expected to reversibly cycle thousands of times while maintaining excellent Coulombic efficiency (CE) and high capacity retention.[1,6,7] Elucidating electron transfer on short and long-time scales is key to understanding the molecular traits that make a material successful for energy storage applications. Here, we utilized single particle measurements to provide an accelerated testing platform, conveniently reducing the complexity of the flow battery configuration, and focusing on electron transfer between the RAC and electrode.

Recently, X-ray[24] and transmission electron microscopy[25] techniques have been used to address charge percolation within ion intercalation (e. g. Li, Na, etc.) battery nanomaterials. However, obtaining quantitative electrochemical data from individual particles is rare. To date the majority of these single entity studies has focused on micron-sized particles for ion intercalation.[26–31] In this work, we explore immobilized single viologen RACs (between 0.83-1.2 μm in diameter) with electrochemical interrogation using nanoelectrodes and the scanning electrochemical microscope (SECM, Figure 3.1).[18,32–37] Through SECM feedback imaging, single RACs were located to make contact for direct electrochemical measurements. In our first study, we explored charge transfer at RACs (1.2 um diameter) that contained Cl^- counterions using cyclic voltammetry (CV) and potential-controlled bulk electrolysis (BE).[18] The Cl^- counterions helped adhere the RACs to an insulating surface within the organic electrolyte. In a following study, we

expanded our measurements for highly dispersible RACs containing PF_6^- counterions[12] by first applying an immobilization protocol. Cycling experiments revealed concentration and diffusional parameters, and changes in electron transfer behavior that were linked to conditioning, charge dynamics, and the RAC's SoC. Further, Raman spectroscopy allowed us to qualitatively track the V^+ content throughout BE cycling. These reports demonstrate advanced analytical methodologies that show how single particle reactivity progresses throughout cycling. They provide unprecedented insight into material design limitations for flowable, multi-electron, energy storage materials.

3.3 Materials and Methods

3.3.1 Chemicals and Materials

Viologen-based redox active colloids (RACs) with a dry diameter of 135±12 nm and 827±71 nm were prepared as described previously.[12] RACs containing either Cl^- or PF_6^- counterions were used in our experiments. Lithium tetrafluoroborate ($LiBF_4$ (Aldrich, 99.99 %)) and tetrabutyl ammonium hexafluorophosphate ($TBAPF_6$ (TCI, >98%)) were used as electrolytes in organic solutions. Potassium nitrate (KNO_3 (Fisher, >99%)) was used in all aqueous experiments. Ferrocene (Fc, Aldrich, 98%) was used as received as a redox mediator for the SECM imaging and contact experiments. All electrolyte solutions were prepared in either anhydrous dimethyl formamide (DMF, Sigma Aldrich) or HPLC grade water (Macron). SECM probes, including Wollaston electrodes (Goodfellow, purity 99.9%, 300 nm radius) and Pt ultramicroelectrodes (Goodfellow, purity 99.9%, 12.5 mm radius) were prepared as described in previous reports.[18,38]

3.3.2 Substrate Preparation

Glass coverslips (Ted Pella, 0.13–0.16 mm thick) were used as insulator substrates and Indium tin oxide (ITO) coverslips (SPI 15–30 W) or gold sputter-coated Si wafers were used as

conductive substrates. For single particle measurements, a 5-10 µL droplet of RACs in acetonitrile (0.05 mg/mL, previously dispersed through sonication) was casted onto the center of a glass substrate and allowed to dry under ambient conditions. The substrate was checked under an optical microscope (Zeiss) to confirm particle isolation. For Raman measurements, 10 mL from a RAC solution (0.7 mg/mL) was dispersed onto an ITO substrate. For RACs containing PF_6^-, we thermally treated at 200 °C for 5 mins and allowed to cool under ambient conditions before the experiment.

3.3.3 SECM Contact to Single Particles and Cycling Measurements

All electrochemical measurements were performed using a CHI920D Scanning Electrochemical Microscope (CH Instruments, Inc.). Measurements were performed inside an oxygen and moisture-free glovebox. For SECM procedures, a 300 nm Pt UME was used as a working electrode with a Pt wire as the counter electrode and Ag wire as a quasi-reference. The substrate was first leveled using a redox mediator and negative feedback. Then an SECM probe was approached to the substrate and positioned using the theory of Cornut and Lefrou.[39] We further used negative feedback while rastering the electrode across the surface for SECM imaging.[40] After discrete particles were identified via imaging, the electrode was positioned directly over the particle and verified via line scans. Contact to the particle was then made through a manual approach (100–300 nm steps toward the particle) with CVs (20 mV/s) taken at each step. Once the particle was contacted, as evaluated by a faradaic contribution from viologen reduction, CV was conducted at various scan rates. The steady-state current and total charge passed/ collected were then extracted after subtracting the background current obtained in the absence of particle contact. CA measurements were also recorded using a potential step to the first reduction process. CA data from single particles were compared with simulations using COMSOL (described below) or with the method proposed by Li et al.[41]

For RACs containing PF_6^-, the substrate was thermally treated setup in an SECM cell and transferred into the glovebox. The surface was leveled for SECM imaging using a Pt ultramicroelectrode (12.5 µm radius) with a Pt wire as the counter electrode and Ag wire as a quasi-reference. Thereafter a smaller SECM probe (300 nm radius) was approached to the substrate and positioned using the feedback mode and the theory of Cornut and Lefrou.[39,40,] Contact was made to discrete particles identified via imaging through a manual approach (100 nm steps toward the particle). Cycling was conducted using CV or potential-controlled CA. All potentials were converted to $Ag/AgNO_3$ using Fc as an internal reference.

3.3.4 Raman Measurements

The Raman microscope used in this study is an in-lab-constructed instrument as described previously.[18] Through the aid of a CCD camera (Thorlabs), a laser line from a 532 nm diode laser (Melles Griot) was focused with a 20X objective (Mitutoyo) to an ITO sample containing dropcasted RACs. Using micropositioners, the beam was focused to encompass multiple RACs on the ITO surface before eventual collection with a spectrometer from Ocean Optics QE Pro. A Pt wire counter electrode and a Ag/AgCl reference electrode (CH Instruments, Inc.) were used for all Raman measurements in a 100 mM KNO_3 aqueous solution. Raman measurements were taken continuously with an acquisition time of 5 s for each spectrum. In order to minimize oxygen interferences, the measurements were taken in solutions covered with Parafilm that had been purged with argon and left under an argon positive pressure blanket.

3.3.5 COMSOL Simulations

Simulations were completed using the Transport of Diluted Species module within COMSOL Multiphysics 4.4. For our simulations, we utilized a closed-boundary, 2-D axisymmetric geometry. The geometry consisted of a circle the same swollen size as the RAC used in the SECM experiment with a 300 nm electrode surface in contact with the RAC domain as described

previously.[18] As suggested in previous studies, we used Butler-Volmer to simulate electron transfer at the electrode surface and Fick's laws to govern electron hopping within the RAC.[42] For cycling simulations, we used the results from the previous simulations as the initial conditions for each subsequent simulation. Further details are provided in Appendix A.

3.4 Results

3.4.1 Scanning Electrochemical Microscopy on Single RACs containing Cl^-

Drop-casting from a dilute solution (0.1 mg/mL) was sufficient for isolating RACs on top of glass as shown in Figure 3.2a. The optical image shows individual particles with a dry diameter of 1.2 ± 0.2 μm (standard deviation, n = 34) for the RACs with Cl^-. SECM allowed us to position a 300 nm (radius) disk-shaped electrode above the particles at the surface. By using Fc as a redox mediator, we observed negative feedback, i.e., a decrease in current when approaching a glass substrate.[39,40] Negative feedback imaging allowed us to identify individual RAC particles and evaluate their size by using an edge-to-edge measurement from the SECM image. We found that the swollen diameter of the particles in DMF was 2.0 ± 0.5 μm (n = 34, Figure 3.2b). After contact with a particle with an SECM probe, the viologen within the RAC can be electrolyzed to explore intraparticle charge transfer.

In Figure 3.3, results of reducing a single particle on top of glass are shown after background subtraction. For this measurement we biased the SECM tip 180 mV more negative than the $E_{1/2}$ to ensure the quantitative reduction of V^{2+} to $V^{+}\cdot$. The chronoamperogram shows a current decay for a 300 s time interval. A best fit to this curve was obtained using two different models. The first model consisted of a modified bulk electrolysis procedure assuming a single contact point between a nanoelectrode and a particle which does not explicitly require assumptions about the intraparticle concentration. This model is based on the equation:[41]

$$i(t) = i_p \exp[-(4r_e D_{CT}/V)t] \quad (1)$$

where i_p is the maximum current after the potential step, r_e is the effective contact radius, D_{CT} is the charge transfer diffusion coefficient, V is the volume of the particle, and t is time. Using this method, we obtained a charge diffusion coefficient of 2.4×10^{-10} cm^2/s with a least-squares fit to a single exponential.

Following this initial analysis, finite element simulations using COMSOL Multiphysics were performed to gain a more precise understanding of charge transport within single RAC particles. In the COMSOL simulations, diffusion of the redox couple was simulated in a 2D axisymmetric domain representing a radial cross section of a spherical particle in contact with a nanoelectrode (Appendix A). At the boundary between the particle and the electrode, a zero concentration for V^{2+} was simulated and the current was extracted using a boundary probe. All other boundaries were insulating. Best fits were selected by eye for evaluating the effect of different diffusion coefficients on the simulated transients and in comparison to the experiment. A suitable profile for the current decay obtained via COMSOL using the diffusion coefficient from the first approach was obtained when using an intraparticle concentration of 1.25 M of V^{2+}. The concentration and diffusion coefficients we found are in good agreement with trends estimated previously through CV at a RAC monolayer electrode.[12] The larger diffusion coefficient of the 1.2 μm colloid was consistent with other RACs of various sizes.[12] The combination of methods reported here, and applied on a single particle, provides us with a strong degree of confidence on the accuracy of the charge properties determined for these RACs.

We confirmed the results from CA by performing CV in contact with another RAC (Figure 3.4), where intraparticle charge transfer diffusion is approximated via the steady state equation:[38,43,44]

$$i_{ss} = 4nFDaC \quad (2)$$

where i_{ss} is the measured steady state current, *n* is the number of electrons for the process, F is Faraday's constant, D is the diffusion coefficient, a is the radius of the electrode, and C is the concentration of the system. This is only an approximation, because diffusion in our experiment is restricted to the particle, while this equation applies for a semi-infinite boundary condition.[40] By using various scan rates (Figure 3.4b), we found deviation from steady-state behavior at scan rates below 20 mV/s, which exhibited a decreasing limited current upon reduction beyond E^0. This is likely related to the larger degree of electrolysis attained over the longer time required for this voltammogram to proceed, given the restricted geometry for the particle. By using the background-subtracted current for a relatively fast scan rate of 20 mV/s (Figure 3.4a) and the concentration derived from CA (1.25 M) a measurement of the electron diffusion through different RACs using the steady state, eq 2 was determined to be $(3 \times 10^{-10}) \pm (2 \times 10^{-10})$ cm^2/s (standard deviation for 9 particles). If we use the diffusion coefficient from our bulk electrolysis simulations and the average steady state current for a single particle we find an intraparticle concentration of 1.1 M. Within reasonable accuracy, these results are consistent and also on the same order of magnitude with previous bulk measurements.[12]

3.4.2 SECM Cycling of Single RACs containing PF_6^-

RACs containing PF_6^- are highly dispersible[12] in organic electrolyte compared to RACs paired with Cl^-. We explored the attachment of RACs containing PF_6^- to substrates (Figure 3.5), as otherwise they became mobile on the surface (Supporting Materials; DOI: 10.1002/celc.201800736). This characteristic is highly desirable for RFB materials, but also leads to poor adhesion to glass and conductive substrates. We observed a monotonic decay with dropcasted particles during CV cycling on a gold substrate, because the particles continually detached from the electrode (Figure 3.5b). Without any pretreatment, SECM cannot be used to image or make contact measurements to such particles. Therefore, an immobilization method is necessary to hold the RAC particles in place.[32,45] Thermal treatment seemed favorable for

adhesion of RACs due to their polymeric nature. We hypothesized that RACs could withstand a glass transition without degradation[46] of their redox activity. Heating at 400°C (Figure 3.5a) led to extensive morphological changes and poor electrochemistry (Figure 3.6). For all of our experiments with RACs containing PF_6^-, we chose a heat of 200°C for 5 minutes under ambient conditions.[47] This treatment produced well-adhered RACs that were morphologically similar to untreated RACs[12] and displayed CVs congruent with those obtained from untreated samples (Figure 3.5c). We believe the improved adhesion is related to greater contact area between the RACs and the substrate due to deformation of the RAC and the removal of surface species (e. g. volatiles, water) from the substrate. Furthermore, this additive free method showed only a slight improvement in the redox response as evidenced by a small change in the peak splitting between untreated and treated samples, Figure 3.5c.

With properly adhered RACs, we turned to SECM measurements of individual particles. As illustrated in Figure 3.1, we approached a sharpened SECM probe with an exposed Pt microdisc of 300 nm in radius toward a glass surface containing adhered RACs. Thereafter, SECM feedback imaging using ferrocene as mediator was used to find isolated particles (Figure 3.7a). We then aligned the SECM probe over the centroid of a chosen particle for approaching and making contact.[18] We stepped the probe toward the particle in 100 nm increments while using cyclic voltammetry (CV). Upon contact, we observed a faradaic current above the background, Figure 3.7b. CV on multiple particles allowed us to estimate the diffusion coefficient for charge transfer, D_{CT}, at $8 \times 10^{-11} \pm 3 \times 10^{-11}$ cm^2/s (n=7) based on equation 2. These values were in error with measured D_{CT} for the RACs containing Cl^- and in agreement with previous measurements on RAC monolayers.[12]

Upon confirming contact, we conducted cycling measurements with potential-controlled BE focused on high capacity access within the RAC containing PF_6^-. The RAC was reduced/oxidized for 60 s (Figure 3.7c-e) with 200 mV applied overpotential to approach full

electrolysis. Based on precedent work,[12,18] we assumed the RACs have a pendant concentration of 1 M and a theoretical capacity of 110 pC, leading to ~72% of the capacity accessed during the reduction cycle. Individual RACs may vary in pendent concentration and the actual access may be higher. Furthermore, the first charge/discharge cycle had a CE of 60%. Previous BE measurements on a RAC suspension of the same batch showed 78% CE for the first cycle and capacity loss upon further cycling.[12] Here, we have eliminated complications arising from a bulk setup, including material adsorption and precipitation on the electrode, crossover, and RAC-to-RAC charge transfer. Single particle measurements thus suggest that loss of capacity is innate to these RACs. Comparison to smaller RACs (80 and 137 nm) which exhibited more reversible electrolysis for up to 50 cycles[12] suggests that 830 nm RACs exhibit poorer charge percolation.[48] Nonetheless, simultaneous to a decreased charge accessibility upon cycling, we also observed an increased Coulombic efficiency that reached ~100%. Thus, irreversible processes and capacity fade occurred during the initial cycles, but cycling also conditioned the particles. This observation mirrors the behavior for BE and flow cell experiments for several types of RAC particles, where modest improvement of CE occurred in the early cycles.[12] This correlation gives us confidence that single particle experiments are relevant to the behavior of bulk RAC electrolytes.

Unfortunately, we could not continue BE experiments indefinitely since electrolysis led to an unexpected behavior. We speculate the inconsistent data in cycle 9 and 10 is due to loss of contact, with similar behavior observed in additional SECM experiments. Volumetric changes in RACs are known to occur between the charged and discharged state, so the mechanical impact could potentially lead to a loss of contact.[12] Since we cannot rule out that the behavior may simply reflect further material degradation, we turned to a milder charge/discharge technique via CV.

Voltammetric cycling over 150 cycles allowed us to probe capacity loss and charge transfer dynamics, Figure 3.8.[49,50] After SECM imaging (Figure 3.8a) and contact to a new particle,

we accessed the particle's redox at 50 mV/s (Figure 3.8b). Background subtraction (Figure 3.8c) revealed a quasisteady- state response, characterized by a non-uniform plateau. However, throughout 100 cycles, we observed a gradual progression toward a peak-shaped voltammogram (Figure 3.8c). A similar transition was observed when cycling an ultramicroelectrode (12.5 µm electrode radius) modified with few RACs (Figure 3.9). Peak-shaped CVs are characteristic of 1D linear diffusion, while sigmoidal CV shapes are observed under conditions leading to 2D hemispherical diffusion.[49,51,52] We speculate that this shape change implies a transition from a radial to a linear diffusional regime, likely related to the modification of charge transport pathways within the RAC and potentially linked to the conditioning behavior observed during the single RAC BE experiment. A vertical shift on the current axis suggested that over time charge became trapped in the particle, leading to a modified SoC. Coulometry (Figure 3.8d) showed a steep decrease in the charge passed during the first 10 cathodic sweeps. These experiments suggest that charge percolation within the particle involves CV reporting based on a "near-electrode" SoC (Figure 3.8e: I) while in time some charge becomes inaccessible to CV due to diffusion into the bulk particle (Figure 3.8e: II–III).

Finite element simulations using COMSOL Multiphysics software (Figure 3.10 and further details in Appendix A) provided an excellent framework to investigate our hypotheses and to determine the impact of cycling on SoC. We designed a 2-D axisymmetric domain with the size and geometry of the RAC used in the SECM experiment (1.3 mm diameter) with a 300 nm electrode contact.[18] We recreated Butler-Volmer kinetics to simulate electron transfer at the electrode surface and Fick's laws of diffusion to recreate charge diffusion within the RAC.[42] Our simulations showed that as the SoC increased, the CV shifted downward on the current axis (Figure 3.10a) with no impact on the CV shape. Although we were not able to quantitatively recreate the quasi steady-state shape or current level observed experimentally, these simulations allowed us to evaluate charge distribution in the RAC.

CV simulations (Figure 3.10b) confirmed that the bulk SoC was inhomogeneous and changed with subsequent cycles due to charge trapping (Figure 3.10c). For example, these inhomogeneities caused the CV response at the 3rd and 8th cycles to exhibit current levels similar to those for particles with an otherwise homogeneous SoC of 25% and 50%, respectively (Figure 3.10b). While the electrode accesses V^+ in its vicinity, the particle's SoC away from the contact changed at a slower pace (Figure 3.11), effectively mirroring our experimental CV (Figure 3.8c-e). Ultimately, our results suggest SoC only played a large role in the early cycles and the observed CV changes in our experiment are more complex. We also speculate that charge trapping might lead to changes in conductivity across the particle.[48] Given this dynamic behavior, with potential differences on short and long time scales, we pursued additional methodologies to further interpret our single particle results.

3.4.3 Raman Spectroscopy on few RACs containing PF_6^-

Raman spectroscopy is a powerful aid in tracking V^+ within RACs during cycling.[53,54] We evaluated heat-treated RACs on a transparent ITO surface (Figure 3.12a) in Ar-purged aqueous KNO_3. While reducing the RACs with CV, we observed clear development and loss of three Raman peaks ascribed to V^+ (Figure 3.12b).[18,53,55] All the peak intensities followed the same trend with applied voltage and showed similar behavior to previous measurements on RAC monolayer films.[18] However, CVs performed on 830 nm RACs at 20 mV/s evidenced a residual Raman signal due to trapped V^+ at the end of the scan (Figure 3.12b, top curve), corroborating the single particle CV cycling and simulations.

When bulk electrolyzing the RACs, we observed a steady signal intensity after 15 s and no apparent degradation while in the charged state. In contrast, cycling led to capacity fade (Figure 3.13) and intensity loss in the first few cycles (Figure 3.12c). For these measurements, only the peak intensity for the strongest peak, 1530 cm^{-1}, was tracked with a 5 s acquisition time. Electrolyzing the RACs with long 60 s steps (Figure 3.12c) showed strong fluctuations between a

saturated peak intensity and complete disappearance of the peak back to baseline each cycle. Thus, the irreversible capacity losses observed seem to be caused by the cycling process and directly involve loss of access to viologen species within the RAC. The same decaying trend was observed in another electrolysis experiment following the Raman shift with a 60X objective. However, our measurements show the Raman signal repeatedly depletes to background meaning the species are not extensively trapped in the V^+ state at the end of each cycle and this implies the trapped state is not the culprit for the observed capacity fade. The RACs showed an average reduction time of 15 ± 3.5 s to reach a saturated Raman signal, and a longer 40 ± 5 s to completely return the signal to background. This lag suggests that bulk oxidation of the RAC was consistently slower than its reduction and has been observed with bulk cycling of redox active polymers[14] and RACs.[12] Viologen redox-active polymers are expected to eject counterions during reduction[56,57] and our results could be explained as a higher difficulty for ion reentry during re-oxidation. Ion diffusion into the RAC may be slow due to rearrangement of the structure or static effects from the particle being highly charged.

Thereafter, we evaluated the effect of electrolysis time on charge transfer within the RAC (Figure 3.12d). By controlling the electrolysis time, we can mimic the effect of electrode collision time on capacity access within a RAC, as it occurs in flow batteries. We can probe this concept by controlling the length of time that electrons are transferred to and from the RAC via the length of the potential step. We continued from the 60 s time steps with the same sample to evaluate smaller electrolysis steps on the Raman signal. Charge trapping had a large impact on electron recovery when electrolysis times were low (Figure 3.12d). For instance, the Raman signal for cycling with 5 s steps, Figure 3.12d (blue curve), was nearly invariable due to gradual accumulation of trapped V^+ and this was also reflected with a continual increase in CE (Figure 3.14). For both 5 and 10 s cycling, we observed the development of Raman peaks that never fully returned to baseline while long electrolysis times (60 s) led to more consistent CE (Figure 3.14).

In a RFB, charge trapping could potentially be problematic with slow charge/discharge processes. From a practical standpoint, this would be undesirable and would limit capacity access per unit time and possibly require multiple electrode collisions during a charge/discharge cycle for full capacity access of a given particle. However, it is interesting that 10 s cycling did show consistent fluctuations without additional degradation (Figure 3.12d). This apparent stabilization resembles that exhibited by Li cathode materials that perform better by avoiding very high SoC.[58] Likewise, a recent report found direct correlation between the SoC of quinone derivatives for aqueous flow batteries to their decomposition rate.[59] Altogether, single- and few- particle results suggest that stability and access to charge in RACs are also dependent on SoC. Thus, research and material development should focus on pinpointing structure-property relationships that enable reversible and full capacity access without risking particle degradation.

3.5 Conclusions

We explored the electrochemical properties of individual viologen redox-active colloids, revealing fundamental electrochemical information and the impact of cycling, conditioning, and state of charge on particle performance. SECM imaging was used to locate individual particles, while single particle interrogation via contact with a 300 nm electrode was used to access charge using voltammetric and chronoamperometric perturbations. We quantified charge diffusion within RACs through our own models built in COMSOL and reported equations. Cycling RACs containing PF_6^- indicated a low access of 72% of the theoretical capacity, in line with reported experiments on bulk dispersions.[12] Continued particle cycling exhibited two opposite behaviors: while initial cycles displayed an irreversible capacity loss, the Coulombic efficiency increased with cycle number. A change in the charge transport mode within individual RACs was evident upon CV cycling. COMSOL simulations helped discern effects derived from capacity loss from those of charge trapping and inhomogeneous charge distribution within the particle. Likewise, Raman spectroscopy proved to be an excellent tool for tracking capacity loss during cycling. It confirmed

that RAC degradation was directly caused by deep cycling and the capacity loss did not specifically involve trapped V^{+}.

In all, our single particle measurements combined with Raman provided a much clearer picture of charge transport in RACs, their cycling capabilities and degradation processes that were not obtained with previous bulk analyses. The methodology used here provided a stepwise viewpoint of the progression of RAC function with cycling, linking bulk behavior with that of individual particles. These studies suggest future research directions to explore RACs of smaller sizes and to pinpoint key structure-property relationships that will lead to higher internal D_{CT}, higher CE, and faster electron transfer rates. These characteristics will be important for next-generation materials that harness the full potential of particles with multiple redox sites.

3.6 Acknowledgements

This work was supported as part of the Joint Center for Energy Storage Research (JCESR), an Energy Innovation Hub funded by the U.S. Department of Energy, Office of Science, Basic Energy Sciences. Sample characterization was carried out in part in the Materials Research Laboratory Central Research Facilities and the Beckman Institute for Advanced Science and Technology, University of Illinois. K.H.B. gratefully acknowledges the Arnold and Mabel Beckman Foundation for a Beckman Institute Postdoctoral Fellowship. E.C.M. acknowledges support by the Ford Foundation Fellowship Program. J.R.-L. acknowledges support from the 2015 SACP Starter Grant for the construction of the experimental Raman microscope-SECM setup used in this work and a Research Fellowship from the Alfred P. Sloan Research Foundation. The authors thank Mr. Kevin Cheng for providing synthetic guidance and samples of RACs for the experiments reported here.

3.7 Figures

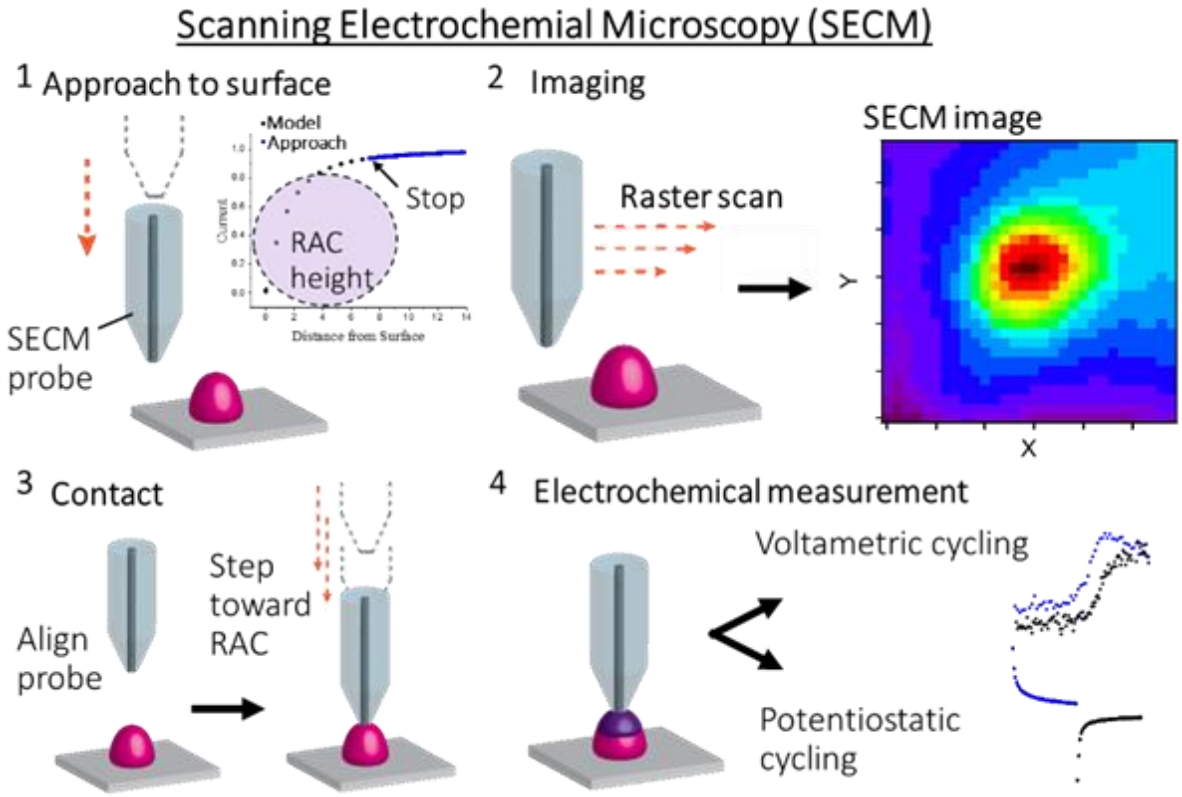

Figure 3.1. Methodology for single particle cycling. *Substrate Preparation*: (1) RACs were dispersed in MeCN and dropcasted onto a glass substrate, (2) allowed to dry, (3) and then heated and cooled under ambient conditions. *SECM Procedures*: (1) An SECM probe (300 nm radius) was brought to the surface using a redox mediator and feedback theory for positioning. It was positioned 2.1 µm away from the surface to accommodate the RAC swollen height (~1.3 µm). (2) RACs were imaged through raster scanning. (3) Contact to the RACs was made by aligning the probe via the SECM image, then moving in 100 nm steps toward the RAC. (4) Electrochemical cycling measurements were conducted on the single RAC.

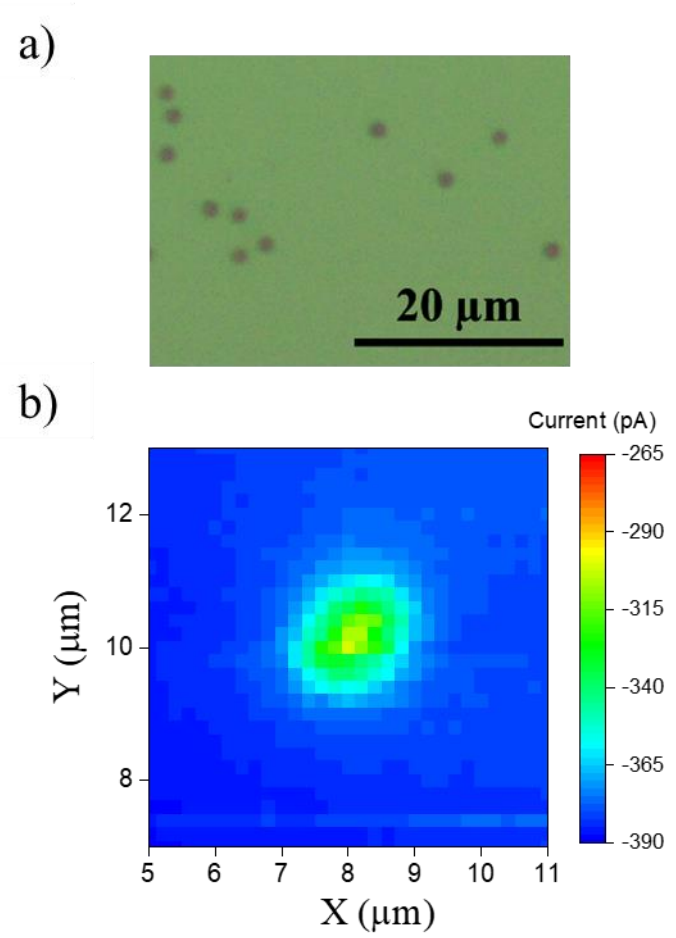

Figure 3.2. (a) Optical microscopy of RACs on glass after drop-casting. (b) SECM imaging of a single RAC on glass using negative feedback.

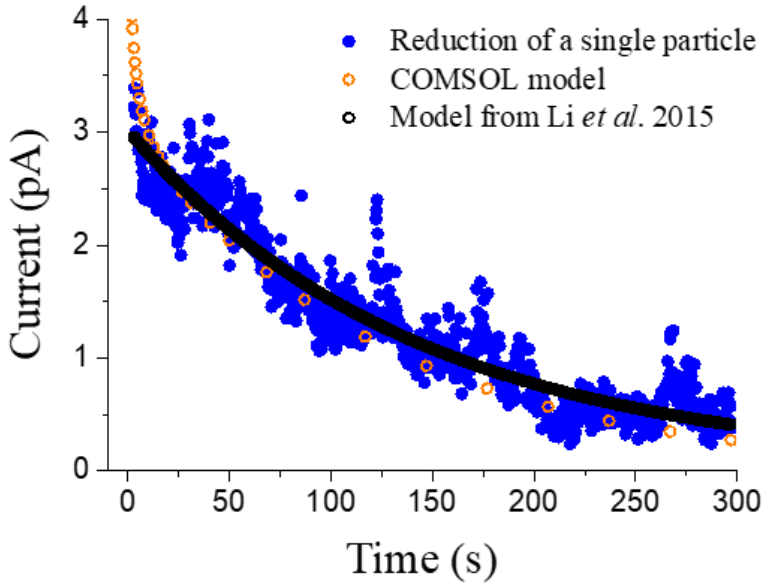

Figure 3.3. Background subtracted CA reduction of single particle on glass substrate in DMF after making contact with an SECM electrode. One fitting is based on a COMSOL model (orange curve) that allows particle size, mediator concentration, and D_{EX} to be defined. The other fitting, black curve, is based on an exponential model previously described by Li et al.[41]

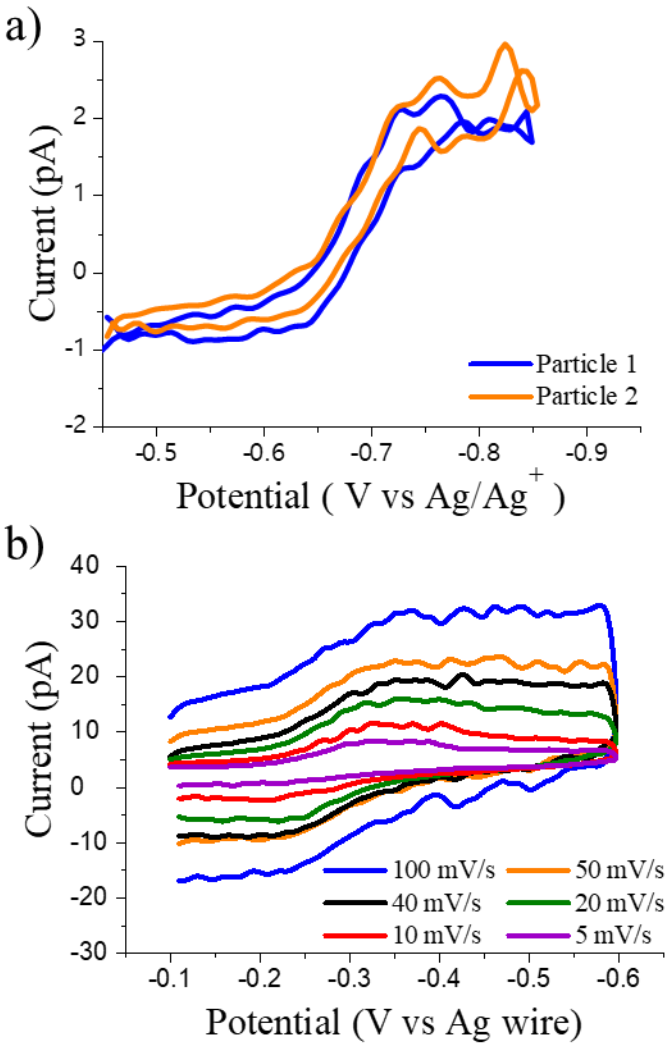

Figure 3.4. (a) CV at 20 mV/s on two single RAC particles (2 μm diameter) after background subtraction. (b) Scan rate dependence of CV when in contact with a single particle.

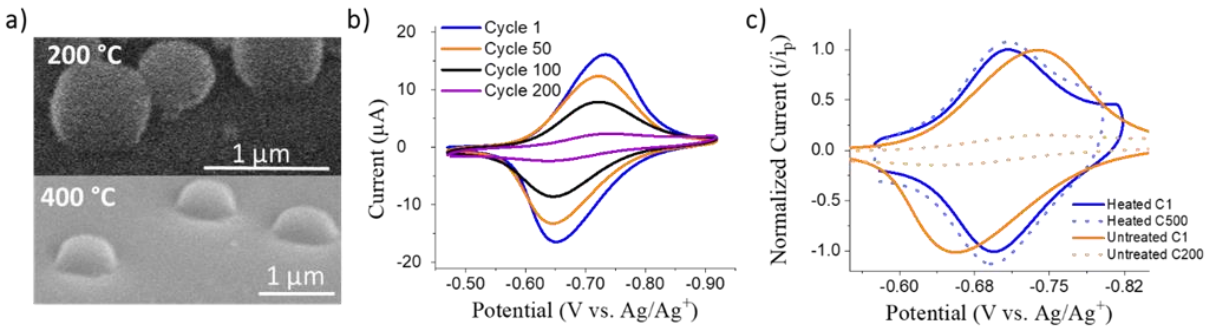

Figure 3.5. Heat treatment for improving RAC adhesion. (a) SEM images of RACs after heating for 5 minutes at 150 and 400 °C. (b) Continuous CV of 135 nm RACs dropcasted on a large gold electrode (1 mm radius) without heat treatment. (c) Comparison of CV for heated (200 °C, 5 min. under ambient conditions) and untreated RACs. The currents were normalized to minimize differences due solely to the number of RACs on a given sample. The cycle number is indicated with 'C' in the legend. All scans at 20 mV/s in 0.1 M $LiBF_4$ in DMF.

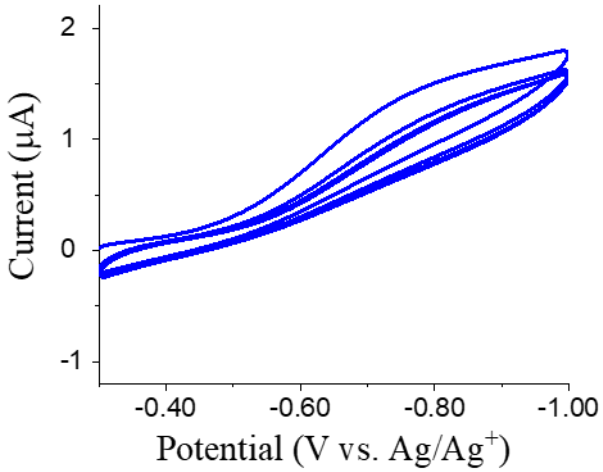

Figure 3.6. CV of 830 nm RACs on gold that were treated at 400 °C for 5 minutes. The CV was taken at 50 mV/s in 0.1 M LiBF4 in DMF.

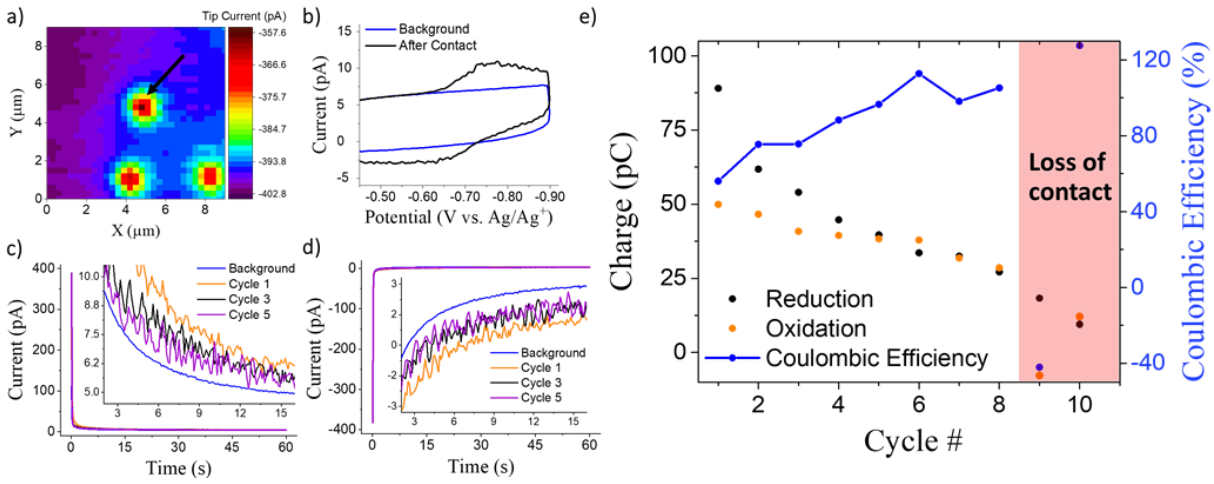

Figure 3.7. Potentiostatic bulk electrolysis cycling of a single RAC. (a) SECM image of three isolated RACs using negative feedback with ferrocene. Black arrow indicates the RAC chosen for contact. (b) SECM probe CV before (blue curve) and after (black curve) contact with the RAC at a scan rate of 20 mV/s. Measured current during (c) reduction and (d) oxidation of a single RAC in potentiostatic cycling for 60 s. Select regions are shown in the respective insets for better clarity. (e) Coulometry for the single RAC BE. The CE trend is shown with the right axis. All measurements were conducted in 0.1 M $LiBF_4$ in DMF.

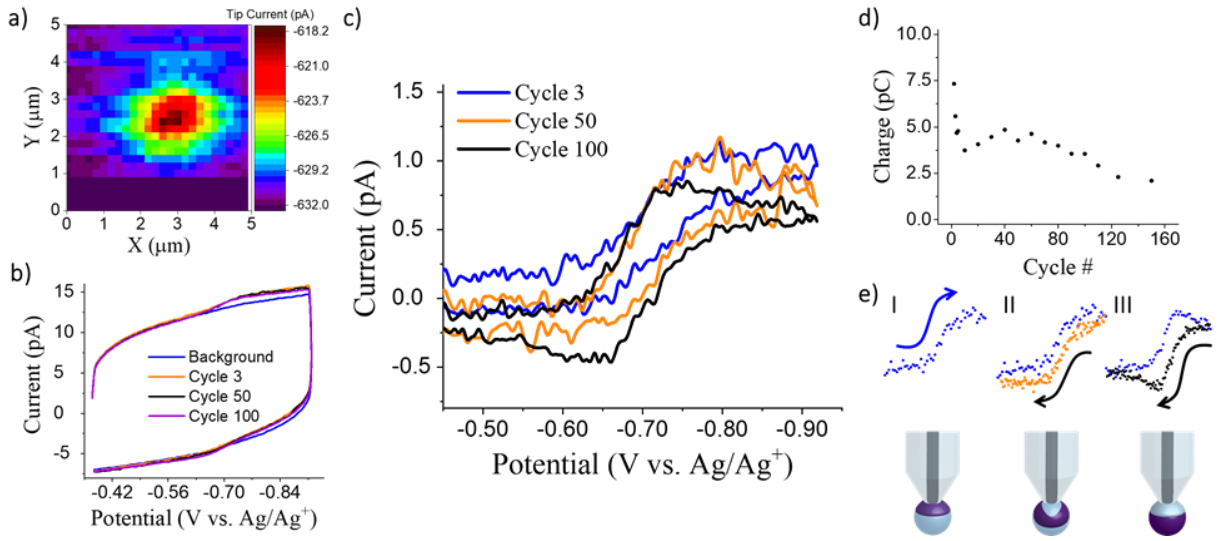

Figure 3.8. Voltammetric cycling of a single RAC. (a) SECM image of the single RAC using negative feedback. (b) Raw RAC CV-cycling data with the background measured before contact. (c) Background-subtracted CV for select cycles. (d) Coulometry for each forward (reduction) sweep during the CV cycling experiment. (e) Diagram showing a proposed sequence of events leading to changes in CV shape from inhomogeneous charge distribution within the RAC particle. A 50 mV/s scan rate was used for all measurements in 0.1 M $LiBF_4$ in DMF.

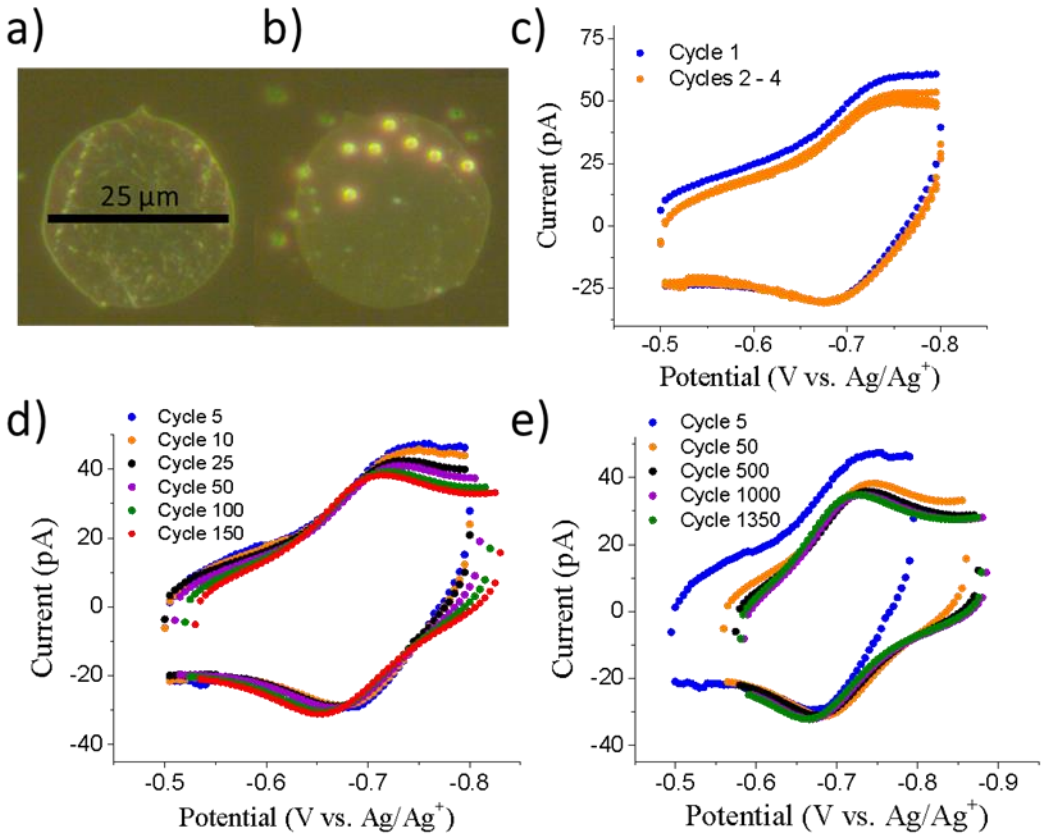

Figure 3.9. CV-cycling with RAC-modified UMEs. (a) Polished Pt UME (12.5 µm radius). (b) Pt UME after dropcasting and heat treatment. (c) CV cycle 1 (blue curve) and cycle 2-5 (orange curves) for the RACUME submerged in 0.1 M LiBF4 in DMF. (d) Change in CV shape during the first 150 cycles using a 7- particle RAC-UME. (e) Comparison of select curves throughout 1350 CV cycles. All measurements were conducted in 0.1 M LiBF4 in DMF.

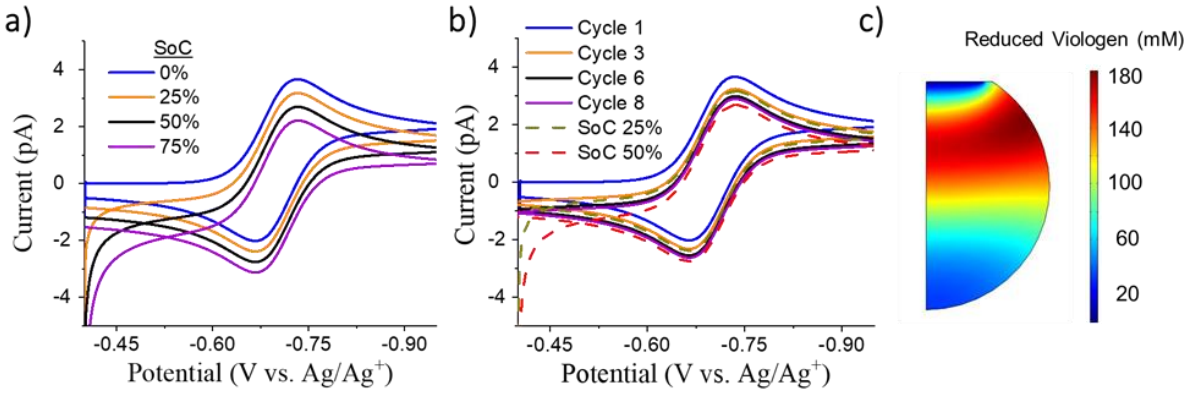

Figure 3.10. COMSOL simulations of single RAC CV-Cycling. (a) Simulations of CV on a RAC with different SoC. (b) CV dependence on cycle number. Dotted lines are fittings for SoC at 25% and 50%. (c) Profile of V^+ content at the end of the first cycle (2D with symmetry axis projection).

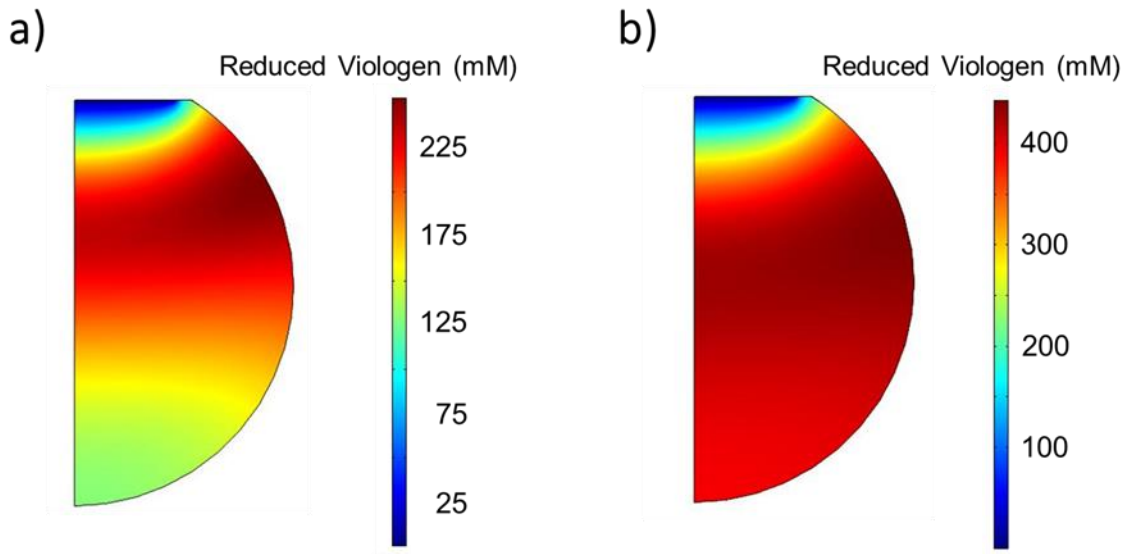

Figure 3.11. COMSOL simulations of charge trapping during CV-cycling**.** 2-D distribution of V^+ in the RAC at the beginning of cycle 3 (a) and cycle 8 (b).

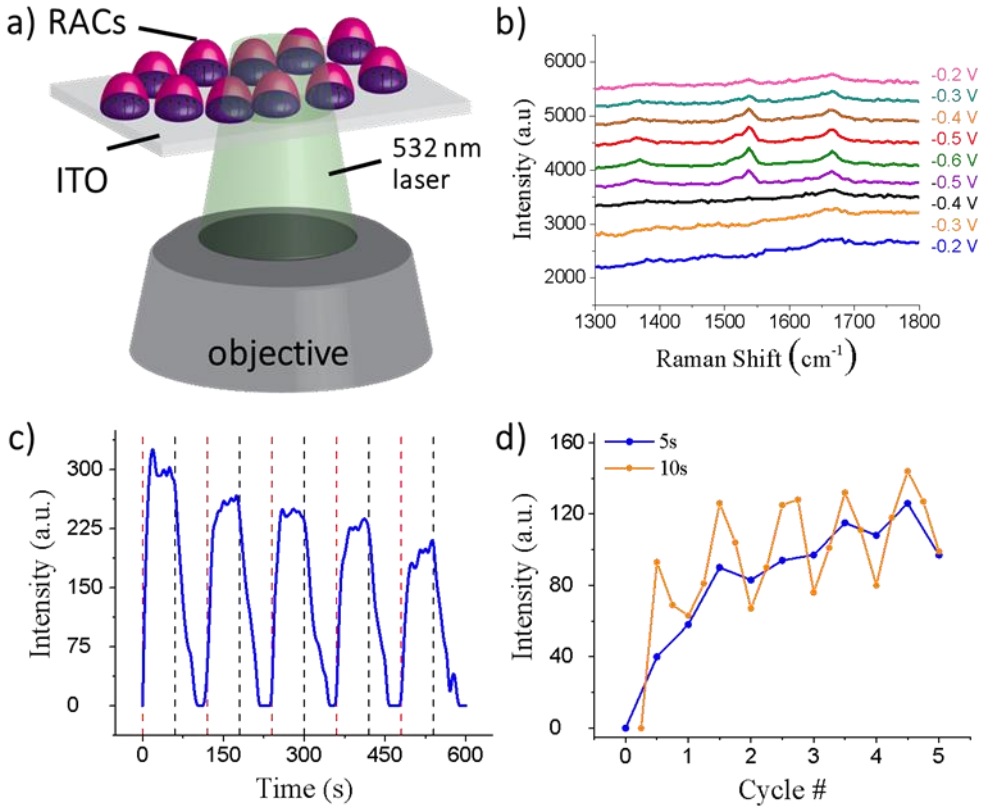

Figure 3.12. Tracking of V^{+} with Raman during RAC Cycling**.** (a) Diagram of Raman measurements on large RACs dropcasted as a single layer on an ITO substrate. Many particles are being reduced providing a substantial electrochemical signal while a select area is evaluated via Raman. (b) Raman measurement for select potentials during CV at 20 mV/s. (c) 1530 cm^{-1} peak intensity fluctuation during BE cycling of dropcasted RACs with potential step times of 60 s. Red and black dashed lines indicate the start of the reduction and oxidation steps, respectively. (d) Fluctuation in peak intensity for the 1530 cm^{-1} peaks while electrolyzing the RACs with 5 and 10s time steps.

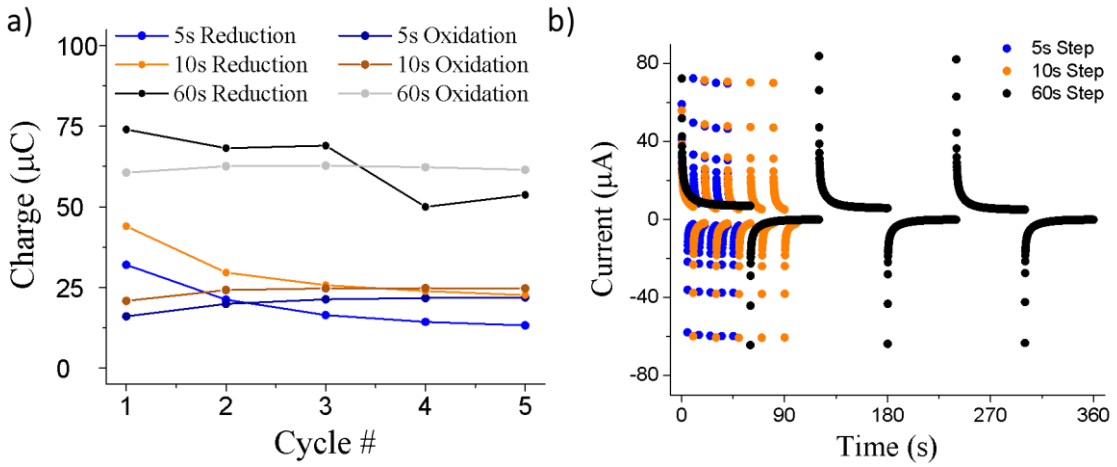

Figure 3.13. Varied RAC electrolysis times and coulometry. (a) Coulometry and (b) raw electrochemical data for select cycles during electrolysis of RACs on ITO for various time steps. All measurements collected in an aqueous 0.1 M KNO_3 electrolyte with >150 mV applied overpotential.

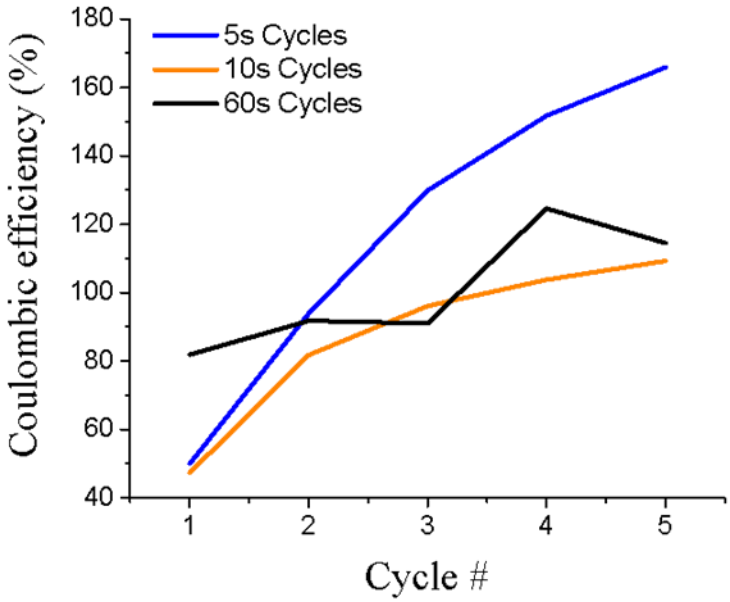

Figure 3.14. Progression of CE throughout cycling with various potential step times for BE.

3.8 References

(1) Y. A. Gandomi, D. S. Aaron, J. R. Houser, M. C. Daugherty, J. T. Clement, A. M. Pezeshki, T. Y. Ertugrul, D. P. Moseley, M. M. Mench, *J. Electrochem. Soc*. **2018**, 165, A970-A1010.

(2) G. L. Soloveichik, *Chem. Rev*. **2015**, 115, 11533–11558.

(3) J. W. Choi, D. Aurbach, *Nat. Rev. Mater*. **2016**, 1, 16013.

(4) Y. Zhao, Y. Ding, Y. Li, L. Peng, H. R. Byon, J. B. Goodenough, G. Yu, *Chem. Soc. Rev*. **2015**, 44, 7968–7996.

(5) D. Larcher, J.-M. Tarascon, *Nat. Chem*. **2015**, 7, 19–29.

(6) B. Dunn, H. Kamath, J.-M. Tarascon, *Science*. **2011**, 334, 928–935.

(7) M. Park, J. Ryu, W. Wang, J. Cho, *Nat. Rev. Mater*. **2017**, 2, 16080.

(8) J. Winsberg, T. Hagemann, T. Janoschka, M. D. Hager, U. S. Schubert, *Angew. Chem*. **2017**, 129, 702–729.

(9) T. B. Schon, B. T. McAllister, P.-F. Li, D. S. Seferos, *Chem. Soc. Rev*. **2016**, 45, 6345–6404.

(10) M. L. Perry, A. Z. Weber, *J. Electrochem. Soc*. **2016**, 163, A5064-A5067.

(11) M. Burgess, J. S. Moore, J. Rodríguez-López, *Acc. Chem. Res*. **2016**, 49, 2649–2657.

(12) E. C. Montoto, *et al*., *J. Am. Chem. Soc*. **2016**, 138, 13230–13237.

(13) T. Janoschka, N. Martin, U. Martin, C. Friebe, S. Morgenstern, H. Hiller, M. D. Hager, U. S. Schubert, *Nature*. **2015**, 527, 78–81.

(14) G. Nagarjuna, J. Hui, K. J. Cheng, T. Lichtenstein, M. Shen, J. S. Moore, J. Rodríguez-López, *J. Am. Chem. Soc*. **2014**, 136, 16309–16316.

(15) E. C. Montoto, G. Nagarjuna, J. S. Moore, J. Rodríguez-López, *J. Electrochem. Soc*. **2017**, 164, A1688–A1694.

(16) M. Burgess, E. Chénard, K. Hernández-Burgos, G. Nagarjuna, R. S. Assary, J. Hui, J. S. Moore, J. Rodríguez-López, *Chem. Mater*. **2016**, 28, 7362–7374.

(17) C. L. Bird, A. T. Kuhn, *Chem. Soc. Rev*. **1981**, 10, 49–82.

(18) Z. T. Gossage, N. B. Schorr, K. Hernández-Burgos, J. Hui, B. H. Simpson, E. C. Montoto, J. Rodríguez-López, *Langmuir*. **2017**, 33, 9455–9463.

(19) J. B. Flanagan, S. Margel, A. J. Bard, F. C. Anson, *J. Am. Chem. Soc*. **1978**, 100, 4248–4253.

(20) M. Burgess, K. Hernández-Burgos, B. H. Simpson, T. Lichtenstein, S. Avetian, G. Nagarjuna, K. J. Cheng, J. S. Moore, J. Rodríguez-López, *J. Electrochem. Soc*. **2016**, 163, H3006–H3013.

(21) C. M. Casado, I. Cuadrado, M. Mor_n, B. Alonso, B. Garcia, B. Gonzalez, J. Losada, *Coord. Chem. Rev*. **1999**, 185, 53–80.

(22) F. R. F. Fan, M. V. Mirkin, A. J. Bard, *J. Phys. Chem*. **1994**, 98, 1475–1481.

(23) R. E. Palacios, F.-R. F. Fan, A. J. Bard, P. F. Barbara, *J. Am. Chem. Soc*. **2006**, 128, 9028–9029.

(24) M. Wolf, B. M. May, J. Cabana, *Chem. Mater*. **2017**, 29, 3347–3362.

(25) Y. Liu, F. Fan, J. Wang, Y. Liu, H. Chen, K. L. Jungjohann, Y. Xu, Y. Zhu, D. Bigio, T. Zhu, *Nano Lett*. **2014**, 14, 3445–3452.

(26) A. J. J. Jebaraj, D. A. Scherson, *Acc. Chem. Res*. **2013**, 46, 1192–1205.

(27) J. Lim, Y. Li, D. H. Alsem, H. So, S. C. Lee, P. Bai, D. A. Cogswell, X. Liu, N. Jin, Y.-s. Yu, *Science*. **2016**, 353, 566–571.

(28) Y. Takahashi, A. Kumatani, H. Munakata, H. Inomata, K. Ito, K. Ino, H. Shiku, P. R. Unwin, Y. E. Korchev, K. Kanamura, *Nat. Commun*. **2014**, 5, 5450.

(29) K. Dokko, N. Nakata, Y. Suzuki, K. Kanamura, *J. Phys. Chem. C*. **2010**, 114, 8646–8650.

(30) K. Dokko, Q. Shi, I. C. Stefan, D. A. Scherson, *J. Phys. Chem. B*. **2003**, 107, 12549–12554.

(31) S. Waki, K. Dokko, T. Matsue, I. Uchida, *Denki Kagaku*. **1997**, 65, 954–962.

(32) P.-Y. Blanchard, T. Sun, Y. Yu, Z. Wei, H. Matsui, M. V. Mirkin, *Langmuir*. **2016**, 32, 2500–2508.

(33) Y. Yu, T. Sun, M. V. Mirkin, *Anal. Chem*. **2015**, 87, 7446–7453.

(34) M. A. O'Connell, A. J. Wain, *Anal. Chem*. **2014**, 86, 12100–12107.

(35) S. M. Oja, Y. Fan, C. M. Armstrong, P. Defnet, B. Zhang, *Anal. Chem*. **2015**, 88, 414–430.

(36) S. C. S. Lai, J. V. Macpherson, P. R. Unwin, *MRS Bull*. **2012**, 37, 668–674.

(37) J. Kim, C. Renault, N. Nioradze, N. y. Arroyo-Currás, K. C. Leonard, A. J. Bard, *Anal. Chem*. **2016**, 88, 10284–10289.

(38) A. J. Bard, F. R. F. Fan, J. Kwak, O. Lev, *Anal. Chem*. **1989**, 61, 132–138.

(39) R. Cornut, C. Lefrou, *J. Electroanal. Chem*. **2007**, 608, 59–66.

(40) Bard, A. J.; Mirkin, M. V. *Scanning electrochemical microscopy*; CRC Press, **2012**.

(41) Li, Y.; Deng, H.; Dick, J. E.; Bard, A. *J. Anal. Chem*. **2015**, 87 (21), 11013−11021.

(42) M. E. G. Lyons in *Electroactive Polymer Electrochemistry*, Plenum Press, New York, **1994**, 1–235.

(43) Wightman, R. M.; Wipf, D. 0. In *Electroanalytical Chemistry*; Bard, A. J., Ed.; Marcel Dekker: New York, **1988**; Vol 15

(44) C. Lefrou, *J. Electroanal. Chem*. **2006**, 592, 103–112.

(45) M. L. Kromer, J. Monzo, M. J. Lawrence, A. Kolodziej, Z. T. Gossage, B. H. Simpson, S. Morandi, A. Yanson, J. Rodríguez-López, P. Rodríguez, *Langmuir*. **2017**, 33, 13295–13302.

(46) C. E. Carraher Jr in *Introduction to Polymer Chemistry*, CRC press, **2017**.

(47) P. Hanarp, M. Käll, D. S. Sutherland, *J. Phys. Chem. B*. **2003**, 107, 5768–5772.

(48) C. Karlsson, T. Suga, H. Nishide, *ACS Appl. Mater. Interfaces* **2017**, 9, 10692–10698.

(49) A. J. Bard, L. R. Faulkner in *Electrochemical Methods: Fundamentals and Applications*, Vol. 2, John Wiley & Sons, **2001**.

(50) S. Ching, R. Dudek, E. Tabet, *J. Chem. Educ*. **1994**, 71, 602.

(51) R. M. Wightman, *Science*. **1988**, 240, 415–420.

(52) N. M. Elgrishi, K. J. Rountree, B. D. McCarthy, E. S. Rountree, T. T. Eisenhart, J. L. Dempsey, *J. Chem. Educ*. **2017**, 95, 197–206.

(53) C. A. Melendres, P. C. Lee, D. Meisel, *J. Electrochem. Soc.* **1983**, 130, 1523–1527.

(54) P. Rostron, S. Gaber, D. Gaber, *Int. J. Eng. Trans. A* **2016**, 21, 24.

(55) B. Liu, A. Blaszczyk, M. Mayor, T. Wandlowski, *ACS Nano*. **2011**, 5, 5662–5672.

(56) N. Sano, W. Tomita, S. Hara, C.-M. Min, J.-S. Lee, K. Oyaizu, H. Nishide, *ACS Appl. Mater. Interfaces* **2013**, 5, 1355–1361.

(57) E. F. Dalton, R. W. Murray, *J. Phys. Chem*. **1991**, 95, 6383–6389.

(58) N. Nitta, F. Wu, J. T. Lee, G. Yushin, *Mater. Today*. **2015**, 18, 252–264.

(59) M.-A. Goulet, M. J. Aziz, *J. Electrochem. Soc*. **2018**, 165, A1466-A1477.

CHAPTER 4

Probing the Reversibility and Kinetics of Li^+ during SEI Formation and (De)intercalation on Edge Plane Graphite using Ion-sensitive Scanning Electrochemical Microscopy

4.1 Abstract

Ions at battery interfaces, such as Li^+, participate in both the solid-electrolyte interphase (SEI) formation and the subsequent energy storage mechanism. However, few *in situ* methods can directly track interfacial Li^+ dynamics. Herein, we report on scanning electrochemical microscopy with Li^+ sensitive probes for its *in situ*, localized tracking during SEI formation and intercalation. We followed the potential-dependent reactivity of edge plane graphite influenced by the interfacial consumption of Li^+ by competing processes. Cycling in the SEI formation region revealed reversible ionic processes ascribed to surface redox, as well as irreversible SEI formation. Cycling at more negative potentials activated reversible (de)intercalation. Modeling the ion-sensitive probe response yielded Li^+ intercalation rate constants between 10^{-4} to 10^{-5} cm s^{-1}. Our studies allow decoupling of charge-transfer steps at complex battery interfaces and create opportunities for interrogating reactivity at individual sites.

4.2 Introduction

Understanding fundamental charge transfer at interphases is a research priority for enabling better energy storage technologies.[1–3] In high energy density anodes, such as carbon and silicon, heterogeneous charge-mediating interphases determine electrode cycling performance, materials utilization, and risk for failure.[1] The solid electrolyte interphase (SEI) plays

This chapter is adapted and reprinted from an original research article in *Chemical Science** with permission from the Royal Society of Chemistry, copyright 2019. Z.T.G. conducted the experiments, made the figures and wrote the publication. J.H. helped with writing and Raman measurements. Y.Z. and H.F-Z. helped with substrate and electrode preparation.

*Gossage, Z.T.; Hui, J.; Zeng, Y.; Flores-Zuleta, H.; Rodríguez-López, J. "Probing the reversibility and kinetics of Li^+ during SEI formation and (de)intercalation on edge plane graphite using ion-sensitive scanning electrochemical microscopy." *Chem. Sci.*, **2019**, *10*, 10749-10754. DOI: 10.1039/C9SC03569A.

a major role in the ability of lithium-ion batteries (LIBs) to operate in a reliable manner.[1,2] The SEI components and properties are derived from electrolyte decomposition reactions at the surface of the anode, resulting in a morphologically and chemically heterogeneous structure.[2,4–7] Materials characterization methods have led to improved understanding of the components and precursors involved in the SEI,[1,2,8,9] on the observation of its reactivity and morphological changes during formation,[10,11] and tracking of the intercalation process.[12–14] On the other hand, there are few in situ methods capable of tracking interfacial alkali ions (e.g. Li^+)[15] and the impact of SEI progressive growth on their response.

Ions at the electrode–electrolyte interface play a key role in both SEI formation and the subsequent energy storage mechanism. Thus, structural heterogeneity may lead to reactive heterogeneity, ultimately affecting local ionic fluxes and cycling performance at differentiated sites.[16,17] Several groups have successfully relied on tracking atomic states or phase change to infer Li^+ movement throughout bulk electrode materials,[13,14,18,19] but the extension of this analysis to the SEI is not easily attainable due to its thickness (typically <100 nm), variable molecular content, and amorphous nature.[1] Ultimately, direct and localized quantification of Li^+ is desirable to provide key insight into ion intercalation kinetics, the ion diffusion mechanism through the SEI, localized heterogeneities, and SEI dynamics during charge/discharge.

The unique aspect of the analytical approach presented here comes from accurately measuring the local Li^+ response[20] as SEI formation and (de)intercalation reactions occur at the anode.[21–23] Emerging ion-sensitive scanning probe methods (SPMs) show great potential for understanding processes at functioning electrodes to guide development of next-generation energy storage technologies.[2,24–26] Scanning electrochemical microscopy (SECM) is a highly versatile SPM that is capable of acquiring both ionic and electronic information at an electrode surface within real battery environments.[2,27] However, quantitative ionic measurements require specialized probes and are far less common among SECM studies.[21,23,24] Recently, our group

applied Hg probes to detect ion fluxes into multi-layered graphene (MLG)[23] and patterned highly-oriented pyrolytic graphite (HOPG).[21] Recent work in our lab regarding probe fabrication and positioning[22] has dramatically improved their performance, enabling exciting directions in the exploration of ion dynamics on activated battery electrodes.

In this work, we used redox and ion-sensitive modes of SECM to track Li^+ flux during SEI formation at the edge site of HOPG. HOPG is a model carbon material that enables the straightforward selection of the Li^+ intercalation sites, i.e. the edge plane, for its characterization.[28–30] We used HOPG substrates with the edge plane sealed between two pieces of low-density polyethylene (LDPE) as described in Figure 4.1. The edge plane is the predominant site for (de)intercalation in graphitic materials,[31–33] showing high electron transfer kinetics[34] and high Li^+ site density[29] compared with the basal plane. Also, the edge plane contains functional groups and defects capable of interacting with Li^+.[35–37] Few reports studied the edge plane using electrochemistry coupled to structural imaging using SPMs such as atomic force and scanning tunneling microscopy, and spectroscopy.[29,30,38–40] These studies provided substantial insight into the intercalation process of predominant edge and basal plane electrodes and the effect of various electrolytes and additives. However, there remains limited information regarding interfacial processes from the viewpoint of ionic species, in contrast to changes in the host material. Direct inspection of ion-related phenomena, such as intercalation kinetics, and ion-coupled redox processes, is key to understanding the complexity of the battery interphase.

4.3 Materials and Methods

4.3.1 Chemicals and Materials

Lithium hexafluorophosphate ($LiPF_6$), lithium perchlorate ($LiClO_4$) and lithium tetrafluoroborate ($LiBF_4$) were all ≥99.99% purity and purchased from Sigma Aldrich as the lithium source and/or electrolyte. For additional supporting electrolyte, we used tetrabutyl ammonium

hexafluorophosphate ($TBAPF_6$ (TCI, >98%)). *N,N,N′,N′*-tetramethyl-*p*-phenylenediamine (TMPD, 99%, Sigma Aldrich) and ferrocene (Fc, 98%, Sigma Aldrich) were used as received as redox mediators for SECM imaging and positioning. All electrolyte solutions were prepared with 1:1 (by volume) mixtures of propylene carbonate (PC, anhydrous, 99.7%, Sigma Aldrich) and ethylene carbonate (EC, anhydrous, 99%, Sigma Aldrich). 2,4-dinitrophenyhydrazine (DNPH, 97%, Sigma Aldrich) was used as a Raman probe as received. Platinum ultramicroelectrodes (UME (Goodfellow, purity 99.9%, 12.5 μm radius)) for initial SECM imaging were prepared as described in previous reports.[41] All purchased chemicals were used as received without further purification.

4.3.2 HOPG Substrate Preparation

Highly oriented pyrolytic graphite (HOPG, brand grade SPI-2 from SPI supplied) and solid slabs of flexible low-density polyethylene (LDPE, 12" x 12" x 1/4" sheet from McMaster-Carr) were used for substrate preparation. The HOPG was sealed between two pieces of LDPE with a vacuum oven at 110 °C for 2 hours and cooled under ambient conditions. The HOPG edge plane was then exposed by cutting and polished to flat surface with 1-5 μm SiC sandpaper. The substrate was rinsed thoroughly with PC before SECM experiments. All Raman measurements were conducted with a 532 nm laser using a Nanophoton Laser Raman Microscope RAMAN-11.

4.3.3 HgDW Preparation

The HgDW probes were prepared as described previously.[22] In brief, Pt UMEs were prepared using standard protocols.[41] They were sharpened and polished using sandpaper (P4000) and alumina paste (1 μm), respectively. The probes were etched electrochemically in an aqueous solution of 30 v.% calcium chloride (99%, Sigma Aldrich), and 10 v.% hydrochloric acid (Macron) with an AC waveform of 2.7 V using a variable autotransformer and graphite rod as the counter electrode. Sonication was used during the etching procedure and afterward in clean HPLC-grade water to clean the probes and remove residual etching solution. Next, Hg was

electrodeposited from 5 mM mercury (II) nitrate monohydrate (≥99.99%, trace metals basis, Sigma Aldrich), and 100 mM potassium nitrate (>99%, Fisher Scientific) to refill the well. Upon filling the well, the probe was examined under an optical microscope and a glass coverslip was used to press the droplet into a flat disc. Probes were then transferred into the glovebox for SECM experiments by gradual, low pressure vacuum cycles in the antechamber to remove water and oxygen.

4.3.4 SECM Experiments

All electrochemical measurements were performed using a CHI920D Scanning Electrochemical Microscope (CH Instruments, Inc.) inside an oxygen and moisture-free glovebox. The HOPG substrates were assembled in a standard SECM cell, transferred into the glovebox and rinsed three times with fresh PC. For the first substrate, we replaced the PC with 15 mM Fc and 0.1 M $LiClO_4$ in PC:EC. We leveled the HOPG with a Pt UME and collected initial SECM images.

Thereafter, we ran multiple LSV scan from 3.3 to 0.5 V *vs*. Li^+/Li. We used a Pt wire as the counter electrode and a polished Ag wire as a quasi-reference. All potentials were converted to the Li^+/Li scale using standard potential of the redox mediator (Fc or TMPD) and of Li^+ amalgamation-stripping. After several scans, we reapproached the HOPG with the Pt UME and reimaged the same region. For the second substrate used in the intercalation experiments, we replaced the PC with 10 mM TMPD, 10 mM $LiPF_6$, 100 mM $TBAPF_6$ in PC:EC. We leveled and imaged the substrate using the same protocol as the first sample. Thereafter we replaced the Pt UME with a HgDW (12.5 μm radius), approached again to the surface and positioned the probe above the center of the HOPG substrate. We approached to the surface, retracted and rinsed the cell three times with fresh PC. We refilled the cell with 10 mM $LiPF_6$ and 100 mM $TBAPF_6$ and repositioned the probe close to the HOPG substrate. We continually cycled the probe with cyclic voltammetry to quantify Li^+ in the vicinity of the probe. While collecting information at the probe,

we applied potential steps to the substrate (~16 s each) in 100 mV increments between 3.0 and 0.6 V vs Li^+/Li. After six cycles we stepped the substrate further negative and decreased the step size to 50 mV.

4.3.5 DNPH Modification of the HOPG Surface

Following previous protocols,[42,43] we prepared a 10 mM DNPH solution in ethanol (with 1% HCl). We degassed the solution and brought it to a boil while stirring. Next, we submerged a fresh HOPG substrate, turned off heat and continued degassing and stirring for 2 hours while the reaction proceeded. We removed the substrate, rinsed thoroughly with ethanol and submerged it into a solution of 0.1 M KOH in ethanol for 10 minutes. Finally, we rinsed again with ethanol, allowed the sample to dry and conducted Raman spectroscopy under ambient conditions.

4.3.6 COMSOL Simulations

Simulations were completed using the Transport of Diluted Species module within COMSOL Multiphysics 4.4, using Fick's laws for diffusion. For simulation of the intercalation process, we used a 2D axisymmetric geometry representing a radial cross section of the HgDW probe positioned near the HOPG electrode. Three active domains were defined: 1) Amalgam, 2) HOPG, and 3) Solution. All parameters used in the simulations are listed in Table 4.1 with reference values. The Amalgam domain and its Flux boundary with the Solution domain involved consumption of species (M+) at the Flux boundary to produce reduced species (M(Hg)) that could diffuse freely into the Amalgam domain. Likewise, the HOPG domain was defined the same way as the Amalgam domain but with its own parameters and Flux boundary defined by Butler-Volmer. The potential at the Amalgam domain Flux boundary was controlled based on a sweeping potential to simulate cyclic voltammetry at the probe. For each simulation the potential applied to the HOPG domain Flux boundary, subE, was maintained at a constant value. Open boundaries were set to bulk conditions. Most values collected from the literature agreed with our simulations.

We note the largest discrepancies involve those surrounding the HgDW (e.g. k^0, D_{red}, $\alpha_{Hg\text{-}Li}$). HgDW probes are sensitive to the electrolyte environment, and contaminants, especially at the Hg surface, can affect the overall probe response. However, even non-ideal probes can be quite stable throughout measurements. We used the parameters that fit best for multiple curves and considered the substrate response for interpretation. Further details provided in Appendix B.

4.4 Results

We immersed an HOPG edge plane (Fig. 4.2a) in a mixed propylene carbonate and ethylene carbonate (PC:EC (1:1 ratio by volume)) electrolyte containing 100 mM lithium perchlorate ($LiClO_4$) and 15 mM ferrocene (Fc) as a redox mediator to probe the local electron transfer kinetics with imaging (Fig. 4.2b and 4.2c). Once the probe was approached to the surface, we observed characteristic mass transfer limited positive feedback (increased redox response) on the SECM probe when transiting above the conductive HOPG (Fig. 4.2c). In contrast, the insulating LDPE showed a characteristic negative feedback (decreased current, Fig. 4.2c). This provided clear identification of the edge location for further positioning in other experiments. We used linear sweep voltammetry (LSV) to form the SEI (Fig. 4.2d). Previous reports indicated that SEI formation on carbon occurs on a wide potential window preceding bulk intercalation, which begins at potentials <0.3 V.[23,44–46] Hereon, we identify these two electrode potential regions as the SEI and intercalation regions.[23]

We first focus on the SEI region. In the first sweep, a cathodic wave peaked near 1.1 V in the HOPG response (Fig. 4.2d). Upon further sweeps, this cathodic wave diminished suggesting a passivation process.[23,29] SECM imaging also indicated significant passivation, as evidenced by a decreasing feedback current; however significant heterogeneity was also observed, suggesting differences in the local electron transfer kinetics (Fig. 4.2e). We observed similar features and an increase in roughness with SEM after SEI and intercalation experiments (Fig. 4.3). All results

suggested SEI formation at the HOPG edge, alike to that observed on other graphitic samples.[7,23,47]

To analyze changes in Li^+ flux during the SEI formation process, we focused on an electrolyte containing 10mM lithium hexafluorophosphate ($LiPF_6$) as the Li^+ source and 100 mM tetrabutyl ammonium hexafluorophosphate ($TBAPF_6$) supporting electrolyte. Batteries commonly involve at least 1 M Li^+ concentrations to maintain high conductivity and accommodate loss of Li^+ during SEI formation and cycling. However, these conditions are not strict limitations for SEI formation and Li^+ intercalation.[23,48] Following detection of the edge-plane using SECM feedback, we rinsed the cell from the redox mediator and switched to a mercury disc-well (HgDW, Fig. 4.4) for measuring the Li^+ response.[22] This was accomplished by continuous cycling of the probe at 1 V/s under conditions of stripping voltammetry, thus detecting local depletion and enrichment[49,50] of ions upon activation of the HOPG substrate, as depicted in Fig. 4.5a and 4.5b. We monitored changes in the stripping peak current (i_{sp}, Fig. 4.5a) as a direct indicator of the local Li^+ concentration resulting from the ion flux to the electrode.[20,21,23] Inward and outward fluxes were detected by i_{sp}, with Li^+ consumption by the HOPG electrode decreasing the absolute value of i_{sp}, and vice versa.

Focusing on the SEI formation region (Fig. 4.5c),[23] we decreased the potential of the HOPG electrode in 100 mV increments from 3.0 V to 0.6 V vs. Li^+/Li in a similar fashion to the potentiometric intermittent titration technique, or PITT.[51,52] To better compare the probe and substrate responses over the step interval, we integrated the current passed by the substrate during each increment (Fig. 4.5b, bottom) to yield an HOPG charge (Fig. 4.5c). During the forward sweep, and especially when stepping more negative than 1.3 V, we observed a concurrent cathodic process on the HOPG and a decrease in i_{sp} (Fig. 4.5c). This potential range agrees with previous reports for irreversible SEI formation on graphitic and edge plane electrodes.[10,29,53] The decrease in i_{sp} follows the trend of the HOPG response indicating that Li^+ is being consumed by

HOPG as part of the electrochemical reaction during the cathodic sweep. Interestingly, stepping the HOPG again positive reversed this trend, revealing an anodic process at 1.4 V and the concurrent increase in i_{sp} implying a reversible process involving an outward flux of Li^+.

The edge plane has a high density of Li^+ sites[29] and can be a site of disorder[54] and functional groups.[37] Previous reports on HOPG suggested Li^+ insertion as part of the SEI formation mechanism;[29,46,53] on the other hand, Li^+ intercalation occurs at more negative potentials, below 0.3 V.[29,55] A reversible SEI film was reported on HOPG as long as potentials were kept positive of 1 V vs. Li^+/Li.[6] Further, redox-active organic groups involving carbonyl species at the edge plane can cause a flux of Li^+; in this case, Li^+ uptake into the SEI would result from reduction of charge neutral C–O groups to the negatively charged species, thus binding to the positively charged alkali.[37,56,57] Following the method proposed in the works of McCreery,[42,43] we used 2,4- dinitrophenylhydrazine (DNPH) as a Raman-active molecular tag for carbonyl functionality at the electrode surface. This experiment indeed showed the presence of surface carbonyl groups on the original samples; by comparing the peak areas for graphite and DNPH Raman peaks and assuming a flat surface, we estimate >90% coverage by carbonyl groups at the HOPG edge (Fig. 4.6a). Evaluation of the anodic charge passed upon voltammetric scan reversal (Fig. 4.6b) indicated a charge density of 110 mC cm^{-2} for the reversible species, suggesting the formation of a multi-layer of redox-active material. We speculate that the observed flux at this potential region results from reversible Li^+ insertion and deinsertion during redox of this SEI, as Li^+ release was dependent on the history of the sweep, i.e. only observed after a reduction process had taken place and at sufficiently positive HOPG potentials (>1.4 V vs. Li^+/Li). Another possibility is that the formation of a dynamic SEI, e.g. dissolving after formation, could lead to the observed Li^+ release.[6] Regardless of the origin, these results suggest a direct observation of the reversible nature of an SEI on the graphitic edge plane.

We noted a significant capacity loss (60%) during the first cycle between the forward/reverse sweeps (Fig. 4.5c) suggesting simultaneous reversible and irreversible components to the total process. Both the cathodic and anodic processes occurring at HOPG decreased upon further cycling evidencing the transient formation of the SEI. These changes in behavior were mirrored on the probe response (Fig. 4.5d), which showed a smaller change in i_{sp} with cycle number at a fixed potential window (e.g. cycle 1–6). Polarizing further negative had the effect of consuming these SEI formation processes and gave way to new ones.

Next, we focus on the intercalation region (Fig. 4.5d). After a brief transient where the HOPG and HgDW responses revealed further SEI formation (Fig. 4.5d, cycle 7), we observed the onset of a second cathodic process (<0.3 V). Stepping the HOPG potential further negative (Fig. 4.5d, cycles 8 and 9) revealed a cathodic plateau (<0.3 V) paired with an anodic peak (0.4 V) on the return. This behavior is consistent with Li^+ uptake during intercalation, and a release, enriching Li^+ local concentration, during deintercalation. We note also that the potential region for this second process agrees with (de)intercalation at bulk graphite.[44,58] Also, the reversible SEI process (>0.6 V) quickly diminished upon sweeping further negative, leaving behind only a slightly decreased signal on the idle i_{sp} background, e.g. compare the origin of cycles 1 and 9 on Fig. 4.5d. This transition has rarely been discussed,[6] though HOPG and its edge plane undergo substantial structural changes during SEI formation and cycling.[59] We also observed a similar transition with a high Li^+ concentration. Despite the fundamental differences between processes such as intercalation and SEI formation, our SECM approach is capable of detecting the resulting ion responses as the substrate is activated.

We now turn to quantifying the local intercalation kinetics aided by the measurement of i_{sp}. By using COMSOL Multiphysics finite element method, we simulated the probe response in a 2D axisymmetric geometry (Fig. 4.7a) during the intercalation sweep, assuming reported intercalation parameters on other graphitic materials as initial conditions (Appendix B). We

modified our previous model[22] with an HOPG domain (Fig. 4.7a) that consumed Li^+ based on a defined forward rate constant, k_{fLi}, which caused a response on the simulated SECM tip voltammetry (Fig. 4.7b). k_{fLi} can be further understood in the context of Butler–Volmer kinetics (B–V), as is done in Fig. 4.7c, but it does not assume this model in the calculation of the values presented in Table 1. Therefore, these values can be used to understand fundamental activation aspects in more complex derivations of the graphitic system.[60]

By fitting the overall response, we determined a k_{0Li} of 10^{-4} cm s^{-1} for the HOPG substrate. Our results in Fig. 4.7c are significantly faster than reported rates for (de)intercalation at bulk graphite (10^{-7} cm s^{-1}),[44] and agree more with electron transfer kinetics.[31,61] Both electron transfer kinetics and the fraction of edge-to-basal plane are known to affect intercalation kinetics.[31] Due to the low potentials accessed, plating may also have occurred aside intercalation. However, the HOPG response does not indicate plating or the familiar "cross-over" due to nucleation[62] until stepping 150 mV further negative during cycle 9 (Fig. 4.8). Aside, our best fit was for low α (Fig. 4.7c), suggesting our SEI or the edge itself have a pinhole-like structure and small kinetic domains.[61,63] Accurate modeling of deintercalation kinetics would require detailed knowledge of bulk transport and state of charge at the HOPG electrode, however the change in i_{sp} observed for this process suggests faster rates than for intercalation, consistent with previous reports.[64–66] Kinetics related to the SEI formation process and intercalation are key parameters for battery performance and limitations.[60,67] Our methods move away from bulk characterization of kinetics to measurements at a single location addressed by a versatile probe.

4.5 Conclusions

In conclusion, our SECM approach was capable of correlating Li^+ flux as the HOPG interface was activated toward both irreversible SEI formation and (de)intercalation. The highly reactive HOPG edge plane shows potential regime-dependent behavior. Cycling in a high potential region (>0.6 V) led to SEI formation, but also a rarely reported redox reaction involving

reversible exchange of Li^+.[37] Upon stepping the HOPG further negative, we observed a transition to (de)intercalation. The HgDW response agreed with bulk measurements and captured local screenshots of Li^+ uptake and release by the substrate. By developing a COMSOL model of the intercalation process, we determined localized, fundamental kinetic information. Our strategy paves the way toward *in situ*, kinetic mapping of ionic processes,[22] smaller probes and higher resolution,[68] and amenable chemical resolution for emerging next-generation ion batteries.[69–73]

4.6 Acknowledgments

The authors gratefully acknowledge financial support from the National Science Foundation under grant NSF CHE 1709391. Z. T. G. acknowledges the ACS Division of Analytical Chemistry Summer Fellowship and the Hinoree T. and Mrs Kimiyo Enta Fellowship for support. Y. Z. acknowledges the China Scholarship Council for support under grant CSC201706130031. The authors thank Dr Zachary J. Barton for training in Hg probe preparation and application.

4.7 Figures and Table

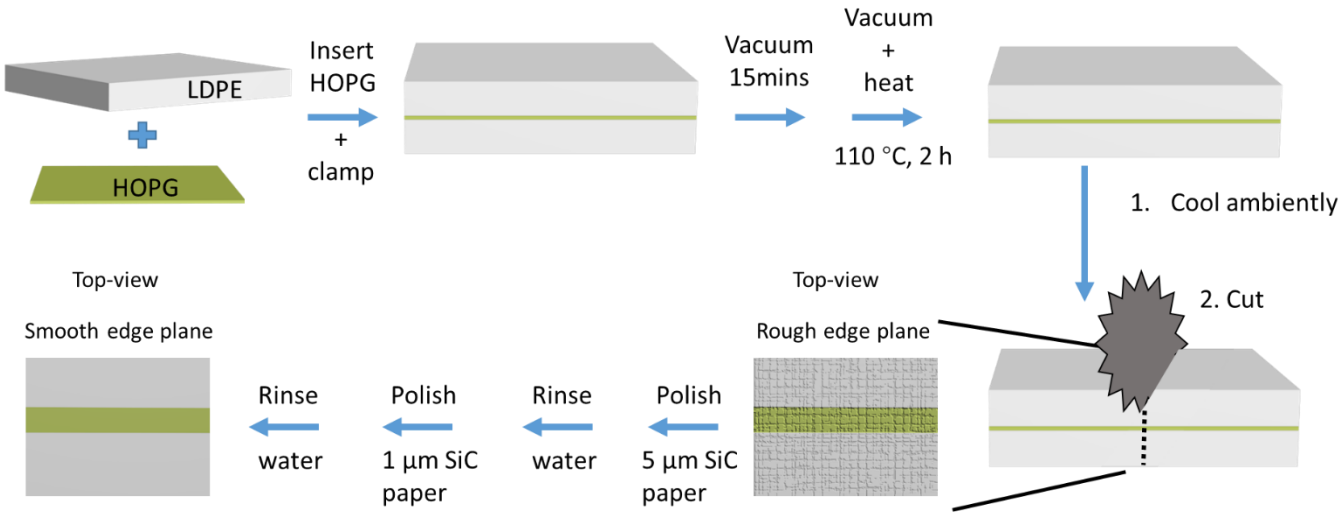

Figure 4.1. HOPG edge plane fabrication procedure.

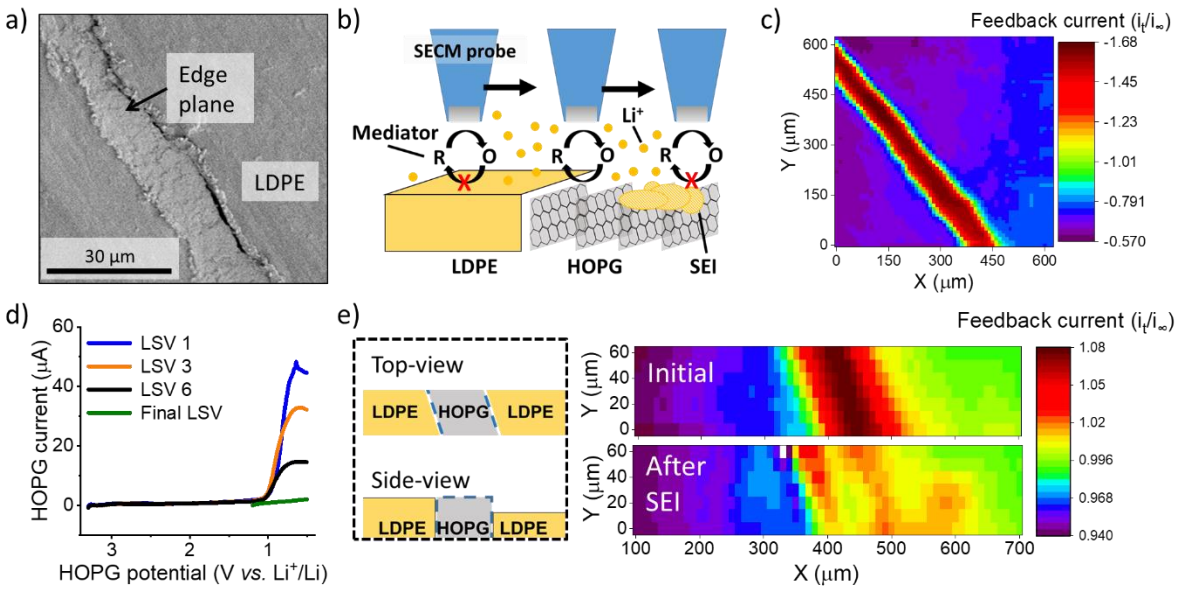

Figure 4.2. SEI formation on the HOPG edge plane. (a) Scanning electron microscopy of an unused region of HOPG edge. (b) Illustration of experimental setup and procedure for SECM imaging and positioning. (c) SECM feedback image of the HOPG substrate. (d) Multiple LSV sweeps on HOPG in the SEI region. (e) SECM images before and after SEI formation. A diagram of the sample (on left) represent the HOPG sample geometry; explaining the tilt observed in the SECM images. SECM and LSV were collected in 0.1 M $LiClO_4$, PC : EC (1 : 1) with 15 mM Fc. For the SECM images, the measured current, it, was normalized by the limiting current far from the substrate, i_∞.

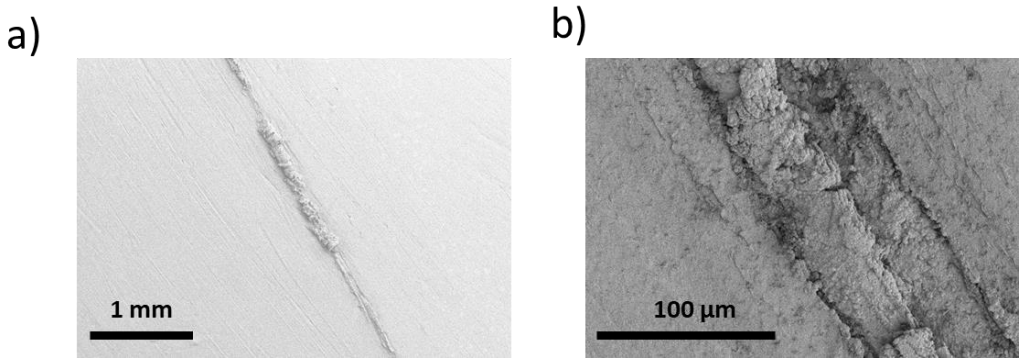

Figure 4.3. SEM characterization of used regions on HOPG edge samples after intercalation experiments. a) and b) show used regions with large protrusions, cracking and holes.

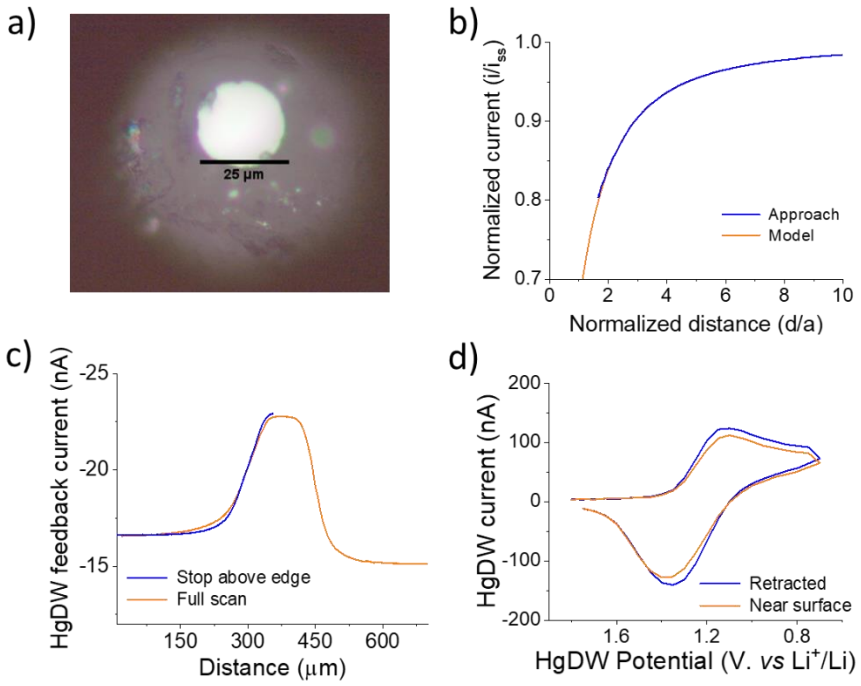

Figure 4.4. HgDW probe and positioning for SEI and intercalation measurements. a) Optical microscopy of HgDW after pressing. b) Approach curve to the LDPE portion of the substrate. c) Positioning the HgDW above the HOPG edge using linescans in the X direction. d) Probe response near the surface and retracted ~ 60 µm.

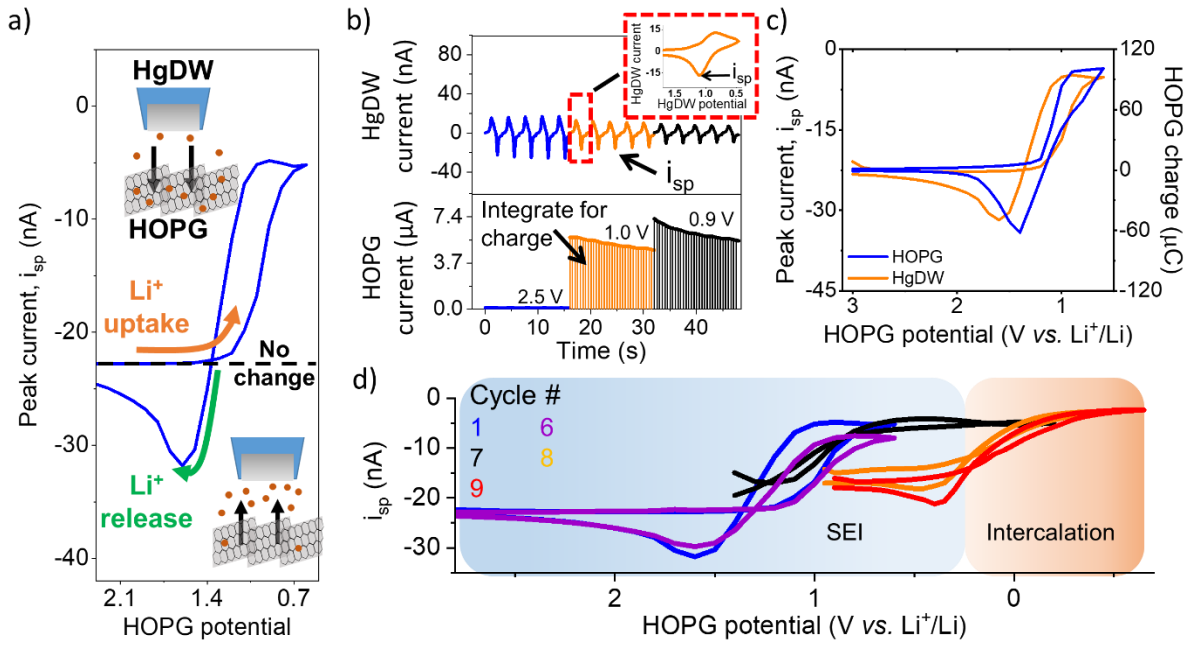

Figure 4.5. Li^+ flux at HOPG during SEI formation. (a) Illustration of processed measurements. (b) Process for collecting the data by cycling the HgDW at 1 V s^{-1} (top) while controlling the HOPG potential (bottom). The inset shows a single HgDW cycle with current vs. HgDW potential. The charge for each transient at HOPG was determined through integration at each potential. (c) Comparison of extracted peak currents, isp, from the HgDW and the integrated HOPG response for each potential during the 1st SEI formation cycle. (d) Measured isp during cycling in the SEI and Intercalation regions. Cycles 1 and 6 are normalized based on the linear region >1.5 V.

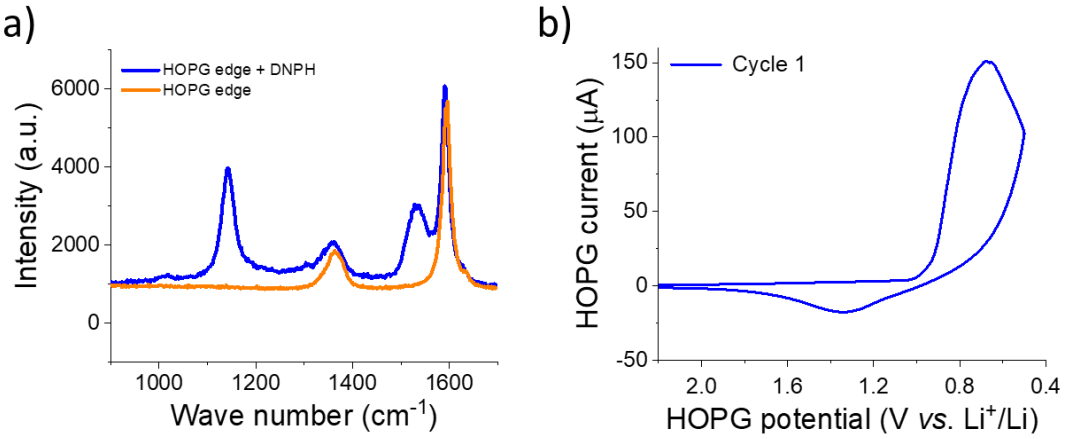

Figure 4.6. Reversible surface species during SEI formation. a) Raman spectrum of HOPG edge plane samples with and without reaction with DNPH. b) First SEI formation cycle on an HOPG edge plan sample.

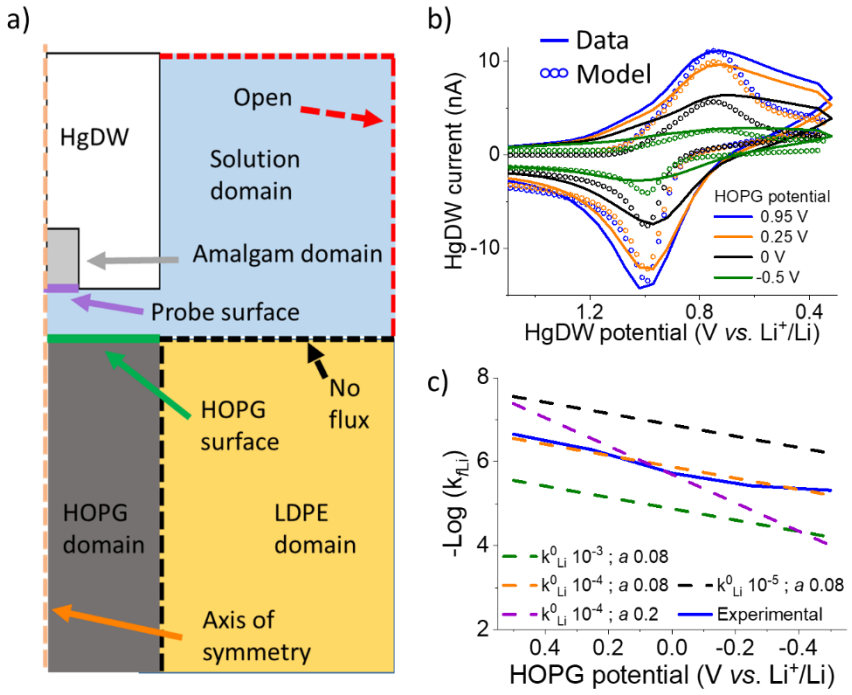

Figure 4.7. COMSOL modeling of intercalation kinetics. (a) Diagram of the COMSOL model for determining k_{fLi}.(b) Fitting of probe response with a COMSOL model for the intercalation in cycle 8. (c) Total data set for the cycle 8 and extracted k_{fLi} fit to different k^0_{Li} and a based on B–V.

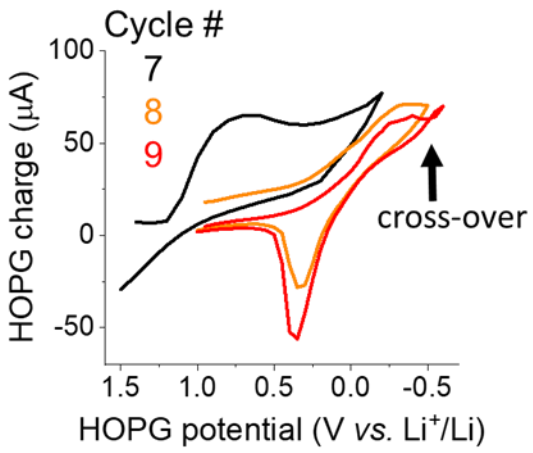

Figure 4.8. Measured HOPG charge during cycling in the Intercalation region. Cross-over indicating plating and nucleation occurred in cycle 9.

Table 4.1. Extracted k_{fLi} from COMSOL fittings.

HOPG potential (V *vs*. Li^+/Li)	k_{fLi} (cm s^{-1})
0.5	2.8×10^{-5}
0.25	6.1×10^{-5}
0	1.3×10^{-4}
-0.25	2.9×10^{-4}
-0.5	6.3×10^{-4}

4.8 References

(1) A. M. Tripathi, W.-N. Su and B. J. Hwang, *Chem. Soc. Rev.*, **2018**, 47, 736–851.

(2) J. Hui, Z. T. Gossage, D. Sarbapalli, K. Hernandez-Burgos and J. Rodríguez-López, *Anal. Chem.*, **2018**, 91, 60–83.

(3) G. Crabtree, G. Rubloff and E. Takeuchi, *Basic research needs for next generation electrical energy storage, Report of the Office of Basic Energy Sciences Workshop on Energy Storage*, U.S. Department of Energy Office of Science, Washington, D.C., **2017**.

(4) H.-Y. Song and S.-K. Jeong, *J. Power Sources*, **2018**, 373, 110–118.

(5) D. Lu, J. Tao, P. Yan, W. A. Henderson, Q. Li, Y. Shao, M. L. Helm, O. Borodin, G. L. Graff and B. Polzin, *Nano Lett.*, **2017**, 17, 1602–1609.

(6) L. Seidl, S. Martens, J. Ma, U. Stimming and O. Schneider, *Nanoscale*, **2016**, 8, 14004–14014.

(7) H. Bülter, P. Schwager, D. Fenske and G. Wittstock, *Electrochim. Acta*, **2016**, 199, 366–379.

(8) J. Z. Olson, P. K. Johansson, D. G. Castner and C. W. Schlenker, *Chem. Mater.*, **2018**, 30, 1239–1248.

(9) F. Shi, P. N. Ross, G. A. Somorjai and K. Komvopoulos, *J. Phys. Chem. C*, **2017**, 121, 14476–14483.

(10) A. v. Cresce, S. M. Russell, D. R. Baker, K. J. Gaskell and K. Xu, *Nano Lett.*, **2014**, 14, 1405–1412.

(11) M. Steinhauer, M. Stich, M. Kurniawan, B.-K. Seidlhofer, M. Trapp, A. Bund, N. Wagner and K. A. Friedrich, *ACS Appl. Mater. Interfaces*, **2017**, 9, 35794–35801.

(12) J. L. L. Lopez, P. J. Grandinetti and A. C. Co, *J. Mater. Chem. A*, **2018**, 6, 231–243.

(13) L. Nowack, D. Grolimund, V. Samson, F. Marone and V. Wood, *Sci. Rep.*, **2016**, 6, 21479.

(14) K. Zhang, F. Ren, X. Wang, E. Hu, Y. Xu, X.-Q. Yang, H. Li, L. Chen, P. Pianetta and A. Mehta, *Nano Lett.*, **2017**, 17, 7782–7788.

(15) T. Yamanaka, H. Nakagawa, S. Tsubouchi, Y. Domi, T. Doi, T. Abe and Z. Ogumi, *ChemSusChem*, **2017**, 10, 855–861.

(16) M. E. Snowden, M. Dayeh, N. A. Payne, S. Gervais, J. Mauzeroll and S. B. Schougaard, *J. Power Sources*, **2016**, 325, 682–689.

(17) L. Danis, S. M. Gateman, C. Kuss, S. B. Schougaard and J. Mauzeroll, *ChemElectroChem*, **2017**, 4, 6–19.

(18) S.-H. Yu, X. Huang, K. Schwarz, R. Huang, T. A. Arias, J. D. Brock and H. D. Abruña, *Energy Environ. Sci.*, **2018**, 11, 202–210.

(19) J. Wang, Y.-c. K. Chen-Wiegart, C. Eng, Q. Shen and J. Wang, *Nat. Commun.*, **2016**, 7, 12372.

(20) Z. J. Barton and J. Rodríguez-López, *Anal. Chem.*, **2014**, 86, 10660–10667.

(21) Z. J. Barton, J. Hui, N. B. Schorr and J. Rodríguez-López, *Electrochim. Acta*, **2017**, 241, 98–105.

(22) Z. J. Barton and J. Rodríguez-López, *Anal. Chem.*, **2017**, 89, 2716–2723.

(23) J. Hui, M. Burgess, J. Zhang and J. Rodríguez-López, *ACS Nano*, **2016**, 10, 4248–4257.

(24) Z. J. Barton and J. Rodríguez-López, *Anal. Bioanal. Chem.*, **2016**, 408, 2707–2715.

(25) N. Balke, S. Jesse, Y. Kim, L. Adamczyk, A. Tselev, I. N. Ivanov, N. J. Dudney and S. V. Kalinin, *Nano Lett.*, **2010**, 10, 3420–3425.

(26) Y. Takahashi, A. Kumatani, H. Munakata, H. Inomata, K. Ito, K. Ino, H. Shiku, P. R. Unwin, Y. E. Korchev and K. Kanamura, *Nat. Commun.*, **2014**, 5, 5450.

(27) E. Ventosa and W. Schuhmann, *Phys. Chem. Chem. Phys.*, **2015**, 17, 28441–28450.

(28) R. L. McCreery, K. K. Cline, C. A. McDermott and M. T. McDermott, *Colloids Surf. A*, **1994**, 93, 211–219.

(29) Y. Domi, M. Ochida, S. Tsubouchi, H. Nakagawa, T. Yamanaka, T. Doi, T. Abe and Z. Ogumi, *J. Phys. Chem. C*, **2011**, 115, 25484–25489.

(30) S. Tsubouchi, Y. Domi, T. Doi, M. Ochida, H. Nakagawa, T. Yamanaka, T. Abe and Z. Ogumi, *J. Electrochem. Soc.*, **2012**, 159, A1786–A1790.

(31) Y. Yamada, K. Miyazaki and T. Abe, *Langmuir*, **2010**, 26, 14990–14994.

(32) K. Persson, V. A. Sethuraman, L. J. Hardwick, Y. Hinuma, Y. S. Meng, A. Van Der Ven, V. Srinivasan, R. Kostecki and G. Ceder, *J. Phys. Chem. Lett.*, **2010**, 1, 1176–1180.

(33) M. Winter, P. Nov´ak and A. Monnier, *J. Electrochem. Soc.*, **1998**, 145, 428–436.

(34) R. J. Rice and R. L. McCreery, *Anal. Chem.*, **1989**, 61, 1637–1641.

(35) J. Collins, G. Gourdin, M. Foster and D. Qu, *Carbon*, **2015**, 92, 193–244.

(36) T. Placke, V. Siozios, R. Schmitz, S. F. Lux, P. Bieker, C. Colle, H. W. Meyer, S. Passerini and M. Winter, *J. Power Sources*, **2012**, 200, 83–91.

(37) N. Ogihara, Y. Igarashi, A. Kamakura, K. Naoi, Y. Kusachi and K. Utsugi, *Electrochim. Acta*, **2006**, 52, 1713–1720.

(38) Y. Domi, M. Ochida, S. Tsubouchi, H. Nakagawa, T. Yamanaka, T. Doi, T. Abe and Z. Ogumi, *J. Electrochem. Soc.*, **2012**, 159, A1292–A1297.

(39) Y. Domi, T. Doi, M. Ochida, T. Yamanaka, T. Abe and Z. Ogumi, *J. Electrochem. Soc.*, **2016**, 163, A2849–A2853.

(40) H. Nakagawa, Y. Domi, T. Doi, M. Ochida, S. Tsubouchi, T. Yamanaka, T. Abe and Z. Ogumi, *J. Power Sources*, **2012**, 206, 320–324.

(41) Bard, A. J.; Fan, F. R. F.; Kwak, J.; Lev, O. *Anal. Chem.* **1989,** *61* (2), 132-138.

(42) M. A. Fryling, J. Zhao and R. L. McCreery, *Anal. Chem*., **1995**, 67, 967–975.

(43) K. Ray and R. L. McCreery, *Anal. Chem.*, **1997**, 69, 4680–4687.

(44) M. D. Levi and D. Aurbach, *J. Electroanal. Chem*., **1997**, 421, 79–88.

(45) Z. Ogumi and M. Inaba, *Bull. Chem. Soc. Jpn*., **1998**, 71, 521–534.

(46) S. Flandrois and B. Simon, *Carbon*, **1999**, 37, 165–180.

(47) H. Bülter, F. Peters, J. Schwenzel and G. Wittstock, *Angew. Chem., Int. Ed*., **2014**, 53, 10531–10535.

(48) D. Rehnlund, C. Ihrfors, J. Maibach and L. Nyholm, *Mater. Today*, **2018**, 21, 1010–1018.

(49) M. L. A. V. Heien, M. A. Johnson and R. M. Wightman, *Anal. Chem*., **2004**, 76, 5697–5704.

(50) N. T. Rodeberg, S. G. Sandberg, J. A. Johnson, P. E. M. Phillips and R. M. Wightman, *ACS Chem. Neurosci*., **2017**, 8, 221–234.

(51) M. D. Levi, E. A. Levi and D. Aurbach, *J. Electroanal. Chem*., **1997**, 421, 89–97.

(52) J. Li, X. Xiao, F. Yang, M. W. Verbrugge and Y.-T. Cheng, *J. Phys. Chem. C*, **2011**, 116, 1472–1478.

(53) M. Inaba, Z. Siroma, Y. Kawatate, A. Funabiki and Z. Ogumi, *J. Power Sources*, **1997**, 68, 221–226.

(54) G. Katagiri, H. Ishida and A. Ishitani, *Carbon*, **1988**, 26, 565–571.

(55) Y. NuLi, J. Yang and Z. Jiang, *J. Phys. Chem. Solids*, **2006**, 67, 882–886.

(56) K. Hernández-Burgos, G. G. Rodríguez-Calero, W. Zhou, S. E. Burkhardt and H. D. Abruña, *J. Am. Chem. Soc*., **2013**, 135, 14532–14535.

(57) M. Burgess, K. Hernández-Burgos, K. J. Cheng, J. S. Moore and J. Rodríguez-López, *Analyst*, **2016**, 141, 3842–3850.

(58) D. Aurbach, M. D. Levi, E. Levi and A. Schechter, *J. Phys. Chem. B*, **1997**, 101, 2195–2206.

(59) Y. Domi, T. Doi, H. Nakagawa, T. Yamanaka, T. Abe and Z. Ogumi, *J. Electrochem. Soc*., **2016**, 163, A2435–A2440.

(60) R. B. Smith, E. Khoo and M. Z. Bazant, *J. Phys. Chem. C*, **2017**, 121, 12505–12523.

(61) N. L. Ritzert, J. Rodríguez-López, C. Tan and H. c. D. Abruña, *Langmuir*, **2013**, 29, 1683–1694.

(62) S. H. White and U. M. Twardoch, *J. Appl. Electrochem*., **1987**, 17, 225–242.

(63) A. Kiani, M. A. Alpuche-Aviles, P. K. Eggers, M. Jones, J. J. Gooding, M. N. Paddon-Row and A. J. Bard, *Langmuir*, **2008**, 24, 2841–2849.

(64) Q. Liu, C. Du, B. Shen, P. Zuo, X. Cheng, Y. Ma, G. Yin and Y. Gao, *RSC Adv*., **2016**, 6, 88683–88700.

(65) Y. Yamada, M. Yaegashi, T. Abe and A. Yamada, *Chem. Commun*., **2013**, 49, 11194–11196.

(66) S. R. Sivakkumar, J. Y. Nerkar and A. G. Pandolfo, *Electrochim. Acta*, **2010**, 55, 3330–3335.

(67) P. M. Attia, S. Das, S. J. Harris, M. Z. Bazant and W. C. Chueh, *J. Electrochem. Soc*., **2019**, 166, E97–E106.

(68) C. G. Zoski, *Curr. Opin. Electrochem*., **2017**, 1, 46–52.

(69) H. Sun, L. Mei, J. Liang, Z. Zhao, C. Lee, H. Fei, M. Ding, J. Lau, M. Li and C. Wang, *Science*, **2017**, 356, 599–604.

(70) B. Ji, F. Zhang, X. Song and Y. Tang, *Adv. Mater*., **2017**, 29, 1700519.

(71) J.-Y. Hwang, S.-T. Myung and Y.-K. Sun, *Chem. Soc. Rev.*, **2017**, 46, 3529–3614.

(72) H.-S. Kim, J. B. Cook, H. Lin, J. S. Ko, S. H. Tolbert, V. Ozolins and B. Dunn, *Nat. Mater*., **2017**, 16, 454.

(73) J. W. Choi and D. Aurbach, *Nat. Rev. Mater*., **2016**, 1, 16013.

CHAPTER 5

Coordinated Mapping of Li^+ Flux and Electron Transfer Reactivity during Solid-Electrolyte Interphase Formation at a Graphene Electrode

5.1 Abstract

Interphases formed at battery electrodes are key to enabling energy dense charge storage by acting as protection layers and gatekeeping ion flux into and out of the electrodes. However, our current understanding of these structures and how to control their properties is still limited due to their heterogenous structure, dynamic nature, and lack of analytical techniques to probe their electronic and ionic properties in situ. In this study, we used a multi-functional scanning electrochemical microscopy (SECM) technique based on an amperometric ion-selective mercury disc-well (HgDW) probe for spatially resolving changes in interfacial Li^+ during solid electrolyte interphase (SEI) formation and for tracking its relationship to the electronic passivation of the interphase. We focused on multi-layer graphene (MLG) as a model graphitic system and developed a method for ion-flux mapping based on pulsing the substrate at multiple potentials with distinct behavior (e.g. insertion–deinsertion). By using a pulsed protocol, we captured the localized uptake of Li^+ at the forming SEI and during intercalation, creating activity maps along the edge of the MLG electrode. On the other hand, a redox probe showed passivation by the interphase at the same locations, thus enabling correlations between ion and electron transfer. Our analytical method provided direct insight into the interphase formation process and could be used for evaluating dynamic interfacial phenomena and improving future energy storage technologies.

This chapter is adapted and reprinted from an original research article in *Analyst** with permission from the Royal Society of Chemistry, copyright 2020. Z.T.G. conducted the experiments, made the figures and wrote the publication. J.H. and D.S. helped with writing and substrate preparation.

*Gossage, Z.T.; Hui, J.; Sarbapalli, D.; and Rodríguez-López, J. "Coordinated Mapping of Li^+ Flux and Electron Transfer Reactivity during Solid-Electrolyte Interphase Formation at a Graphene Electrode." *Analyst*, **2020**, 145, 2631-2638. DOI: 10.1039/C9AN02637A

5.2 Introduction

Elucidating the evolution of battery interphases during operation is a major research priority for improving energy storage technologies.[1–7] Achieving high energy densities, as in lithium ion batteries (LIB) and many next generation technologies, requires redox reactions at very high and low potentials.[1,4,8] Consequently, these potentials lead to electrolyte decomposition, forming interphases at the electrodes that regulate electrode reactivity upon further cycling.[1,4] At negative electrodes, such as a graphitic carbon or Si, the formed interphase is referred to as the solid-electrolyte interphase (SEI) and forms rapidly during the initial cycles.[1,4] Recent reports using operando and in situ characterization techniques indicated the SEI structure is morphologically and chemically heterogeneous and continues fluctuating during extended cycling or at open circuit potentials (OCP).[1,9–14] These characterization techniques have led to improved understanding of the SEI components and precursors, but few works have focused on acquiring information regarding interfacial alkali ion (e.g. Li^+) dynamics during SEI initiation and stabilization in spite of the key role of Li+ in the energy storage mechanism.[15–17]

Emerging scanning probe methods (SPMs), such as scanning electrochemical microscopy (SECM),[15,16,18–20] scanning ion-conductance microscopy (SICM),[21–23] or scanning electrochemical cell microscopy (SECCM),[24,25] show promise for tracking and understanding interfacial ion dynamics at functional electrodes.[2,26,27] Recently, our lab introduced Hg probes and methods combined with SECM to provide localized insight of ion flux within real battery environments.[18,28] Our group applied these probes to measure ion intercalation[16,19] and kinetics[15] on graphitic carbons. Also, these probes can utilize the ions to resolve topographical features for both imaging and positioning.[28–30] In few studies, Hg probes were successful at capturing ionic flux images at reacting surfaces.[18,19,31] Ionic imaging is a powerful tool for evaluating battery materials and their interphases, providing access to wide temporal and spatial information.[28]

Hg probes are easy to prepare and provide the unique opportunity to quantify both ionic and electronic information at the same location.[28] As with other SECM studies, adding a dilute redox mediator to the electrolyte enables evaluation of electron transfer across the passivating SEI.[14,32,33] Thereafter, the Hg probe can reversibly switch between feedback or ionic imaging modes through either redox reactions with a mediator or amalgamation/stripping, respectively.[28] This multi-functional probe would help understand how electron and ion transfer reactivity are related, with the ultimate goal of improving interphase stability and function.[2,34]

In this work, we take advantage of the multimodal nature of the Hg probe for extracting and comparing electron and ion transfer at operating multi-layer graphene (MLG) electrodes. We chose MLG as a model graphitic electrode because previous studies on MLG showed fast rate capabilities for (de)intercalation and extensive SEI formation.[19,35,36] Using mercury disc-well (HgDW) microelectrodes,[28] we tracked Li^+ dynamics at different locations during SEI formation and (de)intercalation processes. With the redox mediator couple, *N*,*N*,*N'*,*N'*-tetramethyl-*p*-phenylenediamine (TMPD/$TMPD^+$), we positioned the probe near the thin MLG surface and coordinated Li^+ flux measurements with the MLG potential and electron transfer across its surface throughout the experiments. We introduced a pulsed mapping procedure based on cyclic voltammetry SECM (CV-SECM)[19,28,29] to minimize bulk substrate effects and more effectively measure localized Li^+ flux. We discuss the impact of the extended electrode surface on Li^+ flux maps and the invaluable insight that is accessible through our approach and for future in situ studies.

5.3 Materials and Methods

5.3.1 Chemicals and Materials

For the Li^+ source, we used lithium hexafluorophosphate ($LiPF_6$, ≥99.99%) and lithium tetrafluoroborate ($LiBF_4$, ≥99.99%) from Sigma Aldrich. Also, tetrabutyl ammonium

hexafluorophosphate ($TBAPF_6$ (Sigma Aldrich, 99%)) acted as an additional supporting electrolyte. *N*,*N*,*N'*,*N'*-tetramethyl-*p*-phenylenediamine (TMPD, 99%, Sigma Aldrich) was used as the redox mediator. All electrolyte solutions were prepared in 1:1 (by volume) propylene carbonate (PC, anhydrous, 99.7%, Sigma Aldrich) and ethylene carbonate (EC, anhydrous, 99%, Sigma Aldrich). Platinum ultramicroelectrodes (Goodfellow, purity 99.9%, 12.5 μm radius) were prepared as described previously.[28,37] All purchased chemicals were used as received without further purification.

5.3.2 Substrate Preparation and Characterization

Multilayer graphene samples were grown and transferred as described previously.[35] The MLG samples were heterogenous and consisted of several graphene layers, with the thickest regions at ~20 layers and thinnest regions below 5 layers.[35] In brief, MLG was grown by chemical vapor deposition (CVD) using methane and 25 μm Cu foil as catalyst. The graphene was transferred onto SiO_2/Si wafers through a wet transfer method as described previously.[19] Fully transferred samples were then patterned using tweezers or tape. Substrates were imaged using scanning electron microscopy (Hitachi S-4700).

5.3.3 HgDW Preparation and Characterization

HgDW probes were prepared as previously described.[28] In brief, Pt ultramicroelectrodes (UME) were etched for 2–15 s in saturated $CaCl_2$, 1% HCl using a 60 Hz AC-waveform with a peak-to-peak amplitude of 2.7 V. Thereafter, the etched UMEs were submerged in a $Hg(NO_3)_2$ solution (~10 mM) with KNO_3 supporting electrolyte. We used a Ag/AgCl reference and a tungsten wire counter electrode. The probe was poised to reduce and deposit Hg to slightly overfill the etched cavity, as confirmed via optical microscopy. Finally, a coverslip was used to press and flatten the Hg droplet into a disc.[28] We also used voltammetry to characterize the probe before/after etching and pressing.

5.3.4 Scanning Electrochemical Microscopy and Flux Measurements

All electrochemical measurements were performed using a CHI920D Scanning Electrochemical Microscope (CHInstruments, Inc.) inside an oxygen and moisture-free glovebox (maintained at or below 0.1 ppm). The SECM was placed on a BM-10 Vibration Isolation Platform (Minus K). The MLG substrates were assembled in a standard SECM cell, transferred into the glovebox and rinsed three times with PC before SECM experiments. Thereafter, we replaced the PC with other electrolytes as indicated in the text. We leveled and imaged the substrate using a Pt UME of 12.5 μm radius, with a Pt wire as the counter electrode and a clean Li strip as the reference.

For Li^+ flux measurements, we replaced the SECM probe with a HgDW. We refilled the cell with ~2 mM TMPD, 10 mM $LiPF_6$ and 100 mM $TBAPF_6$ and repositioned the HgDW near the MLG substrate. We collected voltammetry at the HgDW with cyclic voltammetry to measure changes in Li^+ flux in the vicinity of the probe at selected positions on MLG. We applied potential steps to the substrate in 100 mV increments between 2.5 and 0.5 V vs. Li^+/Li to generate the SEI film.

5.3.5 Pulsed CV-SECM

To conduct Li^+ flux imaging, we took two approaches: (1) *in situ* formation of the SEI in the presence of TMPD and subsequent ionic mapping; or (2) preforming the SEI in a Li^+ electrolyte without TMPD. For the 1st approach, we again positioned the HgDW near an MLG substrate using TMPD. Thereafter, the HgDW was cycled while pulsing the MLG substrate to form the SEI or for (de)intercalation at different potentials; typically alternating the potential of the MLG substrate between anodic (more positive) and cathodic (more negative) potentials. After pulsing the MLG at each potential, the probe was rastered across its surface in 10 μm steps. The stripping

peak current, i_{sp}, and integrated substrate charge were extracted for interpreting the results and developing the ionic flux maps.

For the 2nd approach, we preformed the SEI before flux measurements. First, we collected a feedback image using a Pt UME and TMPD; then rinsed the cell thoroughly. Next, we formed the SEI layer on MLG by cycling in 0.1 M $LiBF_4$ electrolyte using recently developed procedures to generate an SEI with full coverage over the substrate, conducive to clear intercalation behavior.[35] After observing reproducible (de)intercalation peaks, we replaced the solution with 5 mM TMPD, 10 mM $LiBF_4$, and 500 mM $TBAPF_6$ in PC:EC. We replaced the Pt UME with a HgDW and positioned the probe for pulsed CV-SECM imaging of the (de)intercalation process. While pulsing the SEI-covered MLG, we used single voltammograms at the HgDW with a 3 s wait time between MLG potential steps. After each potential was measured, the probe was again moved in 10 μm increments across the SEI surface to acquire a profile of changes in Li^+ along MLG.

5.4 Results and Discussion

5.4.1 Li^+ Flux Measurement during SEI Formation at MLG

First, we focused on evaluating Li^+-based SEI formation at MLG substrates deposited on SiO_2. The MLG films were grown via CVD[19,35] and showed large micron-sized grains (Fig. 5.1a). By utilizing the redox mediator, TMPD, we positioned the HgDW probes near the reactive MLG for electron transfer and ionic measurements during the SEI formation process (Fig. 5.1b) with the former performed using the redox mediator in the feedback mode, and the latter performed via transient CV-SECM measurements using the reversible amalgamation of Li^+ in Hg. After leveling using a Pt UME, we collected a feedback SECM image of the freshly transferred MLG sample (Fig. 5.1c). In line with previous reports using SECM on graphene-based materials, we observed positive feedback and fast electron transfer across all of our MLG samples[19,38] with

some diffusional broadening near uncovered SiO_2 regions at the MLG edge, and clear negative feedback resulting from diffusional blocking of the redox mediator at the SiO_2.

For evaluating ion flux at MLG, we replaced the Pt UME with a HgDW and compared their voltammetry. As seen in Fig. 5.2a, cyclic voltammetry (CV) of TMPD at the HgDW displayed a similar voltammetric response to that of Pt UME, indicating a comparable probe size and geometry. We observed only a slight discrepancy which we attribute to some recessing of the Hg disc caused by transfer into the glove box. After approaching and positioning the HgDW above the MLG surface (Fig. 5.2b), we cycled the probe for amalgam/stripping of Li^+/Li(Hg), which displayed a consistent signal across multiple cycles (Fig. 5.2c). While continually cycling the HgDW, we biased the MLG electrode to 2.5 V vs. Li^+/Li, then stepped its potential in increments of −100 mV to 0.5 V vs. Li^+/Li with each potential condition held for 12 s. By continually cycling the probe, we could evaluate changes in Li^+ throughout each potential step.

We focused on changes in the stripping peak currents, i_{sp}, to track Li^+ flux occurring near the probe (Fig. 5.2d) during SEI formation and (de)intercalation processes.[15] HgDWs capture Li^+ flux through competition with the substrate (Fig. 5.2d) where a decrease in the absolute value of i_{sp} indicates an influx of Li^+ to the substrate, while an increase above the baseline level indicates outflux.[28,39] In Fig. 5.2e, we extracted i_{sp} from the HgDW measurements for experiments with the HgDW positioned over SiO_2 and above the MLG. These are plotted alongside the integrated current response, i.e. the charge passed, of one of the MLG samples following our previous analysis.[15] We note the baseline i_{sp} can vary slightly for different probes and positioning. With the HgDW positioned above the MLG, we observed a significant decrease in isp potentials near 2.1 V, 1.7 V and below 1 V vs. Li^+/Li. As the substrate was biased for longer times, these peaks became more pronounced as shown comparing measurements at 1.5 s (green curve) and 11 s (orange curve) after the start of the potential step. The substrate response for all of our MLG samples showed a cathodic process occurring between 2.3 V and 2.5 V (Fig. 5.2e) related to SEI

formation in this potential region.[19,35] For the second SEI peak at ~1 V on the MLG response (Fig. 5.2e), we again observed a probe response in line with Li^+ consumption by SEI formation. Previous results on MLG and other graphitic systems indicated multiple cathodic peaks between 2.5 V and 0.4 V during SEI formation,[19,40] though the specific reactions are still unclear.[1]

When sweeping the MLG electrode back positive, the HgDW response did not return to baseline (Fig. 5.3). Consumption of Li^+ at the bulk MLG surface lead to non-localized effects on the tip response[41] likely from a growing concentration gradient near the MLG surface. 2D COMSOL simulations of Li^+ diffusion at this probe-MLG interface agreed that a cathodic pulse at the extended MLG substrate would cause a large decrease in Li^+ and require a significant time (>100 s) to recover back to baseline (Appendix C). Therefore, our results indicated an irreversible SEI-formation process at MLG that did not lead to significant Li+ release.[19,36] To further verify our measurement, we used another MLG sample and positioned the probe above the SiO_2 (Fig. 5.2b and 5.2e). While decreasing the MLG potential, we observed some small change in the i_{sp}; <1.5% standard deviation across the entire potential range, and little difference when comparing measurements at short and long times. Despite the non-localized effects observed at low potentials (<0.7 V vs. Li^+/Li) and accumulated effect from surrounding bulk substrate, our results clearly indicated the sensitivity of the probe toward location-dependent changes of ionic flux as Li^+ was consumed during the SEI formation process.

5.4.2 Coordinating Localized Electron and Li^+ Flux during SEI Formation

Next, we explored CV-SECM based imaging[19,28,29] to evaluate Li^+ flux during SEI formation at different locations. We now focused on pulsing the potential of the substrate between a condition well into SEI formation (0.5 V vs. Li^+/Li) and its reversal to a condition near its onset (1.8 V vs. Li^+/Li), as depicted in Fig. 5.4a. This was done to restore the diffusion layer before stepping the probe to a different location. Pulsing the substrate minimizes non-localized effects as applied in redox competition imaging[42] to provide a more stable background and improved mapping.

We first used feedback with a low concentration of TMPD to ease positioning and to coordinate measurement of electron and ion transfer. After positioning the HgDW near an MLG substrate, we collected a line scan of the feedback response (Fig. 5.4b, black curve). After cycling the HgDW toward amalgamation/stripping with Li^+, we observed <1% standard deviation at the probe across 15 cycles indicating reproducible operation of the probe in the absence of substrate perturbation. We rastered the probe step-wise across the MLG/SiO_2 region while alternating the substrate potential between cathodic pulses at 0.5 V for SEI formation and anodic pulses at 1.8 V (Fig. 5.4b). During initial cathodic pulses, we observed a large Li^+ flux toward the MLG at a lateral distance of ~100 μm from the MLG edge (Fig. 5.5), which we ascribe to substantial SEI formation due to the large potential step and highly reactive, fresh MLG surface. This initial transient sub-sided after ca. 3 pulses. As seen in Fig. 5.4b, changes in i_{sp} indicated the formation of a Li^+ concentration gradient that was primarily localized over the MLG surface. In this case, the local concentration of Li^+ was diminished above the active surface during the cathodic and anodic pulses. We note that the Li^+ flux during the cathodic pulse consistently resulted in a larger decrease in i_{sp}, than the anodic pulse, as expected for a higher rate of SEI formation at 0.5 V vs. 1.8 V. This result agrees well with the substrate response during the pulse measurements (Fig. 5.4c) suggesting irreversible SEI formation reactions.[19]

After measuring the pulsed ionic flux during SEI formation, we again scanned across the same region using feedback with TMPD (Fig. 5.4b, green curve). The electron transfer rate had significantly decreased from the mass transfer limited value observed before forming the SEI, down to $<10^{-5}$ cm s^{-1}.[39,43,44] We observed a correlation between the most active regions of the MLG and changes in i_{sp}. At the 100 μm position in Fig. 5.4b, the edge of the Li^+ gradient was well resolved and showed similar broadening to the feedback response. A notable peak in i_{sp} occurred at 225 μm, which is related to a high feedback region and suggesting some Li^+ release during the anodic pulse. Through our methodology, we were able experimentally confirm that most of the

MLG surface was undergoing passivation and Li^+ consumption during SEI formation. Few regions showed higher reversibility with outward Li^+ flux during anodic pulsing. These results are in line with previous SECM works suggesting heterogeneities and transient events at the SEI.[14]

5.4.3 2D Li^+ Flux Maps of (De)intercalation

Next, we expanded our pulsed mapping methodology to 2D scans while focusing on the (de)intercalation process. In this case, we decreased the cathodic pulses to lower intercalation potentials of 0.1 V vs. Li^+/Li for more reversible Li^+ uptake and release.[19] After positioning the probe near the edge of the MLG substrate (Fig. 5.6a, black box), we again formed the SEI using potential steps at the substrate between 2.5 and 0.5 V. Subsequently, we continued performing line scans with a substrate pulse sequence between 1.8 V and 0.1 V vs. Li^+/Li to drive (de)intercalation. As with the single line scan in Fig. 5.4, we observed a localized decrease in Li^+ near the substrate upon each subsequent line scan (Fig. 5.6b). The diffusional broadening observed in the Li^+ flux measurement was similar to that observed for feedback (Fig. 5.6b). Further, 2D simulations of the probe at different locations with respect to the MLG confirmed this transition from the MLG electrode to its edge and then to the SiO_2 (Appendix C). Finally, after modifying the Y position, we were able to map the edge of the MLG substrate in a composite SECM image (Fig.5.6c) within minutes; showing that our pulsed approach successfully captured the active (MLG) and inactive (SiO_2) regions of the substrate as judged by the clear differences in i_{sp} along the X axis.

With this sample, we did not observe substantial Li^+ outflux during anodic pulses (Fig. 5.7), i.e. an enrichment of the local Li^+ concentration reflected in an i_{sp} value larger than the baseline. We posit that our *in situ* procedure did not form a stable SEI capable of reversible (de)intercalation.[19] Alternatively, it is also possible that the Li^+ outflux signal is convolved with residual Li^+ influx to the substrate. To examine these possibilities, we turned to an MLG sample with a well-defined intercalation signature by preforming its SEI.

With the preformed SEI, we could confirm the (de)intercalation process and minimize interactions between the redox mediator and the forming SEI. After collecting the SECM feedback image of the MLG substrate (Fig. 5.8), we retracted the SECM probe, rinsed the cell and replaced the solution with 0.1 M $LiBF_4$ in PC : EC. During an initial negative sweep, we observed several peaks for the SEI formation process in line with previous report.[19] The SEI passivated the substrate substantially during initial sweeps to a capacitive background. Cycling the substrate at more negative potentials (Fig. 5.8b) showed two sets of reproducible peaks for (de)intercalation, agreeing with previous reports on Li^+ (de)intercalation in similar MLG systems.[19,35,36]

For conducting pulsed imaging, we replaced the solution with 0.5 M $TBAPF_6$, 10 mM $LiBF_4$ and 5 mM TMPD without rinsing. Using feedback, we approached the HgDW to the MLG substrate and cycled it toward Li^+ amalgamation/stripping. While cycling and moving the probe, we pulsed the substrate to 0.06 then 0.3 V vs. Li^+/Li at each location. Each potential was held for 5 s while measuring with the HgDW leading to a total time of ~20 minutes to collect the two pulse images. The MLG response remained consistent across hundreds of pulses (Fig. 5.8b, inset). We attribute the fluctuations during the initial pulses to restabilization and further formation of the SEI.

We observed good matching between the feedback response (Fig. 5.8c), collected before initiating pulsed imaging, and the pulsed (de)intercalation images (Fig.5.8d and 5.8e) using the same step-size. As seen in Fig. 5.8c, the feedback current indicated negative feedback at the SiO_2 and a mostly passivated SEI-covered MLG displaying some positive feedback. Fig. 5.8d shows that the feedback-active MLG surface induced an inward Li^+ flux while biasing the electrode to 0.06 V. This behavior is expected for the influx of ions caused by intercalation. The subsequent anodic pulses (Fig. 5.8e) showed a higher i_{sp} than the cathodic pulses across the entire surface suggesting Li^+ release by the MLG. This strongly suggests the ability of our probe to detect inward and outward fluxes and to leverage the positioning capabilities of the SECM to map active areas

engaged in these processes. This represents an improvement over our recently reported methodology which explored single locations.[15]

Fig. 5.8e again indicated a lower i_{sp} compared to the initial i_{sp} baseline (56 nA, Fig. 5.9). Still, we observed much larger differences between the cathodic and anodic pulses compared with the *in situ* formed SEI (Fig. 5.6c). We believe the probe response at this potential remains affected by some process that continuously consumes Li^+, as we observed previously.[15] The exact cause remains unclear. Additionally, we observed some changes in the background Li^+ level above the insulating region indicating some disturbance from the pulsed protocol. Despite these issues, our approach revealed broad possibilities for understanding ion fluxes near active battery electrode materials. Understanding ionic flux at different times and locations, and further correlating these properties with other relevant battery parameters such as electron transfer, will be key to detangling the complex chemistry occurring during formation and evolution of battery interphases.

5.5 Conclusions

In conclusion, we introduced an SECM approach that acquired localized redox and ionic information at an evolving MLG interface used as a Li^+ intercalation electrode. We developed a mapping methodology for Li^+ and redox reactivity by first exploring the use of a pulsing sequence at the substrate coupled to HgDW SECM probe operation and rastering. Our methodology was capable of detecting Li^+ fluxes resulting from SEI formation and intercalation processes with temporal and spatial resolution over various MLG geometries. While forming the SEI with potential steps, we first observed a broad signal indicating Li^+ consumption which was consistent with the irreversible nature of Li^+ uptake while forming the SEI at MLG. By pulsing the substrate during ionic imaging, we observed location-dependent uptake of Li^+ across MLG-SiO_2 surfaces; Li^+ uptake was observed on progressively passivated regions towards electron transfer, confirming the insulating nature of the SEI. Diffusional broadening during Li^+ flux mapping was shown to be

consistent with that displayed by feedback measurements, and further confirmed via COMSOL simulations. Upon polarizing the MLG further negative toward (de)intercalation, we observed further SEI formation and location-specific uptake of Li^+ that coordinated well with heterogeneous substrate distribution in feedback mapping. By coordinating potential pulse methods at the substrate with displacements of the SECM probes we gained swift access to exploring both reversible and irreversible processes involving Li^+ fluxes.

We expect that further miniaturization of the probes to submicron sizes (50–300 nm radius), ongoing in our laboratory, will lead to higher spatial resolution to better match the substrate geometry, e.g. individual grains/domains, particles, etc.[45] Hg probes of smaller electrode size can be prepared,[18] but face their own challenges including saturation of the small Hg volume, droplet loss during handling, and more tedious probe characterization. Along with the developments in this work, unlocking the potential of Hg probes will provide vast opportunities to tackle relationships between interfacial processes and cycling performance in next-generation ion batteries.[46–48]

5.6 Acknowledgments

The authors gratefully acknowledge financial support from the National Science Foundation under grant NSF CHE 1709391. Sample preparation and characterization were carried out in part in the Materials Research Laboratory, University of Illinois. Z. T. G. acknowledges the ACS Division of Analytical Chemistry Summer Fellowship and the Hinoree T. and Mrs Kimiyo Enta Fellowship for support. J. R.-L. acknowledges the Alfred P. Sloan Foundation Fellowship.

5.7 Figures

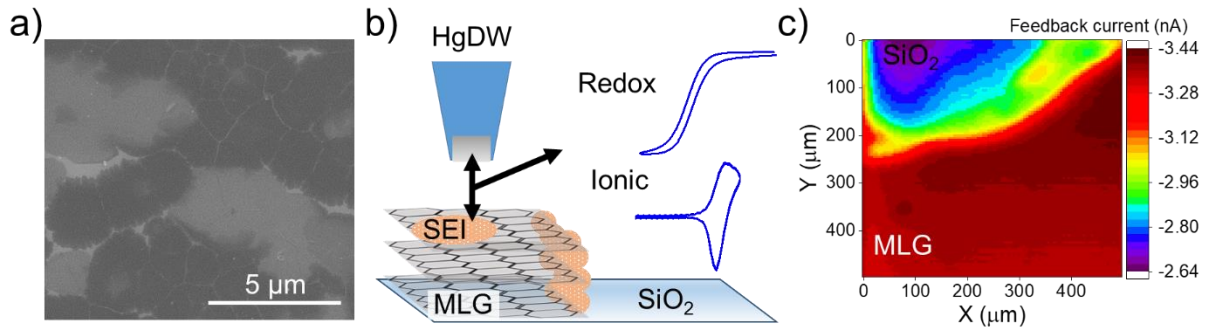

Figure 5.1. Analysis of MLG using multimodal probes with SECM. (a) SEM micrograph of a fresh MLG substrate. (b) Illustration of multimodal measurements using the HgDW, capable of steady-state amperometry using a redox mediator for feedback SECM imaging or reversible amalgamation with alkali ions for measuring and imaging ionic reactivity. (c) SECM feedback image of an MLG substrate before SEI formation using 1.5 mM TMPD. The probe was positioned 12 µm above the MLG surface for imaging.

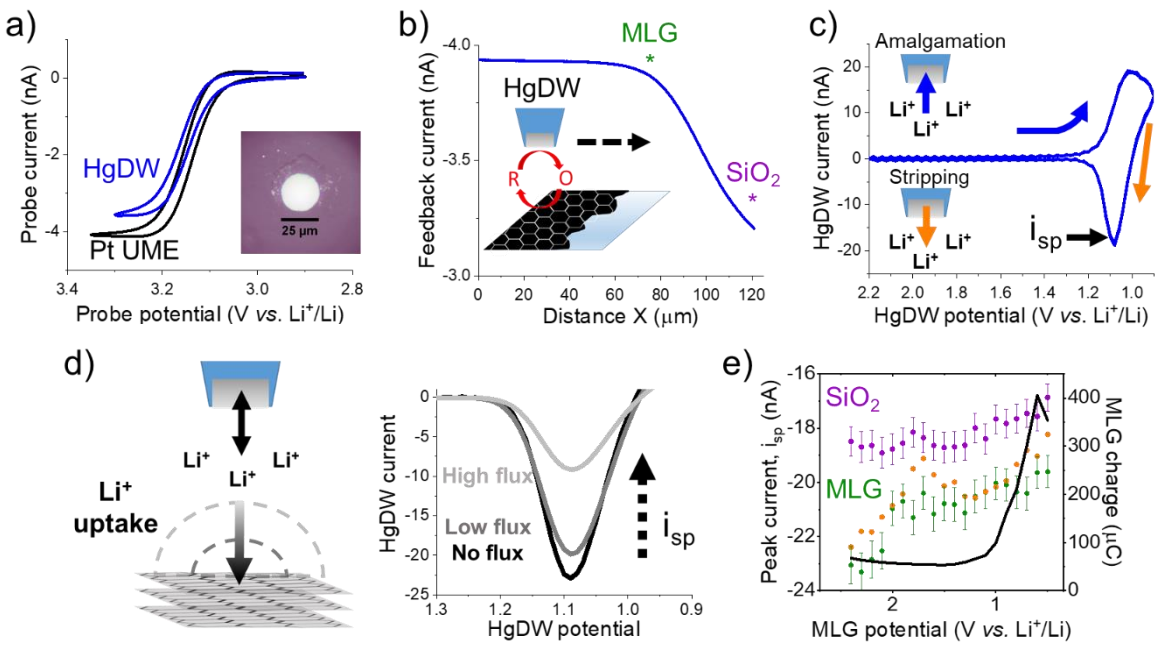

Figure 5.2. Tracking Li^+ during SEI formation on MLG. (a) Comparison of cyclic voltammetry of 2 mM TMPD at a HgDW and Pt UME of the same electrode radius after transfer into a glovebox. The inset shows the pristine HgDW after Hg deposition and pressing. (b) Line scan across the MLG and SiO_2 wafer for positioning the HgDW. The probe positions are indicated relative to the MLG surface during two measurements, on separate samples. The inset is an illustration depicting the line scan process for positioning using a redox mediator. (c) Amalgamation/stripping voltammetry of Li^+ at the HgDW probe for 5 cycles before initiating SEI formation. The stripping peak current, i_{sp}, is labelled. (d) Diagram of competition between the HgDW and an MLG substrate during lithiation and the effect on i_{sp}. (e) Extracted i_{sp} and integrated charge at MLG for each potential step during the first SEI cycle with the HgDW positioned above the SiO_2 and MLG. The green curve involves measurements collected 1.5 s after each potential step. The orange curve are collected later at ~11 s. For the probe above SiO_2, we determined a standard deviation of less than ±1.5% i_{sp} as indicated with the error bars.

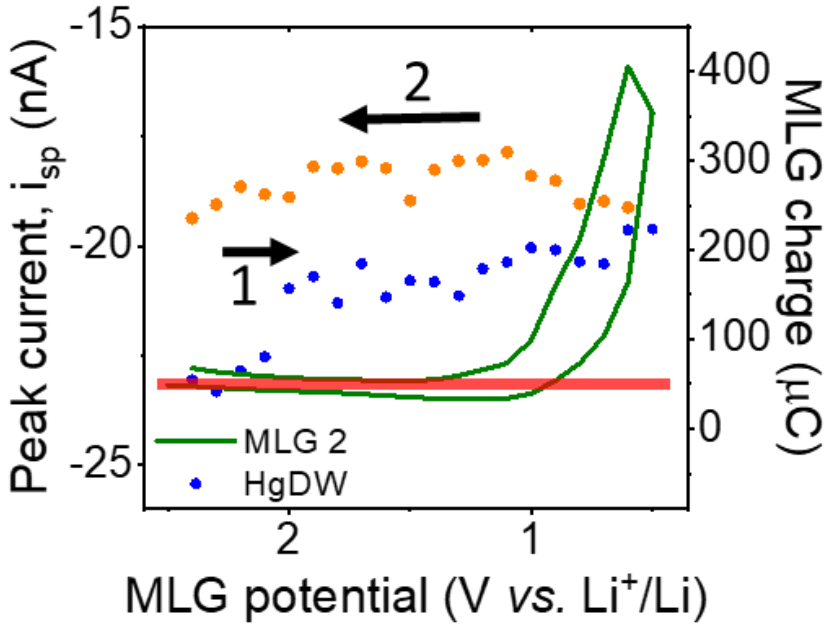

Figure 5.3. HgDW response at MLG during forward and reverse sweeps while forming the SEI.

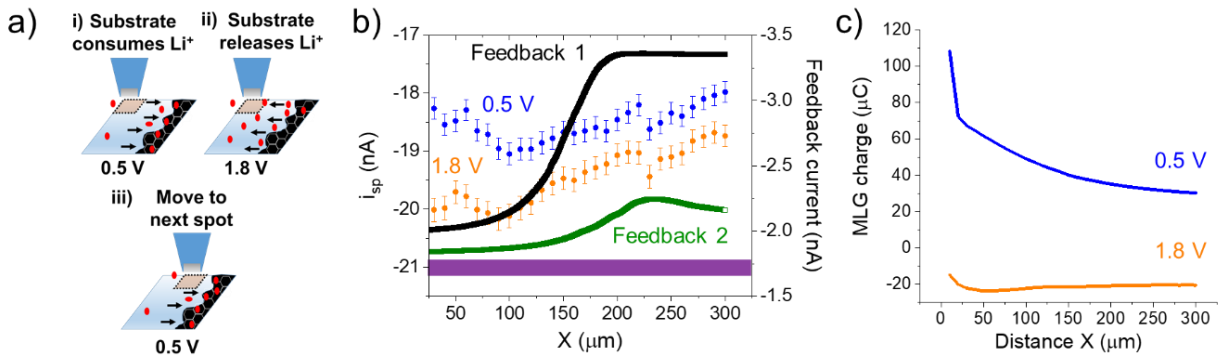

Figure 5.4. Measuring Li^+ during line scans across MLG while pulsing. (a) Illustration of the pulsing methodology for acquiring Li^+ flux maps. (b) Measurements of i_{sp} during pulsing while scanning across an MLG substrate during SEI formation. Ionic data overlay feedback measurements using 1.5 mM TMPD before (black) and after the SEI line scan (green). The purple band represents the baseline isp before polarizing the MLG with its standard deviation of ±1%. (c) Integrated response of the MLG substrate during each pulse.

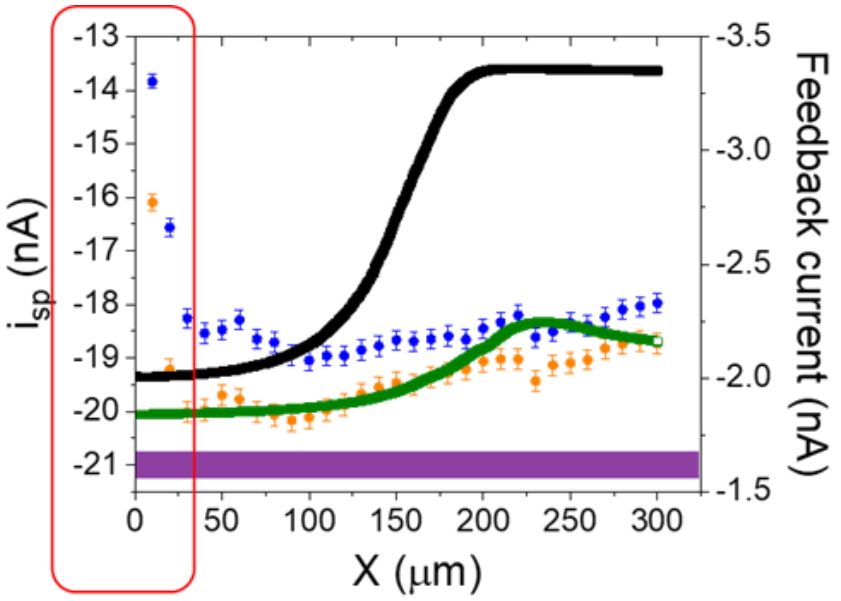

Figure 5.5. Response of the HgDW during initial pulses at MLG while acquiring a line scan profile of Li^+ consumption during SEI formation.

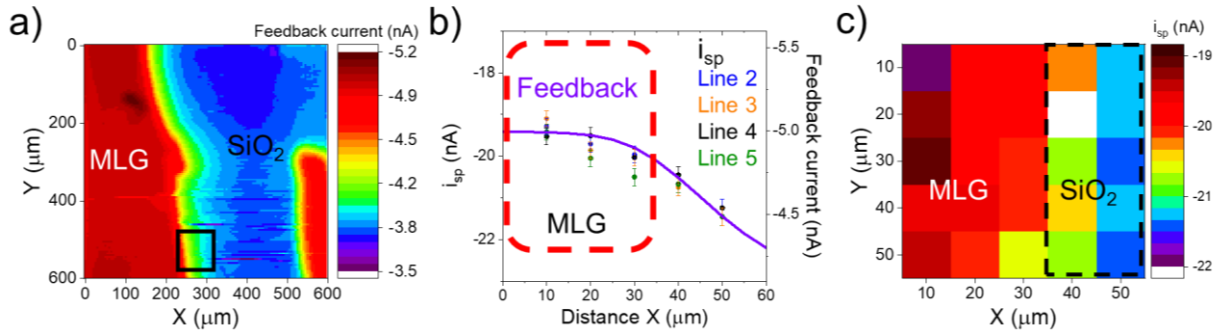

Figure 5.6. Measuring redox and ion transfer at the peripheries of an MLG surface. (a) SECM feedback image before SEI formation using 2 mM TMPD. The approximate location of interest is shown using the black square. (b) Comparison of variation in feedback using TMPD (purple) and i_{sp} while scanning in the X-direction away from the MLG electrode. Feedback current was measured at OCP before forming the SEI. Ion measurements were collected while applying pulses at 1.8 V (anodic) and 0.1 V (cathodic) for (de)intercalation. (c) Composite Li^+ flux image from the cathodic pulse (Li^+ uptake) measurements. For every pixel, we applied 2.6 s pulses to the substrate, totaling ~6 minutes to collect the flux image.

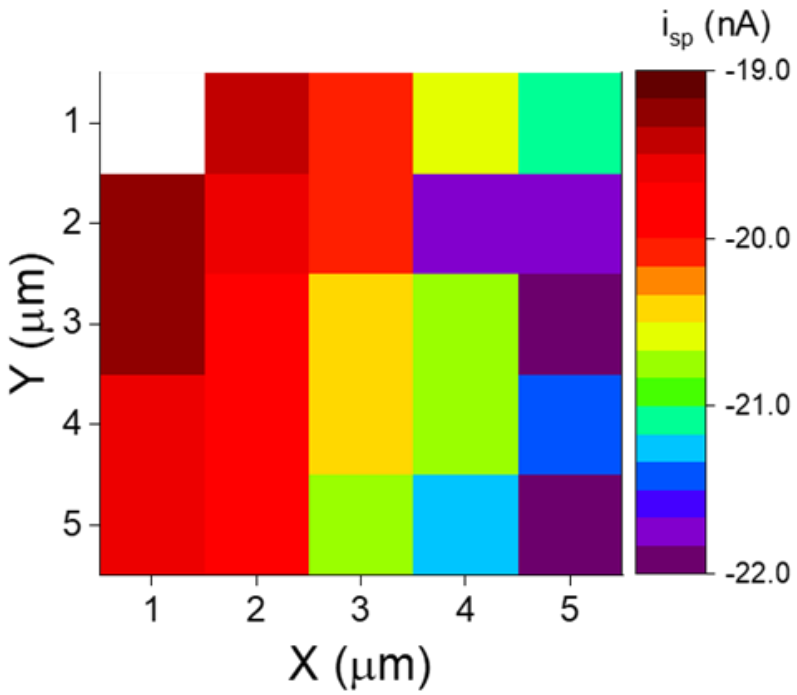

Figure 5.7. Li^+ flux map during anodic pulses (1.8 V vs. Li^+/Li) for deintercalation.

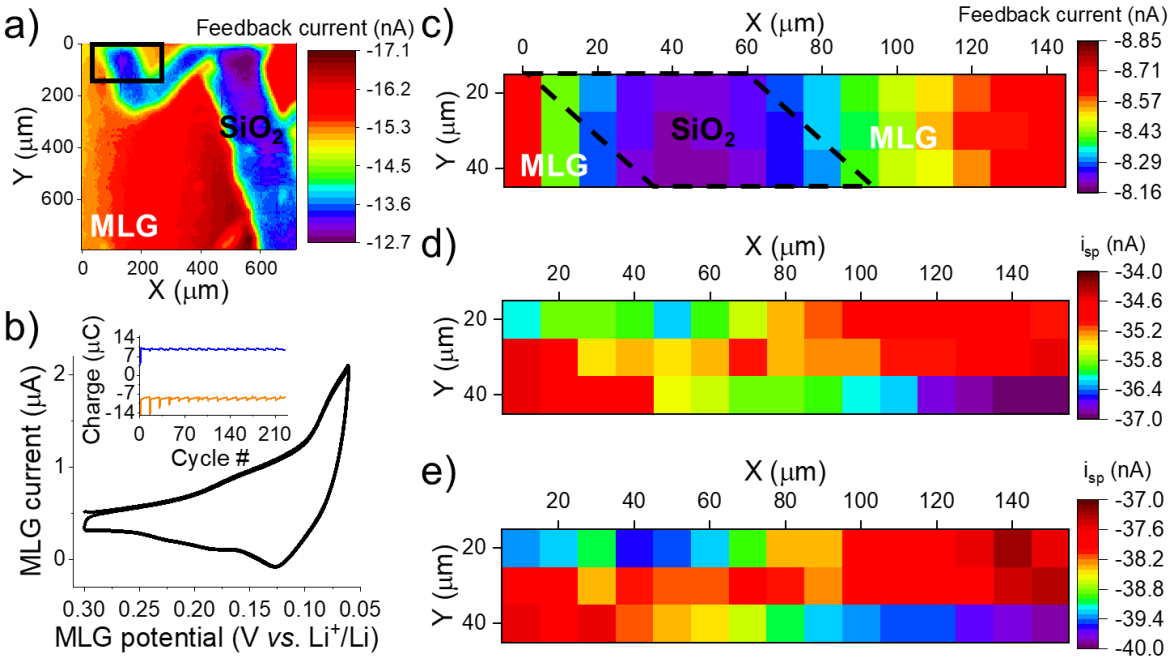

Figure 5.8. Ionic flux mapping on a preformed SEI. (a) Feedback image of a mark on the MLG substrate before SEI formation. A Pt UME was used for imaging in 0.1 M $LiBF_4$, 5 mM TMPD in PC:EC. (b) Voltammetry of (de)intercalation after SEI formation in 0.1 M $LiBF_4$. The inset shows the integrated MLG response during pulsed ionic imaging for pulses at 0.06 (blue) and 0.3 V (orange). (c) Feedback imaging using 5 mM TMPD across the SEI covered MLG. (d) Li^+ flux image during intercalation pulses at 0.06 V. (e) Li^+ flux image during deintercalation pulses at 0.3 V. For every pixel we applied 1.5 s pulses with a 3 s quiet time between each pulse, totaling ~20 minutes to collect the flux image.

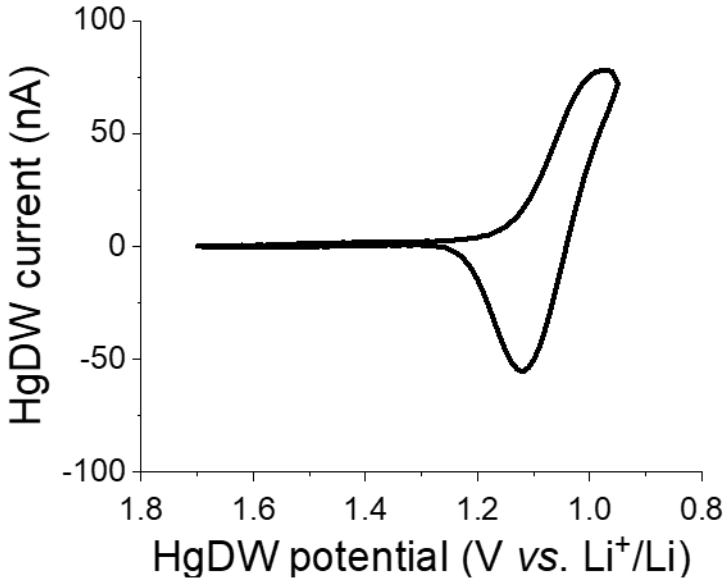

Figure 5.9. CV of HgDW after positioning and before imaging of Li^+ flux at a preformed SEI on MLG.

5.8 References

(1) A. M. Tripathi, W.-N. Su and B. J. Hwang, *Chem. Soc. Rev*., **2018**, 47, 736–851.

(2) J. Hui, Z. T. Gossage, D. Sarbapalli, K. Hernández-Burgos and J. Rodríguez-López, *Anal. Chem*., **2018**, 91, 60–83.

(3) G. Crabtree, G. Rubloff and E. Takeuchi, *Basic research needs for next generation electrical energy storage, Report of the Office of Basic Energy Sciences Workshop on Energy Storage*, U.S. Department of Energy Office of Science, Washington, D.C., **2017**.

(4) S. K. Heiskanen, J. Kim and B. L. Lucht, *Joule*, **2019**, 3, 2322–2333.

(5) M. Ahmed, A. Z. Yazdi, A. Mitha and P. Chen, *ACS Appl. Mater. Interfaces*, **2018**, 10, 30348–30356.

(6) R. Zhao, S. Bobev, L. Krishna, T. Yang, J. M. Weller, H. Jing and C. K. Chan, *ACS Appl. Mater. Interfaces*, **2017**, 9, 41246–41257.

(7) D. X. Liu, J. Wang, K. Pan, J. Qiu, M. Canova, L. R. Cao and A. C. Co, *Angew. Chem., Int. Ed*., **2014**, 53, 9498–9502.

(8) R. Fong, U. Von Sacken and J. R. Dahn, *J. Electrochem. Soc*., **1990**, 137, 2009–2013.

(9) J. Nanda, G. Yang, T. Hou, D. N. Voylov, X. Li, R. E. Ruther, M. Naguib, K. Persson, G. M. Veith and A. P. Sokolov, *Joule*, **2019**, 3, 2001–2019.

(10) C. Cao, I. I. Abate, E. Sivonxay, B. Shyam, C. Jia, B. Moritz, T. P. Devereaux, K. A. Persson, H.-G. Steinrück and M. F. Toney, *Joule*, **2019**, 3, 762–781.

(11) H.-Y. Song and S.-K. Jeong, *J. Power Sources*, **2018**, 373, 110–118.

(12) L. Seidl, S. Martens, J. Ma, U. Stimming and O. Schneider, *Nanoscale*, **2016**, 8, 14004–14014.

(13) D. Lu, J. Tao, P. Yan, W. A. Henderson, Q. Li, Y. Shao, M. L. Helm, O. Borodin, G. L. Graff and B. Polzin, *Nano Lett*., **2017**, 17, 1602–1609.

(14) H. Bülter, P. Schwager, D. Fenske and G. Wittstock, *Electrochim. Acta*, **2016**, 199, 366–379.

(15) Z. T. Gossage, J. Hui, Y. Zeng, H. Flores-Zuleta and J. Rodríguez-López, *Chem. Sci*., **2019**, 10, 10749–10754.

(16) Z. J. Barton, J. Hui, N. B. Schorr and J. Rodríguez-López, *Electrochim. Acta*, **2017**, 241, 98–105.

(17) T. Yamanaka, H. Nakagawa, S. Tsubouchi, Y. Domi, T. Doi, T. Abe and Z. Ogumi, *ChemSusChem*, **2017**, 10, 855–861.

(18) Z. J. Barton and J. Rodríguez-López, *Anal. Chem*., **2014**, 86, 10660–10667.

(19) J. Hui, M. Burgess, J. Zhang and J. Rodríguez-López, *ACS Nano*, **2016**, 10, 4248–4257.

(20) E. Ventosa and W. Schuhmann, *Phys. Chem. Chem. Phys*., **2015**, 17, 28441–28450.

(21) P. K. Hansma, B. Drake, O. Marti, S. A. C. Gould and C. B. Prater, *Science*, **1989**, 243, 641–643.

(22) C.-C. Chen, Y. Zhou and L. A. Baker, *Annu. Rev. Anal. Chem*., **2012**, 5, 207–228.

(23) A. Page, D. Perry and P. R. Unwin, *Proc. R. Soc. A*, **2017**, 473, 20160889.

(24) N. Ebejer, M. Schnippering, A. W. Colburn, M. A. Edwards and P. R. Unwin, *Anal. Chem*., **2010**, 82, 9141–9145.

(25) M. E. Snowden, A. G. Güell, S. C. S. Lai, K. McKelvey, N. Ebejer, M. A. O'Connell, A. W. Colburn and P. R. Unwin, *Anal. Chem*., **2012**, 84, 2483–2491.

(26) L. Danis, S. M. Gateman, C. Kuss, S. B. Schougaard and J. Mauzeroll, *ChemElectroChem*, **2017**, 4, 6–19.

(27) P. Schwager, H. Bülter, I. Plettenberg and G. Wittstock, *Energy Technol*., **2016**, 4, 1472–1485.

(28) Z. J. Barton and J. Rodríguez-López, *Anal. Chem*., **2017**, 89, 2716–2723.

(29) M. A. Claudio-Cintrón and J. Rodríguez-López, *Anal. Chim. Acta*, **2019**, 1069, 36–46.

(30) Z. J. Barton and J. Rodríguez-López, *Anal. Chem*., **2017**, 89, 2708–2715.

(31) R. M. Souto, Y. González-García, D. Battistel and S. Daniele, *Chem. – Eur. J*., **2012**, 18, 230–236.

(32) M. Tang and J. Newman, *J. Electrochem. Soc*., **2011**, 158, A530–A536.

(33) O. C. Harris and M. H. Tang, *J. Phys. Chem. C*, **2018**, 122, 20632–20641.

(34) K. Hernández-Burgos, Z. J. Barton and J. Rodríguez-López, *Chem. Mater*., **2017**, 29, 8918–8931.

(35) J. Hui, N. B. Schorr, S. Pakhira, Z. Qu, J. L. Mendoza-Cortes and J. Rodríguez-López, *J. Am. Chem. Soc*., **2018**, 140, 13599–13603.

(36) S. Petnikota, N. K. Rotte, V. V. S. S. Srikanth, B. S. R. Kota, M. V. Reddy, K. P. Loh and B. V. R. Chowdari, *J. Solid State Electrochem*., **2014**, 18, 941–949.

(37) A. J. Bard, F. R. F. Fan, J. Kwak and O. Lev, *Anal. Chem*., **1989**, 61, 132–138.

(38) C. Tan, J. Rodríguez-López, J. J. Parks, N. L. Ritzert, D. C. Ralph and H. D. Abruña, *ACS Nano*, **2012**, 6, 3070–3079.

(39) A. J. Bard and M. V. Mirkin, *Scanning electrochemical microscopy*, CRC Press, **2012**.

(40) P. Verma, P. Maire and P. Novák, *Electrochim. Acta*, **2010**, 55, 6332–6341.

(41) B. H. Simpson and J. Rodríguez-López, *Electrochim. Acta*, **2015**, 179, 74–83.

(42) K. Eckhard, X. Chen, F. Turcu and W. Schuhmann, *Phys. Chem. Chem. Phys*., **2006**, 8, 5359–5365.

(43) R. Cornut and C. Lefrou, *J. Electroanal. Chem*., **2007**, 608, 59–66.

(44) C. Lefrou, *J. Electroanal. Chem*., **2006**, 592, 103–112.

(45) C. G. Zoski, *Curr. Opin. Electrochem*., **2017**, 1, 46–52.

(46) Y. Li, Q. An, Y. Cheng, Y. Liang, Y. Ren, C.-J. Sun, H. Dong, Z. Tang, G. Li and Y. Yao, *Nano Energy*, **2017**, 34, 188–194.

(47) C. Yang, J. Chen, T. Qing, X. Fan, W. Sun, A. von Cresce, M. S. Ding, O. Borodin, J. Vatamanu and M. A. Schroeder, *Joule*, **2017**, 1, 122–132.

(48) X. Fan, L. Chen, O. Borodin, X. Ji, J. Chen, S. Hou, T. Deng, J. Zheng, C. Yang and S.-C. Liou, *Nat. Nanotechnol*., **2018**, 13, 715.

CHAPTER 6

Reconstruction of Lead Acid Battery Negative Electrodes affected by Hard Sulfation using Controlled Chelation Chemistry

6.1 Abstract

Lead acid batteries (LABs) remain an inexpensive energy storage technology with a wide application base. However, their short cycle lifetimes necessitate improved recycling and maintenance technologies to combat their various failure modes. One major cause of failure is hard sulfation, where the formation of large $PbSO_4$ crystals on the negative active material impedes electron transfer and reversibility. Here, we introduce a protocol to remove hard sulfate deposits on the negative electrode while maintaining their electrochemical viability for subsequent electrodeposition into active Pb. This was accomplished by soaking the hard sulfate negative electrode in an alkaline EDTA solution that reshapes the surface by solubilizing $PbSO_4$ to Pb-EDTA. X ray diffraction suggested that EDTA preferentially dissolved $PbSO_4$ while avoiding Pb phases. Thereafter, we explored the conditions for efficient electrodeposition of the Pb-EDTA complex as fresh electrode material at the resurfaced electrode. Using Pb-EDTA, we found that its reduction to Pb was greatly impacted by solution pH, requiring lower deposition overpotentials as the pH was decreased. We used electrodeposited films on gold to demonstrate reversible cycling of restored active Pb in H_2SO_4. Like commercial battery electrodes, the film's capacity gradually faded with cycling as $PbSO_4$ crystals formed. Lastly, we demonstrated the electrodeposition of Pb films directly onto negative electrodes from a commercial battery

This chapter was submitted to the *Journal of the Electrochemical Society* with authors: Gossage, Z.T.; Guo, F.; Hatfeld, K. O.; Martin, T.; Tian, Q.; Gao, E.; Kumar, K.; Rodríguez-López, J.; and Zhao, H. Z.T.G. wrote the document, made the figures, and collected or guided most of the experiments. K.O.H. helped with Hg probe measurements and collected all optical profilometry. F.G. and others helped guide the original concept and with writing and discussions. The authors gratefully acknowledge financial support from the U.S. Army Construction and Engineering Research Laboratory under cooperative agreements (W9132T1720015 and W9132T1820004). Sample preparation and characterization were carried out in part in the Materials Research Laboratory and the George L. Clark X-Ray Facility and 3M Materials Laboratory, at the University of Illinois

electrode. Our unique approach takes a leap from traditional recycling methods towards in situ protocols and extending the life of a LAB without disassembly or extensive material processing.

6.2 Introduction

Lead-acid batteries (LABs) remain the lowest-cost and most-used secondary battery worldwide with expected market growth to continue alongside the developing automobile industry.[1-3] In spite of their commercial success, LABs have relatively short cycle lifetimes compared to lithium ion batteries (LIBs)[2] and produce extensive waste per year (2.46 million tons in 2014).[4, 5] As such, the need for understanding, preventing, and remediating LAB failure modes, and for extending battery lifetime is becoming more significant.[3, 5-9] One major cause of failure is hard sulfation; this occurs at the negative electrode when LABs are operated under partial state of charge (PSoC), cycled at high rates, deeply discharged, or stored in the discharged state.[6, 10] Lead (II) sulfate ($PbSO_4$) formation occurs on both electrodes as part of the energy storage mechanism, but hard sulfation occurs when the $PbSO_4$ crystals at the negative electrode become too large for effective reduction and impede access to the battery's original capacity. Accumulation of $PbSO_4$ reduces the effective reaction area, increases cell resistance and eventually leads to failure.[6, 7, 11-13] Researchers have directed their attention toward preventing hard sulfation and improving cycle life through additives to the bulk of the negative electrode's active material,[7, 8, 11, 14, 15] electrolyte,[14, 16, 17] and unique charging protocols.[18-20] These methods improve the overall performance and lifetime of the LAB, but primarily apply to new or partially sulfated batteries. Generally, heavily sulfated LABs are recycled after they fail at effectively storing or outputting charge.

Though LABs show high recyclability for the active material, pyrometallurgical processes that utilize high operating temperatures (1100-1300 °C) dominate the field.[3, 5] Several operational drawbacks and environmental concerns are associated with the pyrometallurgical recycling process including highly toxic emissions.[3, 5] Alternatively, LAB electrodes can be recycled through

hydrometallurgical processes that involve solubilization of lead components followed by electrodeposition, or "electrowinning" methods.[21] Though heat is not required for electrodeposition of high purity lead deposits, the process is currently more expensive than pyrometallurgical methods.[5, 21] Typically, the goal of recycling is to separate the battery components and reconstitute them for further applications. Interestingly, significantly less effort has been directed toward developing in situ refurbishing or recycling technologies,[18, 22] though it eliminates the disassembly/reassembly process and could minimize waste.

The liquid electrolyte within flooded LABs is highly accessible for manipulation toward in situ recycling methods. This is evidenced through several reports involving replacing or adding to the existing electrolyte of LABs.[16, 17, 22, 23] Recycling methods also rely on chemical pretreatment steps for dissolving and collecting the spent LAB material.[3, 21] Therefore, in situ, chemical recycling seems plausible for revitalizing the active material. Recently, groups have introduced chelating species, including ethylenediaminetetraacetic acid (EDTA), and other additives to minimize $PbSO_4$ formation. Though these direct additives improved the performance of new LABs,[7, 8, 11, 14, 15] using chelation chemistry to refurbish used and damaged batteries has rarely been considered.[23] EDTA is a strong, tetradentate chelating molecule often used in quantitative analysis due to the 1:1 complexes it forms with metal ions in solution.[24] EDTA is known for its strong chelation to various metal ions including Pb^{2+} with a large formation constant, *K*, of 10^{18}.[25] The ability of EDTA to enhance solubilization of lead salts,[25, 26] including $PbSO_4$,[27] was reported long ago, but few additional efforts have been made to control or understand $PbSO_4$-chelator interactions for use in combatting hard sulfation to extend the life of LAB technologies.

In solution, EDTA is found as a distribution of species with different levels of protonation, e.g. H_4EDTA, H_3EDTA^-, etc.[24] At low pH, as in LABs, EDTA can become fully protonated (H_4EDTA) and tends to precipitate.[24, 26, 28] As such, the level of protonation impacts chelation to other ions in solution through the conditional *K*, or *K'* as described by:

$K' = \alpha_{Y^{4-}} K$

where α represents the fraction of EDTA in one of the protonated forms, and Y^{n-} designates the charge and form with n number of unprotonated groups. By changing the pH, the distribution of protonated species and K' change, because fewer coordinating groups are available for binding.[24] Here, we explored pH as a controlling parameter for driving removal of hard sulfates at the negative LAB electrodes, while simultaneously allowing the facile electrodeposition of the chelated material to restore the negative electrode.

Chelators improve $PbSO_4$ solubility by forming a complex with Pb^{2+} which can be reversibly reduced to redeposit Pb metal.[26, 29] Reduction of the Pb-EDTA chelates can form uniform metal films and the EDTA molecules can be reused for further binding.[26, 30, 31] However, these films are generally not tested as a battery material. Thus, we posited that chelators could be used in a two-step process involving: 1) removal of large, inactive $PbSO_4$ crystals to reactivate damaged electrodes and 2) electrodeposition of fresh electrode material from the Pb-chelator solution (Figure 6.1). Herein, we utilized material characterization and electrochemical methods to explore the concept of in situ refurbishing for hard sulfated LABs. We focused on the negative electrode because it is the most susceptible to irreversible $PbSO_4$ deposits.[6, 18] Our approach takes a leap from traditional recycling methods toward an in situ protocol that would extend the life of a LAB without disassembly or extensive material processing.

6.3 Materials and Methods

6.3.1 Chemicals and Materials

Ethylenediaminetetraacetic acid, disodium dihydrate salt (EDTA (Fisher, ≥99%)) and nitrilotriacetic acid (NTA (Sigma Aldrich, ≥99%)) were used without further purification as chelators. Lead sulfate ($PbSO_4$ (Acro Organics, 99%) and lead nitrate ($Pb(NO_3)_2$ (Fisher, >99%)) were used as lead salts. Sulfuric acid (H_2SO_4, Macron) and sodium hydroxide (NaOH (Fisher,

>99%)) were used for adjusting pH. We used potassium nitrate (KNO_3 (Fisher, >99%)) and sodium sulfate (Na_2SO_4 (Sigma Aldrich, >99%)) as additional supporting electrolytes. Hg probes were prepared with Hg nitrate ($Hg(NO_3)_2$ (Sigma Aldrich, >99.99 %)) as described previously.[32, 33] The Au electrodes were either commercial metal disc electrodes or Au coated onto a silicon substrate with a Temescal electron-beam evaporator. Commercial 6 V lead acid batteries (LABs) were purchased from Yuasa with 5.5 Ah (model - YUAM2655B 6N5.5-1D). All electrolyte solutions were prepared in HPLC grade water (Macron).

6.3.2 Removing Lead Sulfates from Electrodes via Chelation Therapy

Damaged flooded lead acid batteries (US6TMF, 12 V) were received from the U.S. Army after battery failure. We removed the electrolyte and neutralized the inside chamber with a sodium hydroxide solution (***Caution***: residual sulfuric acid is caustic, contains lead, and should be handled with extreme care!). The plastic container was disassembled, and the negative electrodes were collected. The electrode plates were then dried and stored under ambient conditions until further use. To evaluate hard sulfate removal through chelation, we cut the electrode plates into small pieces and soaked them in either: 1) 100 mM EDTA, 2) 100 mM NTA, or 3) water with no chelator. The pH of each soaking solution was adjusted using H_2SO_4 or NaOH. Thereafter, we washed the electrodes with DI water and stored until further measurements. The electrodes were characterized before and after treatment with microscopy and X ray powder diffraction (XRD). For optical and scanning electron microscopy, we utilized a Zeiss and Hitachi S4700 SEM, respectively. For XRD, we used a Rigaku MiniFlex 600 in reflection mode for 2θ between 10° and 100°. Peaks were compared with literature values.[18, 34]

Electrodes from new flooded lead acid batteries were also investigated for chelation treatment. We purchased the LABs from Yuasa and disassembled one before cycling. After cutting the negative electrodes into smaller pieces, we soaked half of each electrode in 100 mM EDTA at different pH values. After 12 hours of soaking, the electrodes were rinsed with water,

dried ambiently and characterized using optical profilometry (Keyence VK-X1000 3D laser scanning confocal microscope).

6.3.3 Electrodeposition of Pb from Pb-Chelator Complexes

All electrochemical measurements were performed using either a CHI760 or a CHI660 potentiostat. We prepared Hg-based ultramicroelectrodes (UMEs) as described previously.[32] Briefly, a 25 µm Pt wire (Goodfellow, 99.9% purity) was sealed in borosilicate glass, sharpened with sandpaper and polished with alumina powder (1 µm) to a flat microdisc.[35, 36] Next, a Hg hemisphere was electrochemically deposited on top of the Pt surface by applying a reducing potential at the Pt UME in a 5 mM $Hg(NO_3)_2$ solution with 100 mM KNO_3 supporting electrolyte.[32, 37-39] We prepared solutions of $PbSO_4$, EDTA, and Na_2SO_4 at different pH (adjusted with NaOH or H_2SO_4). We used a tungsten wire counter electrode, and either a standard calomel electrode, or $Hg/HgSO_4$ as the reference electrode. For simplicity, all potentials were adjusted to $Hg/HgSO_4$. We used cyclic voltammetry at the HgUME to measure Pb-EDTA reduction and Pb stripping. All solutions were bubbled for 10 minutes with Ar to remove oxygen and then adjusted to form an Ar blanket above the solution. To evaluate electrodeposition of Pb films from Pb-EDTA, we used Au disk electrodes (radius = 1 mm) and unused negative electrodes from the Yuasa battery. Potentiostatic and galvanostatic methods were applied to deposit films under ambient conditions. We analyzed the films with microscopy, optical profilometry, and SEM.

6.3.4 Testing of Pb Deposits as Negative Electrode Material

After electrodepositing Pb films, we rinsed the electrodes with fresh water and refilled the cell with 4.2 M H_2SO_4. We cycled the deposited films using cyclic voltammetry or constant current galvanostatic charge/discharge. We compared their cycling behavior with a commercial LAB (Yuasa). The commercial LAB was cycled using a BT-I battery cycler from Arbin Instruments. After deeply discharging the LAB, it was fully charged using a constant potential of 6.2 V (for three

cells in series). Thereafter, it was cycled using a protocol of 500 mA discharge rate (~0.1 C) to 4 V, and 20 mA charge rate (~0.005 C) to 6.4 V. The battery was stopped after thirty charge/discharge cycles.

6.4 Results and Discussion

6.4.1 Interactions between Chelators and Sulfates on Battery Electrodes

First, we evaluated removal of $PbSO_4$ crystals from negative electrode surfaces by immersing and soaking the electrodes in chelator solutions. Electrodes harvested from underperforming commercial flooded LABs (US6TMF) showed extensive coverage by large $PbSO_4$ crystals of various sizes (20-100 µm) as seen in Figure 6.2a. We placed portions of these electrodes into chelator solutions with varied effective formation constants, *K'*, to determine the impact of the chelator species on $PbSO_4$ dissolution. Under high *K'*, such as soaking the electrodes in a pH 10 solution containing 100 mM EDTA, we found that the large crystals were roughened and/or completely removed after 24 hours without agitation (Figure 6.2b). When lowering the EDTA solution pH to acidic conditions (below pH 3), we observed significant EDTA precipitation and only partial removal of the $PbSO_4$ crystals (Figure 6.3). Considering the impact of pH on α_Y^{4-}, α_Y^{3-}, etc., the available binding forms of EDTA diminish dramatically below pH 4. We found similar poor reactivity when using other chelators with a lower *K'*, including nitrilotriacetic acid (NTA), even after soaking for 7 days (Figure 6.3). We also evaluated EDTA on commercial electrodes that were not previously cycled (Yuasa, 6.5 Ah) with small, sub-micron sized crystals across their surfaces. We dipped half of each electrode in an EDTA solution and soaked for 12 hours (Figure 6.2). Again, strong Pb-EDTA binding conditions led to uniform material removal (Figure 6.2c), while lowering the pH (Figure 6.2d) or removing the chelator (Figure 6.4) diminished the removal process. In total, these results suggested that manipulation of pH and *K'* can help control sulfate removal to make it more rapid or gradual depending on the severity of sulfation.

To further investigate the surface reconstruction process, we utilized x-ray diffraction (XRD) before and after treatment (Figure 6.5a). After EDTA treatment, multiple peaks associated with $PbSO_4$ (2Θ = 24, 33, and 52) decreased in intensity, and peaks associated with Pb phases (2Θ = 32, 37, 53, 63) increased.[18, 34] The XRD results suggested that EDTA preferentially attacked $PbSO_4$, while leaving Pb metal phases unperturbed. We further verified the inertness of the EDTA solution with metallic Pb by soaking a piece of Pb metal (37 mg) in excess EDTA (1:10 for Pb:EDTA) at pH 10 for 14 days. The piece remained intact without any apparent dissolution and only 5% mass loss. The enhancement of $PbSO_4$ solubilization by EDTA apparently relies upon interaction with the ionic form of Pb, e.g. Pb^{2+}, which was not readily present at the surface of Pb metal. Taking into consideration the 3D nature of LAB electrodes, targeted removal of inert $PbSO_4$ species at the surface could reveal an underlying layer of metallic Pb that is more reactive and conductive (Figure 6.5B). By making electron transfer sites more accessible, the remaining sulfate crystals would be more readily reduced back to Pb (Figure 6.5b), thereby restoring some of the electrode's original capacity. However, this removal process places much of the Pb content, and thus the battery's original capacity, into a solubilized chelate. To put the chelated material back in service at the negative electrode, we explored a two-step process involving: 1) sulfate removal to reactivate the electrode surface, then 2) using the reactivated electrode to reduce Pb-EDTA directly and redeposit fresh, active electrode material.

6.4.2 Electrodeposition of Pb Films from Pb-Chelator Complexes

In this section, we explored electrodeposition of fresh active electrode material from electrochemical reduction of Pb-EDTA solutions. Previous reports indicated the growth of high purity Pb films through electrolysis of Pb-EDTA, and capacity for reusing the EDTA molecules for further chelation reactions.[26, 40] To evaluate this deposition process, we utilized amalgam/stripping voltammetry at Hg-based microelectrodes (HgUME) (Figure 6.6a-c).[32, 41] HgUMEs are powerful analytical tools for evaluating metal cations in battery systems,[42-44] and can provide quantitative

measurements based on analysis of the stripping peaks.[32, 37, 41, 45] As the HgUME potential is swept negative, Hg can form highly concentrated, reversible amalgams through reduction of the metal cations or their chelates (Figure 6.6b).[32, 33, 37, 46, 47] As shown in Figure 6.6c, EDTA chelation led to a large negative shift, > 400 mV, for forming the Pb-Hg amalgam compared to the ionic salt, $Pb(NO_3)_2$. Therefore, binding to the EDTA inhibited Pb^{2+} reduction, requiring greater overpotentials. Increasing the pH of the Pb-EDTA solution induced negative potential shifts for the Pb-Hg amalgamation process as previously reported on other electrodes.[26, 40] When EDTA was in solution, we only observed a defined forward cathodic wave under acidic conditions. When the pH was very high, the cathodic wave was not resolved due to overlapping solvent processes. However, Pb deposition remained substantial as all the stripping peaks – indicative of redissolution of the amalgamated Pb- were comparable in total charge. Our results agreed that the required overpotential to reduce the Pb-chelator species decreased along with pH and *K'*.[26] From these results, we turned our focus toward low pH conditions for further experiments, as this also represents a condition that is more energetically favorable towards our ultimate objective of refurbishing a battery.

To evaluate Pb film growth, we utilized Au electrodes (Figure 6.7), because Au is visibly distinguishable from Pb, and Au electrodes provide observable stripping peaks for determining deposition potentials.[48, 49] On Au, Pb initially deposits as a sub-monolayer during underpotential deposition before forming bulk films (Figure 6.7a).[49] As seen in Figure 6.7b, electrodeposition of Pb from Pb-EDTA formed a uniform film across the gold electrode when electrodepositing at a constant potential (Figure 6.7c). After deposition, the open circuit potentials shifted to more negative potentials indicating good coverage of Pb on the underlying Au surface. Further, we observed promising results when depositing films while applying a constant current, 57 µA/cm2 in 5 mM $PbSO_4$ for this case (Figure 6.8). We evaluated the impact of Pb-EDTA concentration on film thickness by performing a series of experiments with increasing concentrations of Pb-EDTA.

We observed an increase in Pb film thickness from ~200 nm to greater than 1 µm with increasing Pb-EDTA using a 2 hour deposition time at -1.3 V vs. $Hg/HgSO_4$ (Figure 6.7d,e). The films consisted of densely packed crystallites without any optimization of the deposition process (Figure 6.9). Nevertheless, film characteristics can be manipulated in various ways either through variation of the chemical precursors[50-53] or the electrochemical procedure,[54, 55] emphasizing the vast potential of using an electrochemical procedure in tandem with a removal process to grow fresh electrode material.

After confirming the deposition process, we examined electrodeposition of Pb films directly onto negative electrodes from a commercial, flooded LAB (Yuasa). Other research groups have explored Pb film electrodeposition onto different electrode materials including Pb,[56] Cu,[54, 55] steel,[57] and Pt,[50, 51] but not onto the real negative electrodes found inside LABs. We submerged a fresh negative electrode into a solution containing 20 mM $PbSO_4$ solution with 40 mM EDTA at pH 3. We grew the Pb film at a constant current of 50 mA for 15 hours then rinsed the electrode with water/ethanol and allowed to dry. Thereafter, we compared our deposited film with the original electrode material (Figure 6.10). In this case, our film showed a morphology with larger, flatter Pb deposits (Figure 6.10b) compared to the commercial active material (Figure 6.10d). Realizing that negative electrodes are capable of further electrodeposition is a promising result, because that alone could be used as a strategy for further enhancing the capacity of the LAB or for utilizing alternative deposition chemistries.

6.4.3 Testing Pb deposits as Negative Electrode Material

In this final section, we tested the reaction of the deposited films with H_2SO_4. We grew another Pb film on Au for 10 hours and rinsed the cell thoroughly with water. We refilled the cell with 4.2 M $H2SO_4$ and scanned the potential of the Pb film at 1 mV/s from -1.07 V vs. $Hg/HgSO_4$, where the Pb film was reduced, toward more positive potentials and $PbSO_4$ formation (Figure 6.11a). A large anodic stripping peak, indicative of Pb oxidation to $PbSO_4$, appeared at -0.94 V

vs. $Hg/HgSO_4$ with an integrated charge of 76 mC/cm^2 during the first cycle. When sweeping back negative, we observed an accompanied cathodic peak (onset below -1 V vs. $Hg/HgSO_4$) for reduction of the $PbSO_4$ species back to Pb. The film's $E_{1/2}$ matches well with the redox potential of $Pb/PbSO_4$ at -0.966 V vs. $Hg/HgSO_4$ at 25 C°.[58] Neither of these peaks were observable on the bare Au (Figure 6.12) meaning that our methodology isolated the electrochemical response of the deposited film. We observed a fade in the film's capacity during further CV cycling at 0.5 mV/s (Figure 6.11a). By integrating the forward/reverse peaks, we compared the capacity accessed during each cycle with results on a commercial LAB (Figure 6.11b). We observed a similar fade signature and a continual inefficiency in the charge step compared to the discharge.[6, 34] The large difference in coulombic efficiency was likely due to the much faster charge/discharge rate (both at >1 C) for the film compared to the commercial LAB (0.1 C for discharge/0.005 C for charge). After cycling, the deposited film became covered by $PbSO_4$ crystals (Figure 6.11c, 6.13), but remained intact with only some small cracks and peeling of the film. Aside, we tested the electrodeposited material directly on the commercial electrode (Figure 6.14), but the film was poorly adhered and was difficult to distinguish from the negative electrode's own electrochemistry. Altogether, electrodeposited Pb films were clearly able to perform the same energy storage reactions as actual LAB electrodes, suggesting electrodeposition as a promising tool for enhancing the capacity of a battery. Combining surface removal methodologies with electrodeposition could become a powerful technology for rebuilding or enhancing battery capabilities.

6.5 Conclusions

We introduced a methodology for clearing Pb negative electrodes from hard sulfate deposits via a chelation procedure, and further using the resulting chelate-metal solutions for an electrodeposition step to refurbish the electrode. We showed that species such as EDTA, which display a strong chelating effect, are very effective mediating species for removal of hard sulfation

solid $PbSO_4$ deposits. In line with equilibrium chemistry postulates, controlling the pH resulted in a strategy to control the completeness of $PbSO_4$ deposit removal; however, the chelation strength also determined the overpotential required for electrodeposition from the resulting Pb-EDTA solutions. These observations were possible through electroanalytical stripping measurements at HgUME probes, which elucidated the impact of pH and electrode potential for Pb deposition. Informed by these experiments, we controlled film growth to directly test deposited films for reaction with H_2SO_4. We found the films could reliably cycle the same reaction found in a commercial LAB leading to gradual capacity fade and $PbSO_4$ formation at the film surface. In total, our refurbishing procedure harnesses the dual functionality EDTA, opening new directions for in situ recycling and life extension of LABs even after extreme sulfation or electrode damage. Future directions in our laboratory include the design of new strong chelators that incorporate desirable properties for operating at extreme pH and that optimize the overpotential needed for electrodeposition.

6.6 Figures

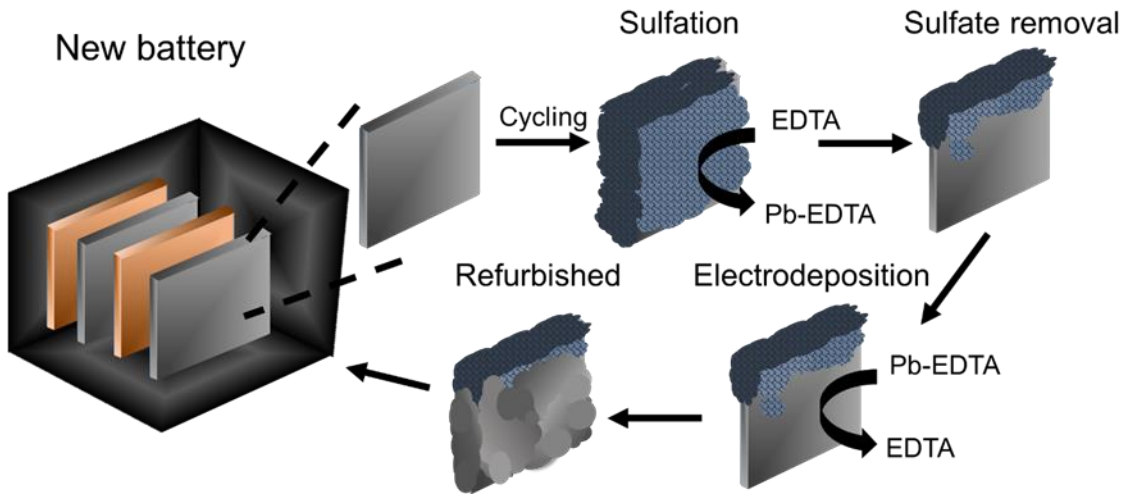

Figure 6.1. Multistep electrochemical process for *in situ* refurbishing for LABs.

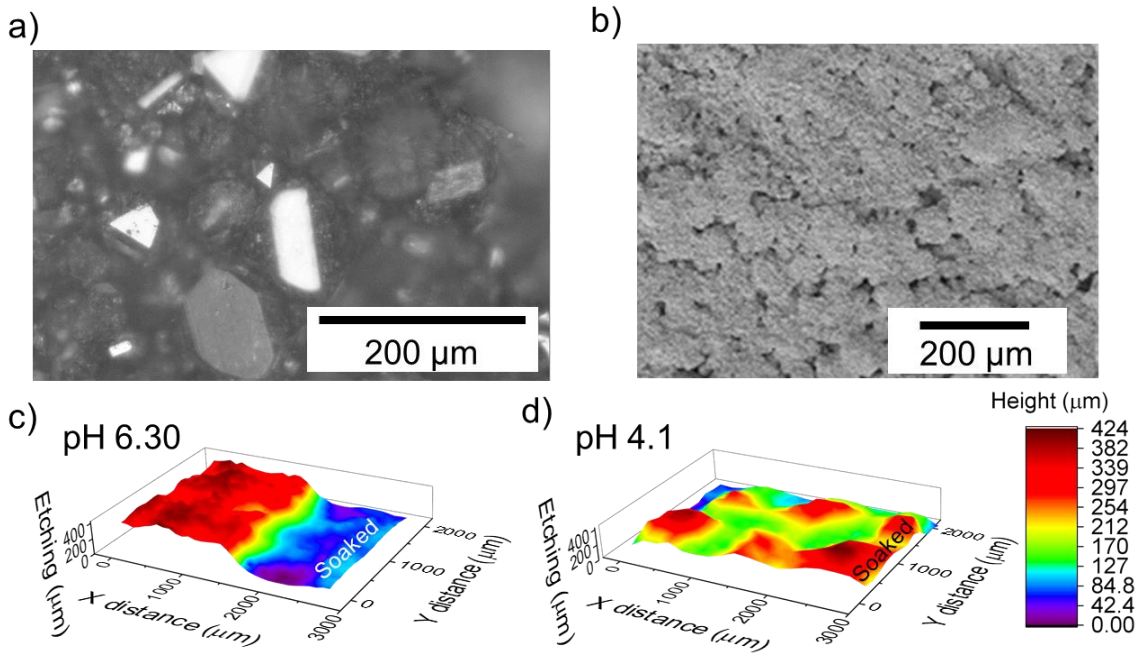

Figure 6.2. Removal of $PbSO_4$ from negative electrodes with EDTA. a) Optical microscopy of heavily sulfated electrodes (US6TMF). b) SEM image of same electrode after soaking in a 100 mM EDTA solution at pH 10 for 24 hours. Optical profilometry of unused negative electrodes (Yuasa) after soaking half the electrode in 100 mM EDTA at (c) pH 6.3 and (d) 4.1 for approximately 12 hours.

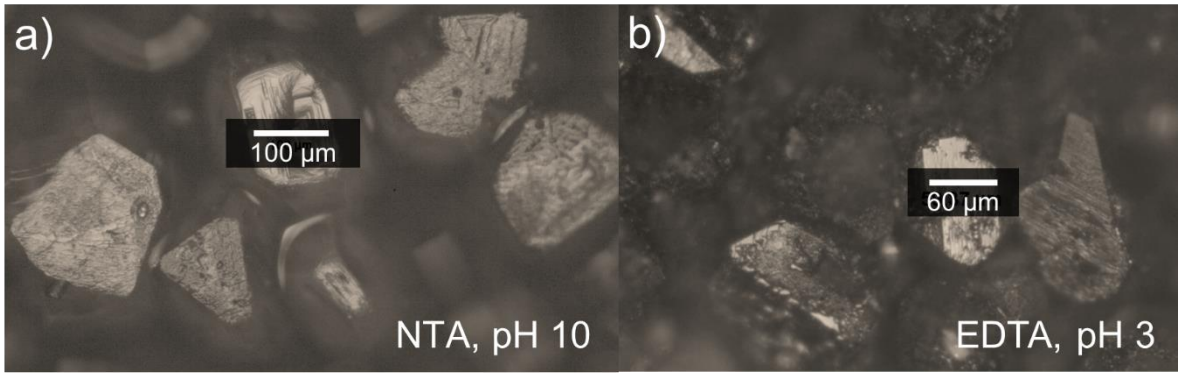

Figure 6.3. Microscopy of underperforming electrodes after soaking in chelator solutions. a) Etched sulfate crystals across the negative electrode (US6TMF, 12 V) after soaking in 100 mM NTA pH 10 for 7 days. b) Etched sulfate crystals after soaking in 100 mM EDTA pH 3 for 7 days.

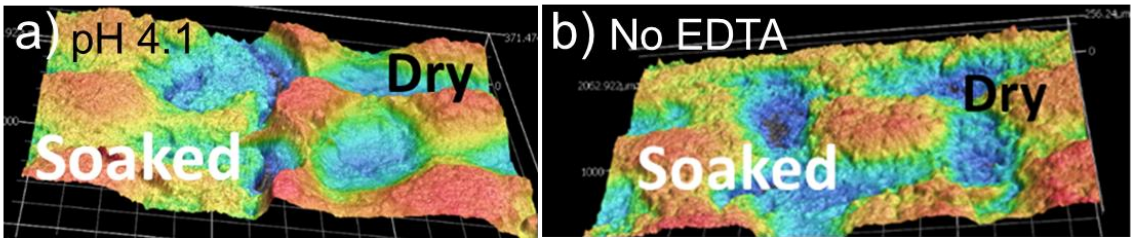

Figure 6.4. Optical profilometry after soaking. Results with half the electrode dipped into 100 mM EDTA solutions at (a) pH 4.1 and in (b) water. The electrodes were soaked for ~ 12 hours.

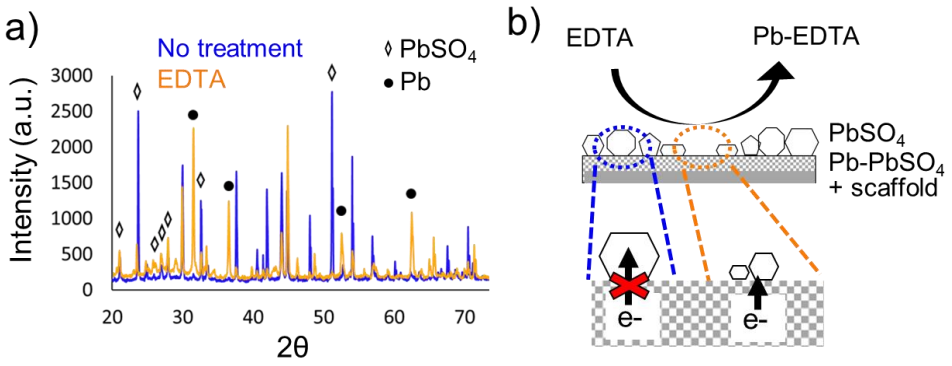

Figure 6.5. Electrode surface restructuring during EDTA treatment. a) XRD before and after treatment in a 100 mM EDTA solution at pH 10 for 24 hours. Peaks for $PbSO_4$ and Pb are identified with markers. b) Illustration of the surface reshaping process and its impact on sulfate reduction after interacting with EDTA.

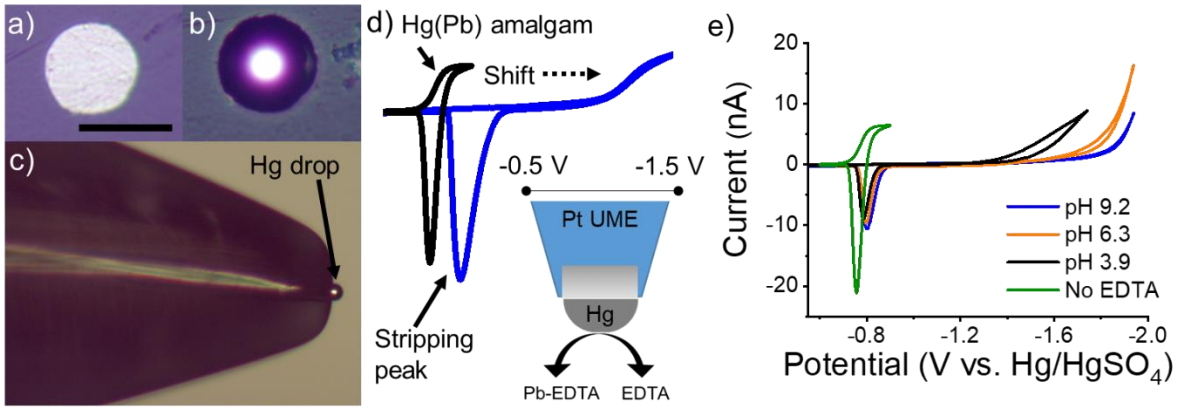

Figure 6.6. Analysis of pH impact on Pb-EDTA electrolysis. a) Top view of Pt UME before Hg deposition. Hg deposited on the Pt UME; (b) top view and (c) side-view. d) Illustration showing voltammetry at a HgUME during amalgam formation and stripping. e) Amalgam-stripping voltammetry at a Hg probe with EDTA and $PbSO_4$ at different pH values compared with $Pb(NO_3)_2$. All solutions contained 100 mM $NaSO_4$ for supporting electrolyte. The pH was adjusted using H_2SO_4 and NaOH.

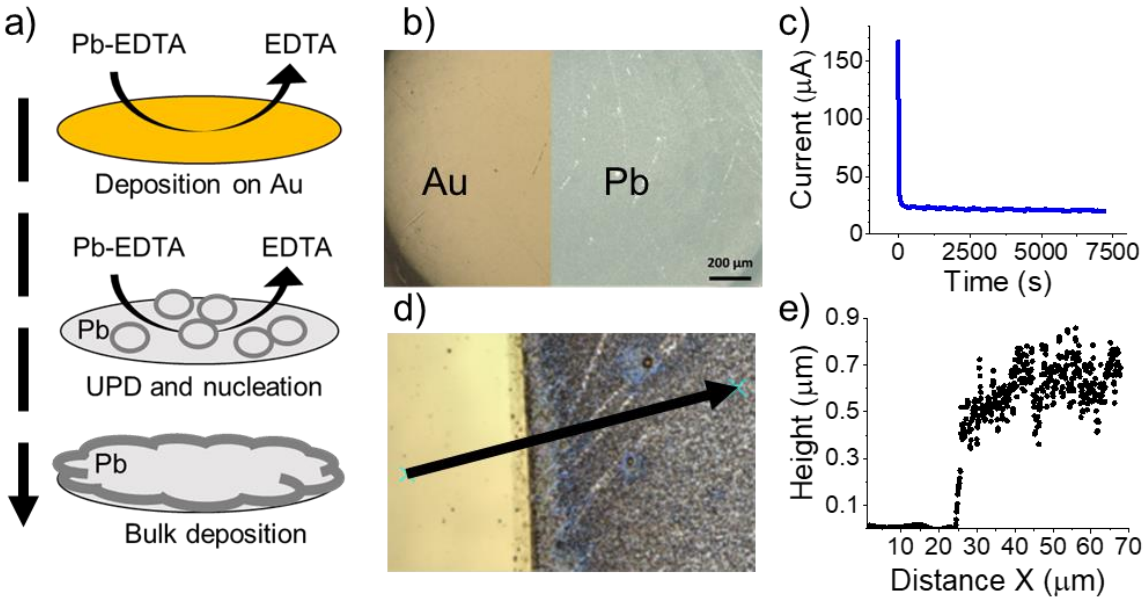

Figure 6.7. Pb electrodeposition on Au macrodisc from Pb-EDTA. a) Diagram of Pb film growth on a Au electrode. b) Macrodisc Au electrode (radius = 1 mm) (left) before and (right) after Pb electrodeposition at -2 V vs. $Hg/HgSO_4$. c) The i-t response during the electrodeposition process. The deposition solution consisted of 5 mM $PbSO_4$, 10 mM EDTA, and 100 mM Na_2SO_4 at pH 4.65. d) Microscopy and (e) optical profilometry of a Pb film electrodeposited on Au at -1.3 V vs. $Hg/HgSO_4$ for 2 hours using 20 mM $PbSO_4$, 40 mM EDTA, 100 mM Na_2SO_4, at pH 3. The arrow in (d) shows the path of the optical profilometry of the film.

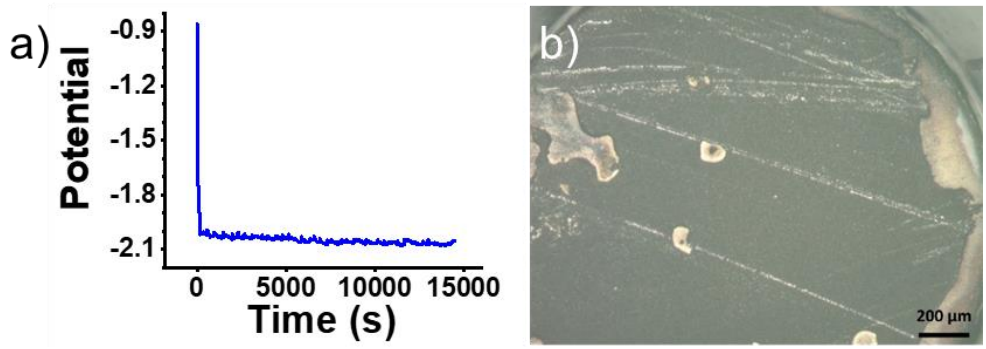

Figure 6.8. Pb film deposition on a gold electrode using constant current. a) Change in potential during galvanostatic deposition of Pb on a gold macrodisc electrode. The applied current was 57 µA/cm^2. b) Optical microscopy of the Pb film after electrodeposition. The electrode had a 2 mm diameter.

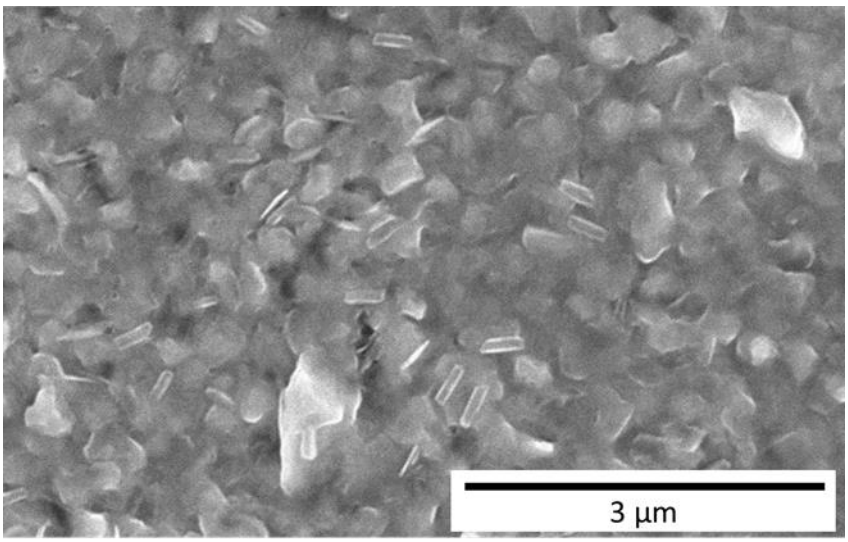

Figure 6.9. SEM of electrodeposited Pb film after 5 hours of deposition at -2.0 V.

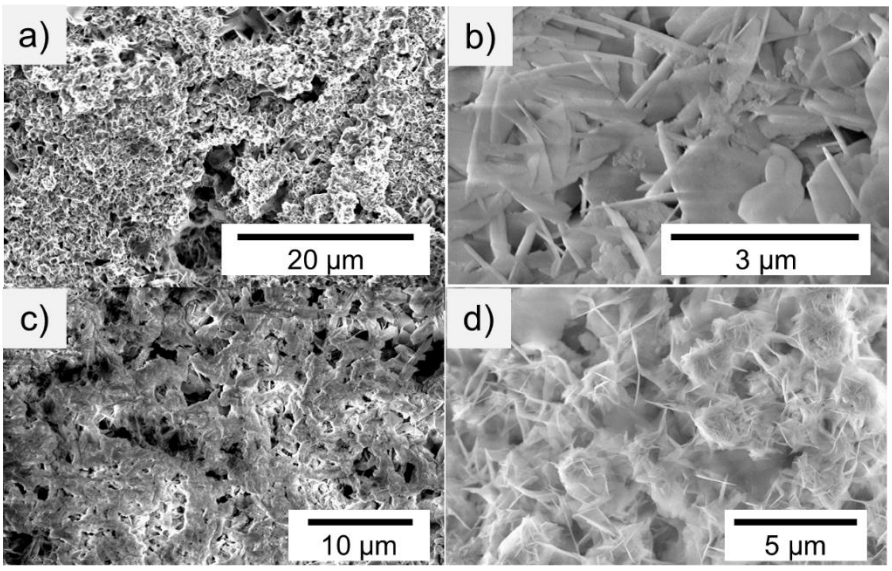

Figure 6.10. SEM of uncycled active material and electrodeposited Pb. a) Electrodeposited Pb and (b) close-up. c) Commercial negative electrode and (d) close-up.

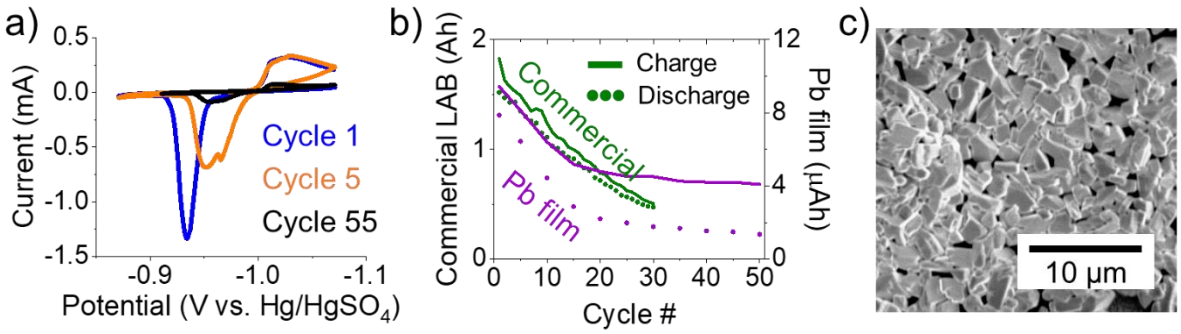

Figure 6.11. Testing electrodeposited films in 4.2 M H_2SO_4. a) Cycling the electrodeposited Pb film on a gold electrode (2.5 mm electrode radius) in 4.2 M H_2SO_4. The film was scanned at 0.5 mV/s between -1.07 and -0.8 V vs. $Hg/HgSO_4$. b) Comparison of peak integration during CV cycling of the Pb film and constant current cycling of a commercial battery at 0.1 C for discharge/0.005 C for charge. Solid lines indicate charge while dotted lines indicate discharge. c) SEM of the Pb film after cycling.

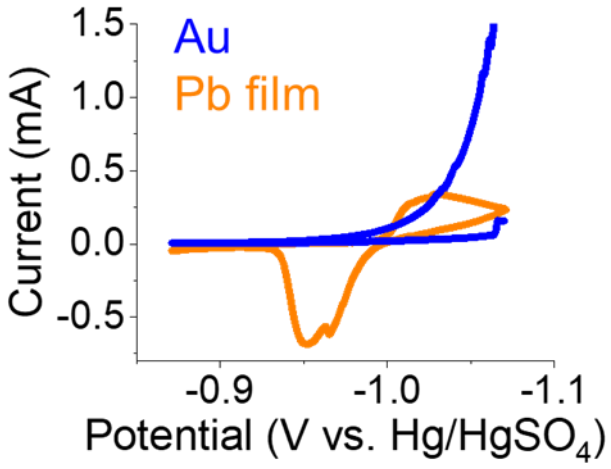

Figure 6.12. CV of H_2SO_4 on Au before and after Pb deposition.

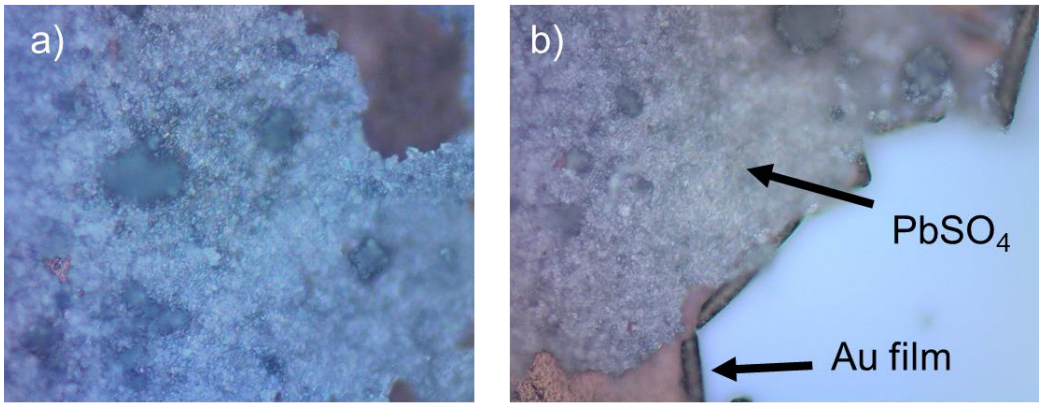

Figure 6.13. Pb/$PbSO_4$ film deposited on Au after cycling in 4.2 M H_2SO_4. Middle region of film with some (a) holes and (b) peeling.

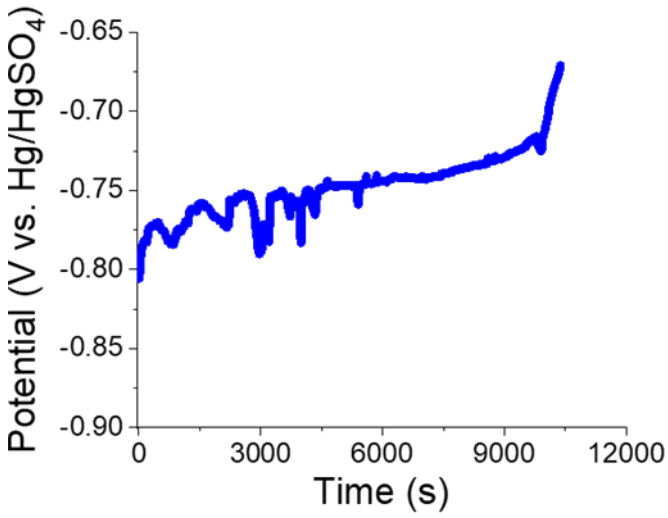

Figure 6.14. Discharge of film deposited on commercial negative electrode in 4.2 M H_2SO_4. The electrode/film was discharged at 1 μA.

6.7 References

(1) Schmidt, O.; Hawkes, A.; Gambhir, A.; Staffell, I., *Nat. Energy*, **2017**, 2 (8), 17110.

(2) Cano, Z. P.; Banham, D.; Ye, S.; Hintennach, A.; Lu, J.; Fowler, M.; Chen, Z., *Nat. Energy*, **2018**, 3 (4), 279.

(3) Zhang, X.; Li, L.; Fan, E.; Xue, Q.; Bian, Y.; Wu, F.; Chen, R., *Chem. Soc. Rev*., **2018**, 47 (19), 7239-7302.

(4) Sun, Z.; Cao, H.; Zhang, X.; Lin, X.; Zheng, W.; Cao, G.; Sun, Y.; Zhang, Y., *Waste Management*, **2017**, 64, 190-201.

(5) Zhang, W.; Yang, J.; Wu, X.; Hu, Y.; Yu, W.; Wang, J.; Dong, J.; Li, M.; Liang, S.; Hu, J., *Renew. Sust. Energ. Rev*., **2016**, 61, 108-122.

(6) Catherino, H. A.; Feres, F. F.; Trinidad, F., *J. Power Sources*, **2004**, 129 (1), 113-120.

(7) Shapira, R.; Nessim, G. D.; Zimrin, T.; Aurbach, D., *Energy Environ. Sci.*, **2013**, 6 (2), 587-594.

(8) Long, Q.; Ma, G.; Xu, Q.; Ma, C.; Nan, J.; Li, A.; Chen, H., *J. Power Sources*, **2017**, 343, 188-196.

(9) Liu, K.; Tan, Q.; Liu, L.; Li, J., *ACS Sustain. Chem. Eng*., **2020**, 8 (9), 3547-3552.

(10) Pavlov, D., *Lead-acid batteries: science and technology*. Elsevier: **2011**.

(11) Moseley, P. T., *J. Power Sources*, **2009**, 191 (1), 134-138.

(12) Lam, L. T.; Haigh, N. P.; Phyland, C. G.; Urban, A. J., *J. Power Sources*, **2004**, 133 (1), 126-134.

(13) Zou, X.; Kang, Z.; Shu, D.; Liao, Y.; Gong, Y.; He, C.; Hao, J.; Zhong, Y., *Electrochim. Acta*, **2015**, 151, 89-98.

(14) Vangapally, N.; Gaffoor, S. A.; Martha, S. K., *Electrochim. Acta*, **2017**, 258, 1493-1501.

(15) Banerjee, A.; Ziv, B.; Shilina, Y.; Levi, E.; Luski, S.; Aurbach, D., *ACS Appl. Mater. Interfaces*, **2017**, 9 (4), 3634-3643.

(16) Yin, J.; Lin, Z.; Liu, D.; Wang, C.; Lin, H.; Zhang, W., *J. Electroanal. Chem*., **2019**, 832, 152-157.

(17) Petkova, G.; Nikolov, P.; Pavlov, D., *J. Power Sources*, **2006**, 158 (2), 841-845.

(18) Zhang, B.; Zhong, J.; Li, W.; Dai, Z.; Cheng, Z., *J. Power Sources*, **2010**, 195 (13), 4338-4343.

(19) Spanos, C.; Berlinger, S. A.; Jayan, A.; West, A. C., *J. Electrochem. Soc*., **2016**, 163 (8), A1612-A1618.

(20) Al Zyoud, A.; Elhaija, W. A., *J. Energy Storage*, **2019**, 25, 100843.

(21) Tan, S.-y.; Payne, D. J.; Hallett, J. P.; Kelsall, G. H., *Curr. Opin. Electrochem*., **2019**.

(22) Karami, H.; Asadi, R., *J. Power Sources*, **2009**, 191 (1), 165-175.

(23) Zeine, M., *Electrolyte and sulfuric acid battery containing same*. Google Patents: **2017**.

(24) Harris, D. C., *Quantitative chemical analysis*. Macmillan: **2010**.

(25) Kim, C.; Lee, Y.; Ong, S. K., *Chemosphere*, **2003**, 51 (9), 845-853.

(26) Allen, H. E.; Chen, P. H., *Environ. Prog*., **1993**, 12 (4), 284-293.

(27) Capelato, M. D.; Cassiano, N. M.; Ramos, L. A., *J. Chem. Educ*., **1995**, 72 (9), 845.

(28) Belcher, R.; Gibbons, D.; West, T. S., *Anal. Chim. Acta*, **1955**, 12, 107-114.

(29) Juzeliunas, E.; Pickering, H. W.; Weil, K. G., *J. Electrochem. Soc*., **2000**, 147 (3), 1088-1095.

(30) Ding, L.; Liu, F.; Cheng, J.; Niu, Y., *J. Appl. Electrochem*., **2018**, 48 (2), 175-185.

(31) Barbosa, L. L.; De Almeida, M. R. H.; Carlos, R. M.; Yonashiro, M.; Oliveira, G. M.; Carlos, I. A., *Surf. Coat. Technol*., **2005**, 192 (2-3), 145-153.

(32) Barton, Z. J.; Rodríguez-López, J., *Anal. Chem*., **2014**, 86 (21), 10660-10667.

(33) Barton, Z. J.; Rodríguez-López, J., *Anal. Chem*., **2017**, 89 (5), 2716-2723.

(34) Saravanan, M.; Ganesan, M.; Ambalavanan, S., *J. Power Sources*, **2014**, 251, 20-29.

(35) Bard, A. J.; Fan, F. R. F.; Kwak, J.; Lev, O., *Anal. Chem*., **1989**, 61 (2), 132-138.

(36) Kwak, J.; Bard, A. J., *Anal. Chem*., **1989**, 61 (11), 1221-1227.

(37) Nepomnyashchii, A. B.; Alpuche-Aviles, M. A.; Pan, S.; Zhan, D.; Fan, F.-R. F.; Bard, A. J., *J. Electroanal. Chem*., **2008**, 621 (2), 286-296.

(38) Baldo, M. A.; Daniele, S.; Mazzocchin, G. A., *Electrochim. Acta*, **1996**, 41 (6), 811-818.

(39) Mauzeroll, J.; Hueske, E. A.; Bard, A. J., *Anal. Chem*., **2003**, 75 (15), 3880-3889.

(40) Juang, R.-S.; Wang, S.-W.; Lin, L.-C., *J. Membr. Sci*., **1999**, 160 (2), 225-233.

(41) Wehmeyer, K. R.; Wightman, R. M., *Anal. Chem*., **1985**, 57 (9), 1989-1993.

(42) Gossage, Z. T.; Hui, J.; Zeng, Y.; Flores-Zuleta, H.; Rodríguez-López, J., *Chem. Sci.*, **2019**, 10 (46), 10749-10754.

(43) Barton, Z. J.; Hui, J.; Schorr, N. B.; Rodríguez-López, J., *Electrochim. Acta*, **2017**, 241, 98-105.

(44) Hui, J.; Burgess, M.; Zhang, J.; Rodríguez-López, J., *ACS Nano*, **2016**, 10 (4), 4248-4257.

(45) Daniele, S.; Baldo, M.-A.; Ugo, P.; Mazzocchin, G.-A., *Anal. Chim. Acta*, **1989**, 219, 19-26.

(46) Alpuche-Aviles, M. A.; Baur, J. E.; Wipf, D. O., *Anal. Chem*., **2008**, 80 (10), 3612-3621.

(47) Wu, H. P., *Anal. Chem*., **1996**, 68 (9), 1639-1645.

(48) Wang, J.; Tian, B., *Electroanalysis*, **1993**, 5 (9-10), 809-814.

(49) Bonfil, Y.; Brand, M.; Kirowa-Eisner, E., *Anal. Chim. Acta*, **2002**, 464 (1), 99-114.

(50) Wong, S. M.; Abrantes, L. M., *Electrochim. Acta*, **2005**, 51 (4), 619-626.

(51) Cherevko, S.; Xing, X.; Chung, C.-H., *Appl. Surf. Sci*., **2011**, 257 (18), 8054-8061.

(52) Muresan, L.; Oniciu, L.; Froment, M.; Maurin, G., *Electrochim. acta*, **1992**, 37 (12), 2249-2254.

(53) Liu, A.; Shi, Z.; Reddy, R. G., *Electrochim. Acta*, **2017**, 251, 176-186.

(54) Nikolić, N. D.; Branković, G.; Lačnjevac, U. Č., *J. Solid State Electr*., **2012**, 16 (6), 2121-2126.

(55) Carlos, I. A.; Matsuo, T. T.; Siqueira, J. L. P.; De Almeida, M. R. H., *J. Power Sources*, **2004**, 132 (1-2), 261-265.

(56) Yolshina, L. A.; Kudyakov, V. Y.; Zyryanov, V. G., *J. Power Sources*, **1997**, 65 (1-2), 71-76.

(57) Carlos, I. A.; Malaquias, M. A.; Oizumi, M. M.; Matsuo, T. T., *J. Power Sources*, **2001**, 92 (1-2), 56-64.

(58) Bard, A. J.; Faulkner, L. R., *Fundamentals and applications. Electrochemical Methods,* **2001**, 2 (482), 580-632.

CHAPTER 7

Ongoing and Future Work

7.1 Abstract

Within this chapter, I present efforts to expand ion-sensitive SECM toward nanomaterials by preparing nanoscale HgDW probes. Thereafter, I show recent work from our group for applications of SECM for evaluating interphases and degradation in cathode materials. Lastly, I discuss using Raman-SECM with contact measurements for single particle spectroelectrochemical measurements. Progress and limitations are discussed.

7.2 Introduction

The work presented throughout this document paves the way for understanding and resolving significant interfacial issues in energy storage. By developing electroanalytical techniques based on SECM, I've shown broad application for extracting localized, fundamental parameters from battery materials. HgDW probes already revealed reaction potentials for Li^+ uptake during SEI formation, stabilization of the SEI, and intercalation kinetics at graphitic electrodes.[1, 2] However, increasing the resolution of Hg probes is highly desirable and would open their application to nanomaterials. Unpublished work with a 300 nm Hg probe are presented herein. Further, I will discuss recent efforts in our group to use SECM probes for evaluating cathode interphase formation and material degradation on a commercial lithium nickel manganese cobalt oxide electrode (NMC). On a different note, Raman and single particle SECM provided invaluable insight into charge transfer and storage within RAPs and RACs.[3, 4] I will

This chapter contains unpublished, on-going research efforts within the Rodriguez-Lopez lab. The NMC experiments were collected by Abhiroop Mishra. Z.T.G. helped develop the methodology and provided guidance throughout the experiments. Raman measurements on single and few RACs were first explored in a joint effort with Dr. Noah Schorr. Z.T.G. collected the Raman and Hg probe measurements presented herein. RACs were provided by Dr. Nagarjuna Gavvallappali and Kevin J. Cheng in Prof. Jeffrey S. Moore's group. Si nanowires were provided by Prof. James Cahoon's group at the University of North Carolina at Chapel Hill.

discuss unpublished efforts to make single particle Raman measurements on viologen-based RACs for a potential Raman-SECM study

7.3 Future Direction #1: Nanoscale Ion-Sensitive SECM

To meet future energy storage needs, researchers have dedicated significant effort toward developing new electrode materials for LIBs.[5] Cathode materials, including $LiCoO_2$, have low theoretical specific capacities of ~140 $mAhg^{-1}$ compared to graphite at 370 $mAhg^{-1}$.[5, 6] Minor improvements in cathodes could have dramatic effects on battery performance, but interfacial issues continue to be problematic.[5, 7] On the anode side, replacement of graphite with conversion or alloying materials would lead to much higher capacities, *e.g*. Si at a theoretical capacity of 4212 mAh^{g-1}.[8-10] Aside, exciting properties are observed among nanoscale battery materials including improved cycling and durability at high rates.[10-14] Shrinking the domain size alleviates some issues with charge transfer, fracture and loss of connection. Bulk measurements have suggested optimal particle sizes for battery performance on the nanoscale,[15] but much remains unknown on the in situ performance of these structures.[16] SECM is a promising platform for analysis of these emerging materials considering advancements with nanoscale probes[17-19] and our recent methodology developments with ion-sensitive measurements.[1, 2, 20, 21]

Our lab has led the way in application of Hg probes to energy storage systems,[1, 2, 20] but exploring nanoscale materials with fast cycling capabilities would require smaller Hg probes. Nanoscale Hg probe were previously demonstrated for quantification of Li^+ and Mn^{2+},[22, 23] and even employed with SECM. As nanoscale SECM probes become more routine,[18, 24] access to nanoscale Hg probes will become more feasible for broad applications in energy storage studies. Building on my previous work,[3, 4] I focused on developing a 300 nm HgDW. This size probe was able to resolve the location of individual Si nanowires across conductive substrates using SECM (Figure 7.1). As a HgDW, the probe will show good stability for SECM compared to a Hg-capped probe,[21] and the etching step provides greater Hg volume to accommodate Li^+ as it moves into

the amalgam. Stable Hg deposition into etched 300 nm Hg probes would greatly improve ion flux mapping resolution and suitability for sub-micron sized battery particles.

Following our etching and deposition procedure,[21] I showed that the same 300 nm probe was stable enough to prepare as a HgDW electrode with etching and deposition (Figure 7.2a). As seen in Figure 7.2b, voltammetry with this probe in a 1 mM $Cd(NO_3)_2$ solution showed amalgamation and stripping peaks with Cd^{2+} at an $E_{1/2}$ of 0.58 vs. Ag/AgCl (reported: 0.5738 V vs. Ag/AgCl[25]). Due to manual sharpening and a large RG between 10-15, the probe was durable enough to press the Hg droplet using a cover slip. Smaller probes prepared through laser pulling would be too delicate for this step. To circumvent this issue, I propose full characterization of the etch depth and referencing to a disc electrode of the same electrode radius.[26] The etch depth can be determined electrochemially[26] and will directly aid modeling efforts.[1] The solid disc electrode provides a known reference Hg^{2+} reduction current for an electrode surface flush with the surrounding glass. Deposition should be stopped near this reference point. Recessed probes can also be identified and characterized.[26] Alternatively, thin Hg films may be more amenable to laser-pulled nanoelectrodes.[27]

Unfortunately, HgDW probes at this scale were very susceptible to losing their Hg droplet during electrodeposition, disconnecting the lead after deposition, or during transfer into the glovebox. Resolving these issues may require a deposition procedure within the glovebox and better electrostatic shielding on the probe. Aside, the nanoscale HgDW probes were more susceptible to saturation of their amalgam phase during amalgam-stripping. Perhaps, studies at low electrolyte concentration or faster scan rates could minimize this issue.[27] Ion-sensitive SECM methods show great potential for improving our knowledge on energy storage systems; bringing ion-sensitive SECM probes to the nanoscale will make the analytical methods even more impactful for forefront energy studies.

7.4 Future Direction #2: Cathode Degradation and CEI Formation

Cathodes used in LIBs and beyond have their own interphase properties distinct from anode SEI,[28] and degradation mechanisms involving metal leaching[29, 30] gas evolution and irreversible phase change.[31, 32] These degradation processes simultaneously occur when cathodes, such as NMC, are pushed to extreme states during cycling. When batteries are charged at high rates, the electrodes can experience extreme overpotentials that lead to such undesirable reactions.[33] As with much of the other work referenced throughout this document, localized electrochemical measurements of this process during electrode operation are limited. Analytical tools that provide new information on the origins and progression of these degradation processes could provide insight for improved material design.

Work with SECM showed conductive CEI formation on multiple cathode materials and an insulating film on an oxidizing Al current collector.[28] Interestingly, the CEI's chemical structure contains similar species to the SEI found on the anode,[34] and CEI are observed in aqueous electrolytes.[35] Recently, our group has been exploring cathode degradation through collection methods using SECM.[36, 37] With a Pt SECM probe positioned near an NMC cathode, we collected soluble products while stepping the NMC potential in 20 mV increments from 3.0 to 5.0 V vs. Li^+/Li (Figure 7.3) following our previous methods.[1] By using cyclic voltammetry at the Pt probe while holding each potential at the NMC (Figure 7.3a), we observed the evolution of two redox active species. The first redox active species formed while the electrode remained at open circuit, suggesting spontaneous formation of a CEI.[38] The reaction plateaued at ~2.45 V vs Li^+/Li on our Pt probe and diminished as we stepped the NMC positive toward 5.0 V. From there, we observed the evolution of another species with a peak at 2.75 V and onset near 2.9 V at the probe (Figure 7.3a). As shown for the peak at 2.75 V, we could track changes in each peak compared with the applied NMC potential (Figure 7.3b); indicating at which potentials degradation products were forming. To identify these species further, we considered previous reports[32] and conducted

voltammetry measurements in our solvent system under saturated CO_2 and O_2 conditions. As seen in Figure 7.3c, we observed reduction of O_2 followed by CO_2 reduction at a more negative potential. In this promising preliminary experiment, we demonstrated the application of SECM for collection of multiple solubilized products from a degrading commercial NMC surface during cycling.

Aside from expanding our analysis to further cycling and other materials, a Hg probe could provide complementary or improved information to that collected by a Pt probe. Not only is the Hg probe sensitive to the same evolving products as the Pt UME, but it also provides opportunity to coordinate material degradation with lithiation/delithiation and metal leaching. Hg probes are extremely versatile and sensitive to reaction products at different potentials than Pt UMEs.[25] In combination, these two probes could reveal extensive information of the evolution of the cathode surface during operation and how its CEI forms and stabilizes.

7.5 Future Direction #3: Single Particle Raman-SECM

SECM and Raman are powerful tools that can be coupled for interrogating redox active species for energy storage.[3] Raman-SECM is a recently developed instrument,[3, 39, 40] but very promising due to extensive work combining in situ electrochemical measurements with spectroscopic methods for tying redox properties with structural change.[16, 36, 41] Further, incorporating Raman-SECM with SERS substrates,[42, 43] could enhance surface sensitivity for understanding interphase formation.[44] In situ SERS has been useful for detecting surface intermediates at metal−oxygen battery interfaces.[45, 46] Significant opportunity remains in utilizing Raman-SECM for understanding next generation energy storage systems.

In our single particle works,[3, 4] we separately demonstrated that SECM could be used to make direct contact to single RACs and that the Raman microscope could be combined with SECM to track local viologen charge/discharge using a non-contact technique.[37, 47] Throughout

the process, we tried to combine the two ideas and simultaneously interrogate a single particle with both the SECM contact and Raman measurements (Figure 7.4a). As seen in Figure 7.4b, we could locate RACs adhered to the surface of an ITO electrode through a CCD camera in line with the laser.[3] From there, we aligned the laser to single RAC using a 50X or 100X objective and the CCD. We attempted cycling measurements while at this location (Figure 7.4c,d); barely observing the major Raman peaks for the viologen radical.[3, 48, 49] Regardless, we could see transition back and forth between charged and discharged states, but with poor resolution compared to previous cycling measurements.[4]

To conduct useful cycling measurements, we need to improve this signal-to-noise issue. Future work on Raman-SECM should focus on improved laser positioning, thermal drift prevention,[50] and enhancing the Raman signal[44, 46] and temporal resolution.. To date, all Raman-SECM experiments have been conducted in aqueous environments.[3, 39, 40, 42] A Raman-SECM system inside an inert environment, e.g. glovebox, would open these studies to more extreme potentials and higher energy density systems. Lastly, the combination of HgDW probes[1, 2] with Raman-SECM could provide substantial insight toward interphase formation and stabilization across a material; acquiring structural, ionic, and electronic information at the same location.

7.6 Conclusion

As presented, ion-sensitive modes of SECM are extremely promising tools for evaluating energy storage materials. I discussed progress in preparing nanoscale Hg probes for Interphase formation and ionic flux measurements on nanoscale materials. I showed recent efforts in our lab showing promise for using SECM probes to evaluate cathode degradation. Lastly, I discussed efforts and potential for using Raman-SECM methods for single particle measurements. In total, SECM is a powerful electroanalytical platform, and combining it with ion-sensitive and spectroscopic measurements would make it a very competitive compared to other methods for interphase studies.

7.7 Figures

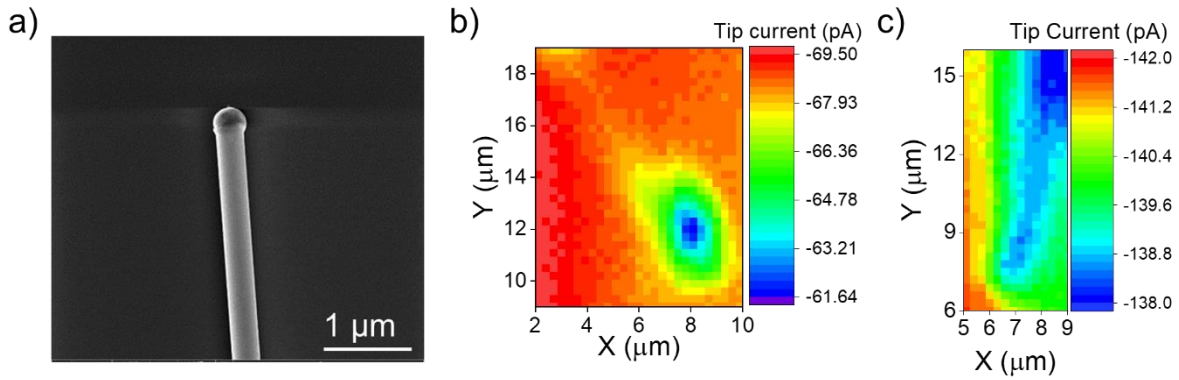

Figure 7.1. SECM measurements of Si nanowires using a 300 nm Pt UME. a) SEM measurement of a nanowire provided by the Calhoon group. b, c) SECM imaging of nanowires on top of graphene substrates. The images were collected using Fc in 100 mM $LiBF_4$ in propylene carbonate.

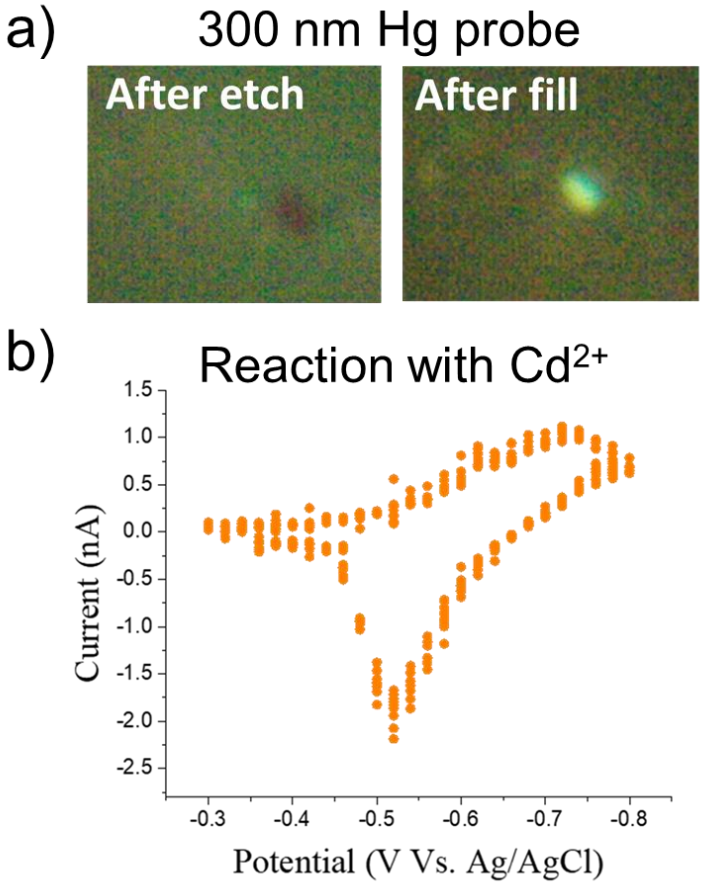

Figure 7.2. 300 nm HgDW probes and amalgamation/stripping. a) On left, Hg probe after sharpening, polishing and etching. On right, Hg probe after depositing and pressing the Hg droplet. b) Voltammetry of the HgDW probe in 1 mM $Cd(NO_3)_2$, 100 mM KNO_3 in water. The reference used was Ag/AgCl. A Pt wire was used as the counter electrode.

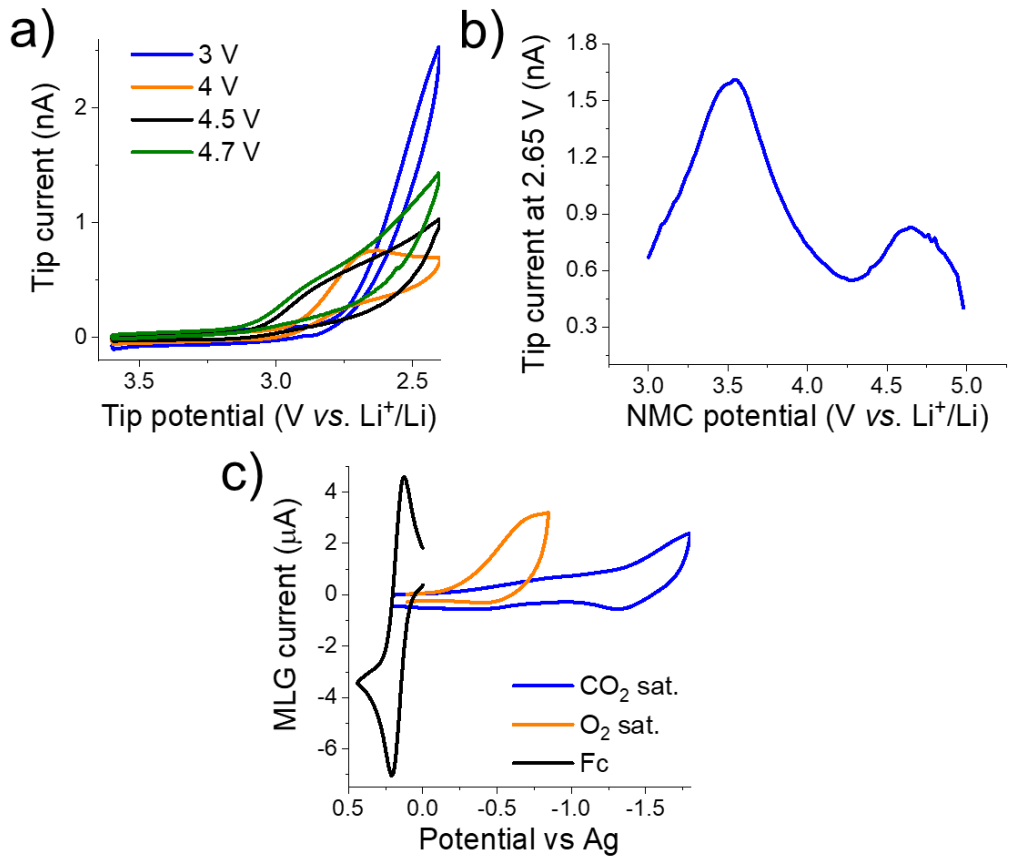

Figure 7.3. Substrate generation-tip collection experiments at an NMC cathode. a) Response of a 12.5 μm Pt microelectrode while collecting CVs above an operating NMC cathode in 0.1 M $LiPF_6$, EC:DEC. Each potential was held at NMC for ~150 s while collecting at the Pt probe. The potential was increased in 20 mV increments. A Pt wire and Li strip were used as the counter and reference, respectively. Measurements were collected inside an inert atmosphere (glovebox - Braun). b) Processed data for the Pt probe response at 2.65 V (O_2 collection). c) Comparison of the redox potentials for CO_2, O_2 and Fc in 0.1 M $LiPF_6$, EC:DEC. CO_2 measurements were collected inside an acrylic glovebox after purging the solution with CO_2. O_2 measurements were collected after purging the solution with O_2 for 10 minutes. For these measurements Pt and Ag wire were used at the counter and reference, respectively.

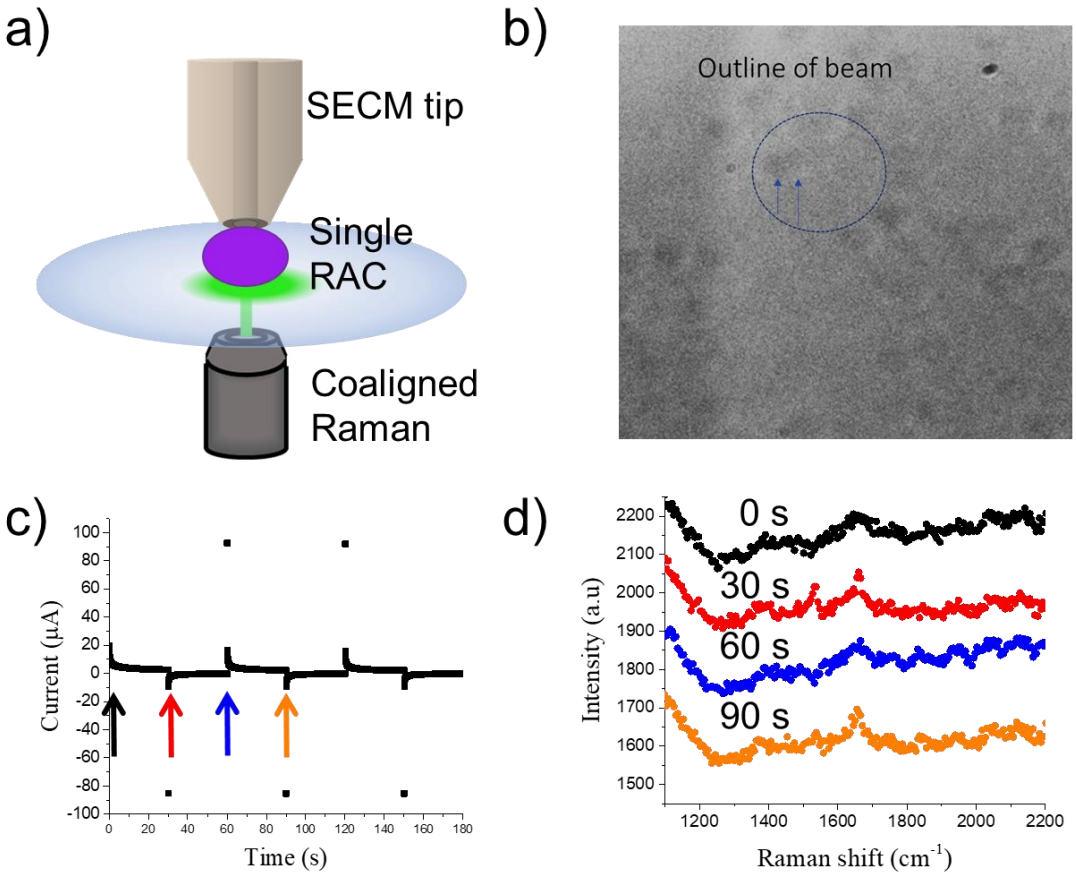

Figure 7.4. Single RAC measurements using Raman-SECM. a) Illustration of a contact measurement for single particle measurements using Raman-SECM. b) CCD image and outline of Raman beam spot before interrogation of one or few RACs with a 50X objective. c) Current response for dispersed RACs on an ITO surface during potentiostatic cycling. d) Raman response during potentiostaic cycling.

7.8 References

(1) Z. T. Gossage, J. Hui, Y. Zeng, H. Flores-Zuleta and J. Rodríguez-López, *Chem. Sci.*, **2019**, 10, 10749-10754.

(2) Z. T. Gossage, J. Hui, D. Sarbapalli and J. Rodríguez-López, *Analyst*, **2020**, 145, 2631-2638.

(3) Z. T. Gossage, N. B. Schorr, K. Hernández-Burgos, J. Hui, B. H. Simpson, E. C. Montoto and J. n. Rodríguez-López, *Langmuir*, **2017**, 33, 9455-9463.

(4) Z. T. Gossage, K. Hernández-Burgos, J. S. Moore and J. Rodríguez-López, *ChemElectroChem*, **2018**, 5, 3006-3013.

(5) E. M. Erickson, C. Ghanty and D. Aurbach, *J. Phys. Chem*., **2014**, 5, 3313-3324.

(6) J. M. Tarascon and M. Armand, in *Materials for Sustainable Energy*, Co-Published with Macmillan Publishers Ltd, UK, **2010**, pp. 171-179.

(7) E. M. Erickson, W. Li, A. Dolocan and A. Manthiram, *ACS Appl. Mater. Interfaces*, **2020**, 12, 16451-16461.

(8) S. Ohara, J. Suzuki, K. Sekine and T. Takamura, *J. Power Sources*, **2004**, 136, 303-306.

(9) I. A. Courtney, *J. Electrochem. Soc*., **1997**, 144, 2045.

(10) J. R. Szczech and S. Jin, *Energy Environ. Sci.*, **2011**, 4, 56-72.

(11) F. Holtstiege, T. Koç, T. Hundehege, V. Siozios, M. Winter and T. Placke, *ACS Appl. Energy Mater*., **2018**, 1, 4321-4331.

(12) X. H. Liu, L. Q. Zhang, L. Zhong, Y. Liu, H. Zheng, J. W. Wang, J.-H. Cho, S. A. Dayeh, S. T. Picraux and J. P. Sullivan, *Nano Lett*., **2011**, 11, 2251-2258.

(13) M. Ge, J. Rong, X. Fang and C. Zhou, *Nano Lett*., **2012**, 12, 2318-2323.

(14) Z. Yi, Y. Liang, X. Lei, C. Wang and J. Sun, *Mater. Lett.*, **2007**, 61, 4199-4203.

(15) J. Yue, F. M. Badaczewski, P. Voepel, T. Leichtweiß, D. Mollenhauer, W. G. Zeier and B. M. Smarsly, *ACS Appl. Mater. Interfaces*, **2018**, 10, 22580-22590.

(16) A. M. Tripathi, W.-N. Su and B. J. Hwang, *Chem. Soc. Rev*., **2018**, 47, 736-851.

(17) T. Sun, Y. Yu, B. J. Zacher and M. V. Mirkin, *Angew. Chem. Int. Ed*., **2014**, 53, 14120-14123.

(18) S. Amemiya, in *Electroanalytical chemistry*, CRC Press, **2015**, pp. 16-87.

(19) P. Wilde, T. Quast, H. B. Aiyappa, Y.-T. Chen, A. Botz, T. Tarnev, M. Marquitan, S. Feldhege, A. Lindner, C. Andronescu and W. Schuhmann, *ChemElectroChem*, **2018**, 5, 3083-3088.

(20) Z. J. Barton, J. Hui, N. B. Schorr and J. Rodríguez-López, *Electrochim. Acta*, **2017**, 241, 98-105.

(21) Z. J. Barton and J. Rodríguez-López, *Anal. Chem*., **2017**, 89, 2716-2723.

(22) Z. J. Barton and J. Rodríguez-López, *Anal. Chem*., **2014**, 86, 10660-10667.

(23) L. Danis, S. M. Gateman, M. E. Snowden, I. C. Halalay, J. Y. Howe and J. Mauzeroll, *Electrochim. Acta*, **2015**, 162, 169-175.

(24) L. A. Baker, *J. Am. Chem. Soc*., **2018**, 140, 15549-15559.

(25) A. J. Bard, L. R. Faulkner, J. Leddy, and C. G. Zoski. *Electrochemical methods: fundamentals and applications*. Vol. 2. New York: Wiley, **1980**.

(26) A. M. Bond, D. Luscombe, K. B. Oldham and C. G. Zoski, *J. Electroanal. Chem*., **1988**, 249, 1-14.

(27) M. A. Alpuche-Aviles, J. E. Baur and D. O. Wipf, *Anal. Chem*., **2008**, 80, 3612-3621.

(28) G. Zampardi, R. Trocoli, W. Schuhmann and F. La Mantia, *Phys. Chem. Chem. Phys*., **2017**, 19, 28381-28387.

(29) G. A. Snook, T. D. Huynh, A. F. Hollenkamp and A. S. Best, *J. Electroanal. Chem*., **2012**, 687, 30-34.

(30) M. Evertz, F. Horsthemke, J. Kasnatscheew, M. Börner, M. Winter and S. Nowak, *J. Power Sources*, **2016**, 329, 364-371.

(31) V. A. Godbole, J.-F. o. Colin and P. Novák, *J. Electrochem. Soc*., **2011**, 158, A1005.

(32) F. La Mantia, F. Rosciano, N. Tran and P. Novák, *J. Electrochem. Soc.*, **2009**, 156, A823.

(33) K. W. Beard, *Linden's Handbook of Batteries*, Fifth Edition, McGraw-Hill Education, New York, N.Y., **2019**.

(34) W. Li, A. Dolocan, P. Oh, H. Celio, S. Park, J. Cho and A. Manthiram, *Nat. Commun*., **2017**, 8, 14589.

(35) S. Liu, D. Liu, S. Wang, X. Cai, K. Qian, F. Kang and B. Li, *J. Mater. Chem. A*, **2019**, 7, 12993-12996.

(36) J. Hui, Z. T. Gossage, D. Sarbapalli, K. Hernández-Burgos and J. Rodríguez-López, *Anal. Chem*., **2018**, 91, 60-83.

(37) A. J. Bard and M. V. Mirkin, *Scanning electrochemical microscopy*, CRC Press, **2012**.

(38) D. Takamatsu, Y. Koyama, Y. Orikasa, S. Mori, T. Nakatsutsumi, T. Hirano, H. Tanida, H. Arai, Y. Uchimoto and Z. Ogumi, *Angew. Chem. Int. Ed*., **2012**, 51, 11597-11601.

(39) N. B. Schorr, A. G. Jiang and J. Rodríguez-López, *Anal. Chem.*, **2018**, 90, 7848-7854.

(40) M. Etienne, M. Dossot, J. Grausem and G. Herzog, *Anal. Chem.*, **2014**, 86, 11203-11210.

(41) C. Gutiérrez and C. A. Melendres, *Spectroscopic and diffraction techniques in interfacial electrochemistry*, Springer Science & Business Media, **2012**.

(42) N. B. Schorr, M. J. Counihan, R. Bhargava and J. Rodríguez-López, *Anal. Chem.*, **2020**, 92, 3666-3673.

(43) J. Clausmeyer, M. Nebel, S. Grützke, Y. U. Kayran and W. Schuhmann, ChemPlusChem, **2018**, 83, 414-417.

(44) L. Cabo-Fernandez, D. Bresser, F. Braga, S. Passerini and L. J. Hardwick, *Batteries Supercaps*, **2019**, 2, 168-177.

(45) I. M. Aldous and L. J. Hardwick, *Angew. Chem. Int. Ed*., **2016**, 55, 8254-8257.

(46) P. M. Radjenovic and L. J. Hardwick, *Faraday Discuss*., **2018**, 206, 379-392.

(47) J. Rodríguez-López, M. A. Alpuche-Avilés and A. J. Bard, *J. Am. Chem. Soc*., **2008**, 130, 16985-16995.

(48) C. L. Bird and A. T. Kuhn, *Chem. Soc. Rev.*, **1981**, 10, 49-82.

(49) C. A. Melendres, *J. Electrochem. Soc.*, **1983**, 130, 1523.

(50) J. Kim, M. Shen, N. Nioradze and S. Amemiya, *Anal. Chem*., **2012**, 84, 3489-3492.

Appendix A: COMSOL Models for Chapter 3

This appendix was published as part of the supplementary materials in two previous articles within (1) *Langmuir* and (2) *ChemElectroChem*:

(1) Gossage, Z.T.; Schorr, N.B.; Hernandez-Burgos, K.; Hui, J.; Simpson, B.H.; Montoto, E.C.; Rodríguez-López, J. "Interrogating Charge Storage on Redox Active Colloids via Combined Raman Spectroscopy and Scanning Electrochemical Microscopy." *Langmuir* **2017**, *33*(37), 9455-9463. DOI: 10.1021/acs.langmuir.7b01121

(2) Gossage, Z.T.; Hernandez-Burgos, K.; Moore, J.S.; Rodríguez-López, J. "Impact of Charge Transport Dynamics and Conditioning on Cycling Efficiency within Single Redox Active Colloids." *ChemElectroChem* **2018***, 5*(20), 3006-3013. DOI: 10.1002/celc.201800736

COMSOL Simulations for Single RAC particles:

Simulations were completed using the Transport of Diluted Species module within COMSOL Multiphysics 4.4, which solves for species diffusion using Fick's laws and reaction kinetics. For single particle simulations, we used a 2D axisymmetric geometry representing a radial cross section of a spherical particle in contact with a nanoelectrode (Figure A1). The only active domain represents the single particle (orange region), where charge diffuses from the point of contact with the probe to the rest of the particle (red line). The diffusion coefficient used for these simulations was extracted from experimental measurements (described in Chapter 3). Within the single particle domain, a viologen (V^{2+}) species was defined with an initial concentration ranging from 0.5 M to 2 M. For single particle electrolysis simulations, we used a concentration

boundary condition at the tip, making the concentration of V^{2+} equal to zero to recreate full reduction of the active species. The particle radius was determined from SECM imaging experiments. All other boundaries were assumed to be insulating via a No Flux condition. Best fits were selected by eye for evaluating the effect of different diffusion coefficients and concentrations on the simulated transients in comparison to the experiment.

For cyclic voltammetry simulations, we set the E^o to 0 for the redox couple with a total concentration of 1 M for the oxidized viologen (V^{2+}) and reduced viologen (V^+) species. The two concentrations were varied for different states-of-charge (e.g. 0.5 M V^{2+} with 0.5 M V^+ for a 50% SoC). We used a flux boundary condition at the probe surface, and recreated Butler-Volmer kinetics to track V^+ flux as the probe voltage swept between 0.3 V and -0.3 V. All other boundaries were assumed to be insulating via a No Flux condition. For cycling simulations, we started by simulating CV with a 0% SoC. Thereafter, we used the final results as the initial conditions for the next simulation/cycle.

Appendix A: Figure

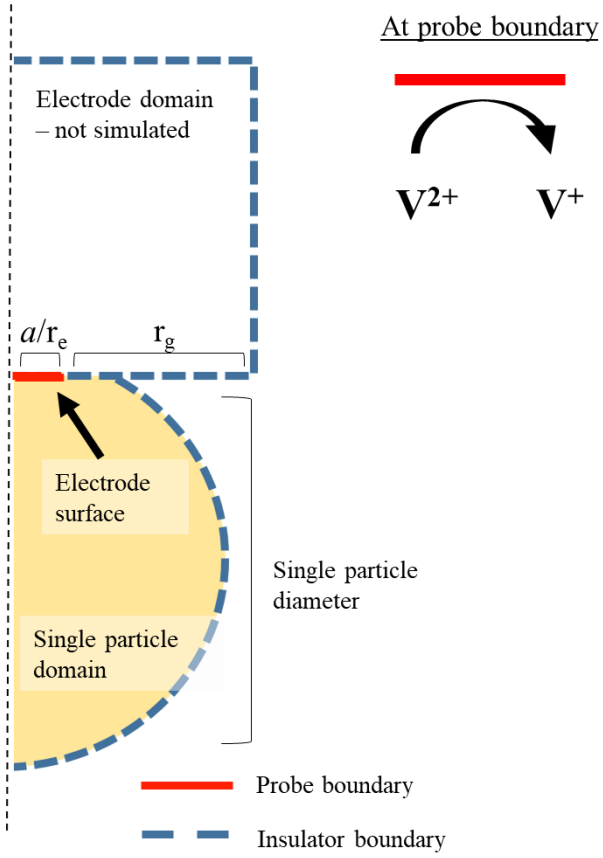

Figure A1. Single particle geometry for COMSOL simulations.

Appendix B: COMSOL Models for Chapter 4

This appendix was published as part of the supplementary materials for an original research article in *Chemical Science*:

Gossage, Z.T.; Hui, J.; Zeng, Y.; Flores-Zuleta, H.; Rodríguez-López, J. "Probing the reversibility and kinetics of Li^+ during SEI formation and (de)intercalation on edge plane graphite using ion-sensitive scanning electrochemical microscopy." *Chem. Sci.*, **2019**, *10*, 10749-10754. DOI: 10.1039/C9SC03569A.

Description of COMSOL Simulations for Intercalation at HOPG:

Simulations were completed using the Transport of Diluted Species module within COMSOL Multiphysics 4.4, using Fick's laws for diffusion. For simulation of the intercalation process, we used a 2D axisymmetric geometry representing a radial cross section of the HgDW probe positioned near the HOPG electrode (Figure B1). Three active domains were defined: 1) Amalgam, 2) HOPG, and 3) Solution. All parameters used in the simulations are listed in Table B1 with reference values. The Amalgam domain and its Flux boundary with the Solution domain involved consumption of species (M^+) at the Flux boundary to produce reduced species (M(Hg)) that could diffuse freely into the Amalgam domain. Likewise, the HOPG domain was defined the same way as the Amalgam domain but with its own parameters and Flux boundary defined by Butler-Volmer. The potential at the Amalgam domain Flux boundary was controlled based on a sweeping potential to simulate cyclic voltammetry at the probe. For each simulation the potential applied to the HOPG domain Flux boundary, subE, was maintained at a constant value. Open boundaries were set to bulk conditions. Most values collected from the literature agreed with our simulations. We note the largest discrepancies involve those surrounding the HgDW (*e.g.* k^0,

Dred, $\alpha_{Hg\text{-}Li}$). HgDW probes are sensitive to the electrolyte environment, and contaminants, especially at the Hg surface, can affect the overall probe response. However, even non-ideal probes can be quite stable throughout measurements. We used the parameters that fit best for multiple curves and considered the substrate response for interpretation.

Appendix B: Figure and Table

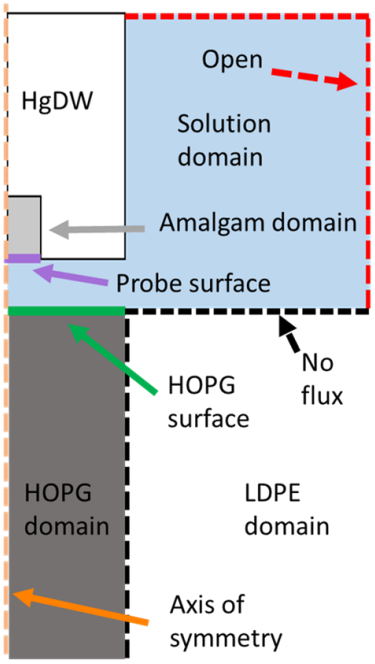

Hg domain B-V (1)

$k_f = k^0 * \exp(-\alpha_{Hg\text{-}Li} * n * f * (Eapp - E^0))$

$k_b = k^0 * \exp((1 - \alpha_{Hg\text{-}Li}) * n * f * (Eapp - E^0))$

HOPG domain B-V (2)

$k_{fLi} = k^0_{Li} * \exp(-\alpha_{HOPG\text{-}Li} * n * f * (subE - sE^0))$

$k_{bLi} = k^0_{Li} * \exp((1 - \alpha_{HOPG\text{-}Li}) * n * f * (subE - sE^0))$

Figure B1. 2D axisymmetric geometry for COMSOL simulations on HOPG edge plane. Probe and HOPG electrode surfaces are domains on the right using B-V for determining k^o.

Table B1. Parameters for COMSOL simulations.

Parameter	Variable	Simulated value	Reported values
HgDW electrode radius	R	12.5 x 10^{-6} [m]	-
HgDW depth	H	37.5 x 10^{-6} [m]	-
Length of HgDW	h2	62.5 x 10^{-6} [m]	-
HgDW:glass ratio	RG	33.75 x 10^{-6} [m]	-
HOPG electrode radius	Hedge	30 x 10^{-6} [m]	-
HOPG depth	Dedge	100 x 10^{-6} [m]	-
HOPG-HgDW distance	D	2.5 x 10^{-6} [m]	-
Cell width	Wcell	500 x 10^{-6} [m]	-
Potential sweep rate – HgDW	Nu	1 [V/s]	-
Potential sampling interval	Eint	0.001 [V]	-
Time sampling interval	Tint	Eint/nu	-
Positive potential limit	Eox	2.0 [V]	-
Negative potential limit	Ered	0.4 [V]	-
Potential applied at tip	Eapp	pw1(t)	-
Time, floating parameter	T	0 (s)	-
Bulk [M^+]	ox^0	10 [mol/m^3]	-
Electron transfer coefficient - M^+ -> M(Hg)	$\alpha_{Hg\text{-}Li}$	0.25	0.7[1]
Reduction potential - M^+ -> M(Hg)	E^0	0.96 [V]	-
Apparent rate constant - M^+ -> M(Hg)	k^0	0.0005 [cm/s]	0.01,[1] 0.008[2]
Forward rate constant – HgDW	k_f	B-V(1) *See above	-
Backward rate constant – HgDW	k_b	B-V(1) *See above	-
Diffusion coefficient – M^+ in solution	Dox	1.7 x 10^{-6} [cm^2/s]	1.7,[2] 2.4[1] for PC
Diffusion coefficient – M in Hg	Dred	5 x 10^{-6} [cm^2/s]	9.2[3]
Electron transfer coefficient – M^+ intercalation	$\alpha_{HOPG\text{-}Li}$	0.08	0.1[4]
Standard reduction potential - M^+ intercalation	sE^0	0.09 [V]	0.22,0.13, 0.086[5]
Apparent rate constant – M^+ intercalation	k^0_{Li}	1 x 10^{-4} [cm/s]	(10^{-4}),[4] (10^{-7})[5]
Forward rate constant – M^+ intercalation	k_{fLi}	B-V(2) *See above	-
Backward rate constant – M^+ deintercalation	k_{bLi}	B-V(2) *See above	-
Diffusion coefficient – M in HOPG	Dedge	3 x 10^{-10} [cm^2/s]	2 to 3.4[5]
Applied substrate potential	subE	3 to -0.5 [V]	-
Moles of electrons per mole M^+ reduction	*N*	1	-
Faraday's constant	F	96485.3 [C/mol]	-
Universal gas constant	R	8.314 [J/(mol * K)	-
Temperature	T	298.15 [K]	-
F/(R*T)	*F*	38.9 [1/V]	-

Appendix B: References

(1) Hills, G. J.; Peter, L. M., *J. Electroanal. Chem.,* **1974,** *50* (2), 175-185.

(2) Cronnolly, C.; Pillai, K. C.; Waghorne, W. E., *J. Electroanal. Chem.,* **1986,** *207* (1-2), 177-187.

(3) Kozin, L. F.; Hansen, S. C., *Mercury handbook: chemistry, applications and environmental impact*. Royal Society of Chemistry: **2013**.

(4) Ritzert, N. L.; Rodríguez-López, J. n.; Tan, C.; Abruña, H. D., *Langmuir,* **2013,** *29*(5), 1683-1694.

(5) Levi, M. D.; Aurbach, D., *J. Electroanal. Chem.,* **1997,** *421* (1-2), 79-88.

Appendix C: COMSOL Models for Chapter 5

This appendix was published as part of the supplementary materials for an original research article in the *Analyst*:

Gossage, Z.T.; Hui, J.; Sarbapalli, D.; and Rodríguez-López, J. "Coordinated Mapping of Li^+ Flux and Electron Transfer Reactivity during Solid-Electrolyte Interphase Formation at a Graphene Electrode." *Analyst*, **2020**, 145, 2631-2638. DOI: 10.1039/C9AN02637A

Description of COMSOL Simulations for Intercalation at HOPG:

We conducted simulations using the Transport of Diluted Species module within COMSOL Multiphysics 4.4, and Fick's laws for diffusion. We explored the impact of a single negative pulse and diffusional broadening at the MLG-SiO_2 edge on Li^+ flux measurements. We used a 2D geometry representing a cross section of the HgDW probe positioned near the MLG electrode (Figure C1). Three active regions were defined: 1) Amalgam, 2) MLG, and 3) Solution. All parameters used in the simulations are listed in Table C1 and referenced appropriately. At the Amalgam domain and its Flux boundary with the Solution domain, Li^+ was consumed to produce reduced species (M(Hg)) that could diffuse freely into the Amalgam domain. The simulated probe response and associated Li^+ flux was controlled via Butler-Volmer to approximate an amalgamation/stripping voltammogram. The MLG domain was controlled as another Flux boundary defined to consume Li^+ at a diffusion limited rate. Open boundaries were set to bulk conditions.

Appendix C: Figure and Table

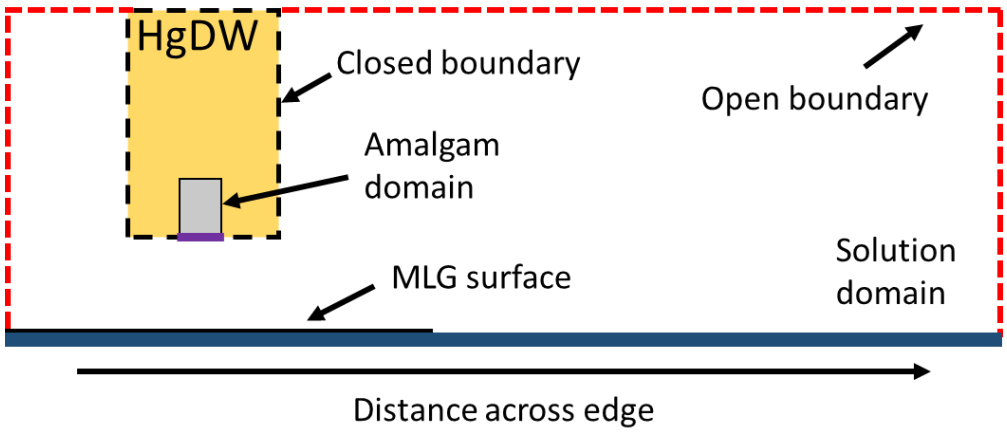

Figure C1. 2D geometry used in COMSOL model for evaluating edge and pulse effects. The probe was translated across the edge to evaluate location-dependent impact on the probe response.

Table C1. Parameters for COMSOL simulations.

Parameter	Variable	Simulated value	Reported values
MLG length	MLGL	200 x 10^{-6} [m]	-
MLG and SEI height	MLGH	100 x 10^{-9} [m]	-
Solution height	SH	500 x 10^{-6} [m]	-
Solution length	SL	500 x 10^{-6} [m]	-
Glass height	GH	2 x 10^{-6} [m]	-
Glass length	GL	500 x 10^{-6} [m]	-
HgDW electrode radius	a	12.5 x 10^{-6} [m]	-
HgDW height	PH	500 x 10^{-6} [m]	-
Ratio of glass to electrode radius	RG	3.0	-
Bulk Li^+ concentration	ox0	0.01 [mol]	-
Probe-substrate distance	d	12.5 x 10^{-6} [m]	-
Li^+ diffusion coefficient in PC	Lid	1.7 x 10^{-10} [m^2/s]	1.7,[1] 2.4[2] for PC
Li^+ diffusion coefficient in Hg amalgam	LHg	5.0 x 10^{-10} [m^2/s]	9.2[3]
HgDW scan rate	nu	1.0 [V/s]	-
Potential sampling interval	Eint	0.01 [V]	-
Time sampling interval	tinit	0.01 [s]	-
Oxidative potential limit (HgDW scan)	Eox	2.0 [V]	-
Reductive potential limit (HgDW scan)	Ered	0.6 [V]	-
Reduction potential - M^+ -> M(Hg)	E^0	0.96 [V]	-
Apparent rate constant - M^+ -> M(Hg)	k^0	0.0005 [cm/s]	0.008,[1] 0.0005[4]
Forward rate constant – HgDW	k_f	**See reference 4**	-
Backward rate constant – HgDW	k_b	**See reference 4**	-
Etch depth	etch	12.5 x 10^{-6} [m]	-
Transfer coefficient for Hg-HgLi	α	0.5	0.7[2]
Moles of electrons per mole M^+ reduction	*n*	1	-
Faraday's constant	F	96485.3 [C/mol]	-
Universal gas constant	R	8.314 [J/(mol * K)	-
Temperature	T	298.15 [K]	-
F/(R*T)	*f*	38.9 [1/V]	-

Appendix C: References

(1) C. Cronnolly, K. C. Pillai, W. E. Waghorne, *J. Electroanal. Chem*., **1986**, 207, 177-187.
(2) G. J. Hills, L. M. Peter, *J. Electroanal. Chem*., **1974**, 50, 175-185.
(3) L. F. Kozin, S. C. Hansen*, Mercury handbook: chemistry, applications and environmental impact*, Royal Society of Chemistry, **2013**.
(4) Z. T. Gossage, J. Hui, Y. Zeng, H. Flores-Zuleta, J. Rodríguez-López, *Chem. Sci*., **2019**, 10, 10749-10754.